MAPPING OF PREFRONTAL HEMODYNAMIC RESPONSES TO NOXIOUS STIMULATION AND CHRONIC PAIN RELATED RESTING-STATE FUNCTIONAL NETWORKS ASSESSED BY FNIRS

by

AMARNATH YENNU

Presented to the Faculty of the Graduate School of

The University of Texas at Arlington in Partial Fulfillment

of the Requirements

for the Degree of

DOCTOR OF PHILOSOPHY

THE UNIVERSITY OF TEXAS AT ARLINGTON

AUGUST 2016

Acknowledgements

First and foremost, I would like to thank my dissertation mentor Prof. Hanli Liu for accepting me as a part of her lab. I sincerely appreciate her valuable guidance and encouragement throughout my Ph.D. training.

I would like to thank my dissertation committee members Prof. Robert J. Gatchel for his support and guidance in chronic pain research, and Dr. Georgios Alexandrakis for his support and guidance in my dissertation. I would like to thank Dr. Cynthia Trowbridge and Ryan Hulla from the department of Kinesiology for their support in chronic pain research. I would also like to thank Dr. Fenghua Tian and all other lab members for their valuable guidance and help in my research activities. I acknowledge the support in part from the University's Interdisciplinary Research Program to sponsor the research collaboration among three Colleges (College of Engineering, College of Science, and College of Nursing and Health Innovation).

I would especially like to thank my mother (Padmavathi Yennu), my father (Shivkumar Yennu), and my brother (Mathuranath Yennu), for their faith in me and allowing me to be as ambitious as I wanted. I would also like to thank my friends, Gehna Mansinghani, Dr. Harshan Ravi, Srujan Reddy, and Chaitanya Telidevara for their love and support.

August 9, 2016

Abstract

MAPPING OF PREFRONTAL HEMODYNAMIC RESPONSES TO NOXIOUS STIMULATION AND CHRONIC PAIN RELATED RESTING-STATE FUNCTIONAL NETWORKS ASSESSED BY FNIRS

Amarnath Yennu, PhD

The University of Texas at Arlington, 2016

Supervising Professor: Hanli Liu

Neural representations of chronic pain are complex and are least understood. Numerous magnetic resonance imaging (MRI) studies have revealed structural and functional abnormalities in several cortical and sub-cortical regions in subjects with chronic low-back pain (CLBP). A more recent MRI study has reported that structural and functional brain abnormalities in pain-treated patients with CLBP are reversible, demonstrating that an appropriate treatment of chronic pain can restore normal brain functions for the patients. Due to high cost, non-portability, and other restrictions of MRI, the development of a complementary brain imaging tool is therefore crucial in order to improve the understanding of neural representations of CLBP and to assess potential brain plasticity resulting from physical or pharmacological treatment of CLBP.

Functional near-infrared spectroscopy (fNIRS) has been extensively used more than 20 years to investigate functional brain activities in subjects with and/or without neurological disorders. To date, however, fNIRS has not been utilized to study neural correlates of either chronic pain or CLBP. Therefore, the goal of my dissertation was (1)

to examine whether or not noxious and innocuous thermal pain can be objectively measured and discriminated by fNIRS taken in the frontal cortical regions of healthy subjects, and (2) to utilize fNIRS as an objective imaging modality to explore pain-induced hemodynamic activities and resting-state brain functional connectivity in all cortical regions of normal subjects and subjects with CLBP, as well as to reveal any characteristic distinctions in such hemodynamic signals between the two groups.

In my dissertation, for Aim 1, I demonstrated the feasibility of fNIRS for mapping neural correlates of selective attention and interference in the prefrontal cortex of subjects with post-traumatic stress disorder, using the linear general model. For Aim 2, I quantified, analyzed and discriminated frontal cortical hemodynamic signals in response to two levels of thermal pain, so the feasibility of using fNIRS to study neural correlates of acute thermal pain in healthy participants was reported. For Aim 3, I quantified robust temporal and spatial characteristics of hemodynamic responses in the prefrontal cortex during noxious thermal pain, induced by thermal-stimulations over three different body regions. For Aim 4, by utilizing a 133-channel fNIRS brain imager, I mapped and characterized pain-induced neural correlates in the whole cortex of normal older adults and age- and gender-matched CLBP patients, and I also observed restoration of normal brain functions in CLBP subjects after a four-week exercise treatment. For the last aim, I applied the group-level independent component analysis to the 133-channel fNIRS hemodynamic signals taken at resting state over control and CLBP subjects and successfully identified four resting-state functional networks, consistently among the pre-exercise CLBP and healthy subjects. The conclusion was that the connectivity of default mode network of subjects with CLBP is compromised due to chronic pain.

Table of Contents

List of Illustrations

List of Tables

Chapter 1

Introduction

1.1 Pain

Pain is the primary symptom for physician consultations in the United States; it can significantly interfere with a person's quality of life and general functioning (Breivik et al., 2008; R. P. Hart, Wade, & Martelli, 2003). Particularly, chronic low back pain (CLBP) is a major public health problem throughout the world. The lifetime prevalence of non-specific low back pain is reported to be as high as 84%, and the lifetime prevalence of CLBP is about 23%, with 11-12% of the population being disabled by low back pain (van Dieen, Kuijer, Burdorf, Marras, & Adams, 2012). Impairments in cognitive functioning, such as attention control, working memory, mental flexibility, problem-solving and information processing speed, are observed in patients suffering from acute and chronic pain (R. P. Hart et al., 2003). Pain can also aggravate psychological attributes, such as depression, anxiety, fear, and anger (Bruehl, Burns, Chung, & Chont, 2009). It is highly desirable to be able to objectively assess the pain, which may aid patients suffering from chronic pain, and for patients who lack communication ability (e.g., infants, patients with a speech disability, and coma). However, because of the lack of a reliable quantitative measure of pain, it is often difficult for clinicians to evaluate the degree of pain to help guide its' clinical management.

1.1.1 Transmission of nociceptive information to brain

Pain is a subjective experience, and it is highly individual and can vary with the emotional state of the individual. It is the brain's interpretation of sensory information

transmitted along pathways that starts at nociceptors (Silverthorn, Hill, & Silverthorn, 2010). Nociceptors are the specialized sensory receptors which are responsible for the detection of noxious stimuli and transforming the stimuli into electrical signals. Then, the electrical signals are conducted to the central nervous system. They are the free nerve endings of primary afferent Aδ and C fibers. Distributed throughout the body (skin, viscera, muscles, joints, meninges) they can be stimulated by mechanical, thermal or chemical stimuli. 'Fast pain' which can be described as sharp and localized pain associated with Cold or mechanical stimuli, is rapidly transmitted (12-30 m/sec) to the central nervous system by myelinated A-δ fibers. Whereas, 'slow pain' which is described as duller and more diffuse pain associated with heat, cold, or mechanical stimuli, is slowly transmitted (0.5-2 m/sec) to CNS by unmyelinated C fibers (Price, Hu, Dubner, & Gracely, 1977; Silverthorn et al., 2010). These nerve fibers synapse in the dorsal horn of spinal cord, where they are modulated (Inhibitory/excitatory) by interneurons. Then, the secondary spinal projection neurons transmit the information to the brainstem, specifically to the ventral medulla and periaqueductal gray. Information from brainstem is further relayed to the thalamus and then to cerebral regions such as somatosensory cortex, where information is interpreted as pain (for review see (Martucci, Ng , & Mackey, 2014; Willis & Westlund, 1997). In the chronic pain condition, it is suggested that inflammatory factors and sensitized receptors in the skin cause an abnormally increased transmission of nociceptive signals from preferably nerve fibers. Also, chronic pain can be attributed to either lack of inhibition or increased excitation, or both at the spinal cord, brainstem or in higher cortical layers, called 'central sensitization' (Latremoliere & Woolf, 2009; Woolf, 2011).

1.1.2 Functional neuroimaging of CNS during acute pain

Numerous functional neuroimaging studies have been performed on the human central nervous system using functional Magnetic Resonance Imaging (fMRI), position emission tomography (PET), and Single Photon Emission Computed Tomography (SPECT) to understand hemodynamic correlates of acute pain [for review (Apkarian et al., 2005)]. Such studies have shown the involvement (increased hemodynamic activity during acute pain) of various cortical and sub-cortical regions of the brain in pain processing, which are often grouped together and referred to as the 'Pain Matrix' or 'Pain Network', Commonly reported pain network regions are primary somatosensory cortex (S1), secondary somatosensory cortex (S2), anterior cingulate (ACC), insular cortex (IC), thalamus, and prefrontal cortex (PFC), Primary motor cortex (M1), and supplementary motor cortex (SMA), posterior parietal cortex (PPC), posterior cingulate cortex (PCC), basal ganglia (BG), hypothalamus (HT), amygdala (AMYG), parabrachial nuclei (PB), and periaqueductal gray (PAG) (See Fig. 1.1 for Illustration of most commonly activated regions during pain). A Meta-analysis article of neuroimaging studies on acute pain (using Contact heat, Laser Heat, Cold, Electric shock, Cutaneous pressure as noxious stimulus) processing by Apkarian and colleagues (Apkarian et al., 2005), reported that both S1 and S2 regions are most commonly activated in heat pain studies. Evidence suggests that the nociceptive input into these regions underlies the perception of sensory features of pain (Chen et al., 2002; Coghill et al., 1999; Peyron et al., 1999). Limbic system components such as ACC and IC are also activated in neuroimaging studies of heat pain, and these components have been implicated to be involved in the affective processing of pain (Fulbright et al., 2001; Rainville et al., 1997; Tolle et al., 1999). Other cortical regions such

as PFC and Parietal Association areas are also activated by heat pain and may be linked to cognitive variables such as memory or evaluation of stimulus (Coghill et al., 1999; Strigo et al., 2003). Primary Motor and Premotor cortices are less frequently activated and their role may be related to suppression of movement or actual pain evoked movements itself.

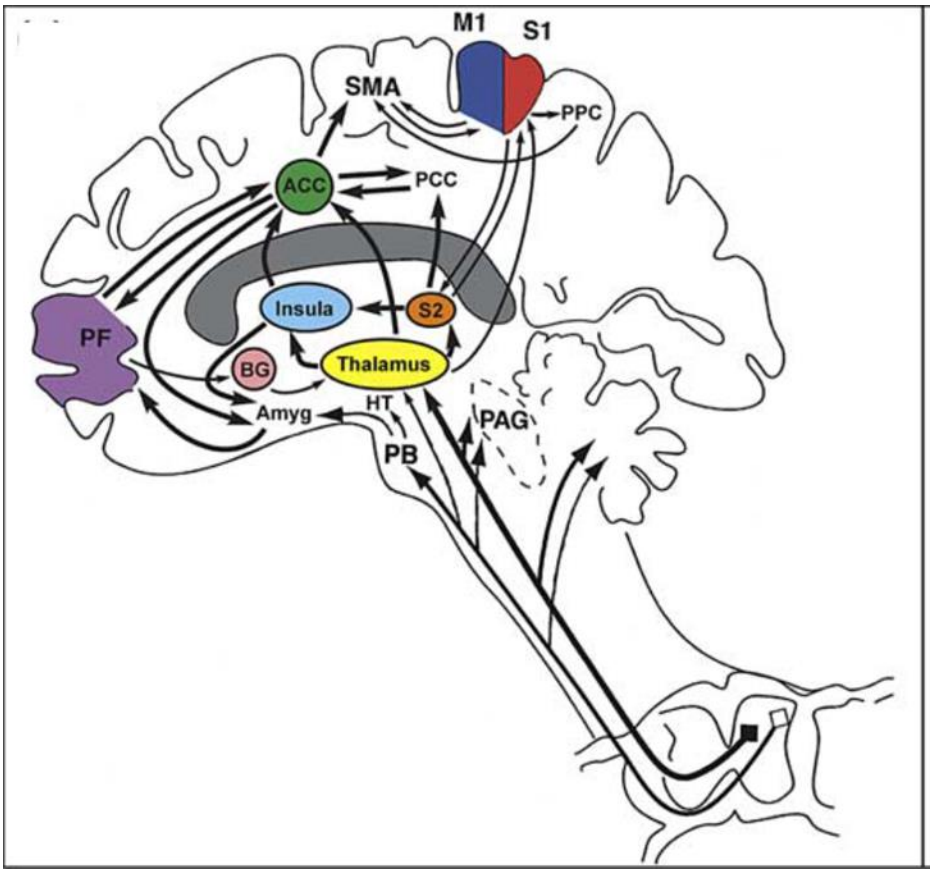

Figure 1.1 Color-coded cortical and sub-cortical regions involved in pain processing, their inter-connectivity [Figure retrieved from (Apkarian, Bushnell, Treede, & Zubieta, 2005)]. Marked regions are primary somatosensory cortex (S1, red), secondary somatosensory cortex (S2, Orange), anterior cingulate (ACC, green), insula (blue), thalamus (yellow), and prefrontal cortex (purple), Primary motor cortex (M1, dark blue), and supplementary motor cortex (SMA), posterior parietal cortex (PPC), posterior cingulate cortex (PCC),

basal ganglia (BG, pink), hypothalamus (HT), amygdala (AMYG), parabrachial nuclei (PB), and periaqueductal gray (PAG).

1.1.3 Structural and functional changes in brain associated with CLBP

Chronic pain is a complex process, and underlying neural mechanisms of chronic pain have been poorly understood. To understand brain's neural mechanisms in the presence of chronic low back pain in humans, numerous structural and functional neuroimaging studies have been performed on central nervous system using imaging modalities such as MRI and PET (Wand et al., 2011). Multiple structural MRI studies have revealed decreased Grey Matter in Dorsolateral Prefrontal Cortex (Apkarian, Sosa, Sonty, et al., 2004; Ivo et al., 2013; Schmidt-Wilcke et al., 2006; Seminowicz et al., 2011), Temporal Lobes (Baliki, Schnitzer, Bauer, & Apkarian, 2011; Luchtmann et al., 2014; Schmidt-Wilcke et al., 2006; Seminowicz et al., 2011), Primary Somatosensory Cortex (Schmidt-Wilcke et al., 2006; Seminowicz et al., 2011), Insula (Baliki et al., 2011; Seminowicz et al., 2011), and several other cortical and sub-cortical regions of CLBP patients.

Functional neuroimaging studies using fMRI, and PET reported abnormal cerebral hemodynamic activities in CLBP patients (Baliki et al., 2006; Baliki, Geha, Apkarian, & Chialvo, 2008; Derbyshire et al., 2002; Tagliazucchi, Balenzuela, Fraiman, & Chialvo, 2010). Also, several other neuroimaging studies have reported increased cortical responses to noxious subcutaneous stimulation of back (Flor, Knost, & Birbaumer, 1997), acute experimental muscle pain (Diers et al., 2007), and peripheral noxious input (Giesecke et al., 2006; Giesecke et al., 2004; Kobayashi et al., 2009) in the CLBP

patients. Notably, a recent MRI-based study demonstrated that functional and structural brain abnormalities (specifically the left DLPFC) are reversible and thus treating chronic pain can restore normal brain (Seminowicz et al., 2011). Therefore, the development of complementary assessment tools for monitoring CLBP is crucial to improving the understanding of neural representations of CLBP and to assess potential brain plasticity resulting from physical or pharmacological treatment in CLBP condition.

1.1.4 Abnormal Resting-state functional connectivity (RSFC) in CLBP

The temporal synchronization of spontaneous, low-frequency neuronal activity in anatomically separated regions in the brain is referred to as resting-state functional connectivity. A Recent method of resting-state fMRI has focused on multiple regions in the brain, targeting inherent and altered measures of connectivity between regions and within brain 'networks' (Fox et al., 2005). RSFC method has the advantage of providing information about the natural state of brain activity in chronic pain without having to apply any external sensory or cognitive stimulation. Chronic pain has been noted to alter several networks, of individual brain regions with similar low-frequency oscillatory activity and an increase or decrease in the presence or absence of external stimulation (Smith et al., 2009).These networks are primarily the default-mode networks (DMN) (Greicius, Krasnow, Reiss, & Menon, 2003), its constituents are more active at rest; the salience and executive control networks, its constituents are more active during stimulation of the senses or tasks; and sensory-motor networks, its constituents are related to sensory and motor processing. Recent functional MRI studies using resting-state functional connectivity analysis, have reported disrupted Default Mode Network (DMN) connectivity in CLBP patients (Baliki et al., 2008; Kornelsen et al., 2013; Loggia et al., 2013;

Tagliazucchi et al., 2010). Using fMRI, Baliki and colleagues reported reduced DMN connectivity in CLBP patients, specifically in the medial prefrontal cortex, posterior cingulate cortex and amygdala (Baliki et al., 2008). In another resting-state fMRI study, Tagliazucchi and colleagues reported that abnormal connectivity in DMN structures such as angular gyrus, bilateral insular cortex, and orbital part of the middle frontal gyrus (Tagliazucchi et al., 2010).

1.2 Principles of Functional Near Infrared Spectroscopy

Functional Near-infrared spectroscopy (fNIRS) is a non-invasive imaging technique which has been widely used in the field of neuroscience to study neural activity in the human brain. It employs safe levels (1-2eV photon energy) of optical radiation (Near-infrared radiation) within 650-950 nm wavelength range (referred as 'optical window' or 'Physiological Window') [see Fig. 1.2], where the relatively low attenuation of near infrared light accounts for light penetration through several centimeters of biological tissue of interest. Due to low NIR light attenuation, it is possible to non-invasively probe the human cerebral cortex and obtain cerebral concentration of hemoglobin which is dominant NIR light absorbing chromophore in the brain. Figure 1.3 shows the banana-shaped path followed by NIR light from the source to the photo-detector while passing through Skin, Galea Aponeurotica, Skull, Dura and Arachnoid matter, and superficial layers of cerebral cortex. Due to the differential NIR absorption spectra of oxy-hemoglobin (HbO_2) and deoxy-hemoglobin (HbR), we can obtain separate measurements of [HbO_2] and [HbR] concentrations in the brain. To separately measure [HbO_2] and [HbR] concentrations simultaneously, NIRS measurements at two wavelengths are sufficient. These two types of hemoglobin concentrations measured are

the result of the interplay between regional blood flow, blood volume, and metabolic rate of oxygen consumption. The sum of [HbO_2] and [HbR] concentrations gives an estimate of cerebral blood volume.

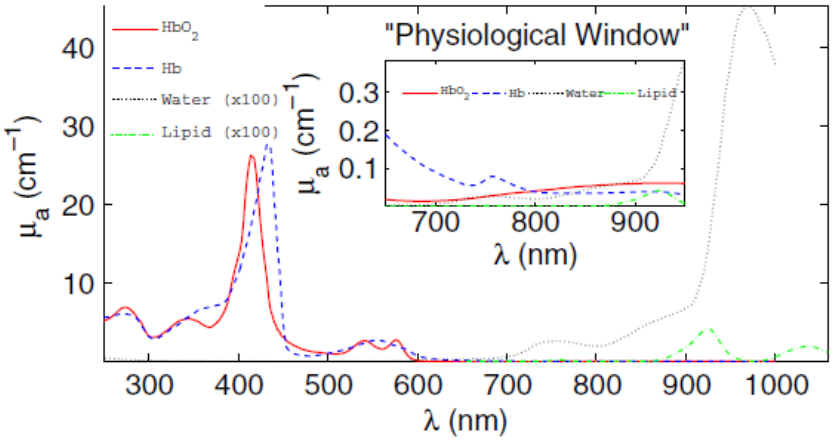

Figure 1.2 Absorption spectra of major tissue chromophores (Oxy-Hemoglobin, Deoxy-Hemoglobin, Water, and Lipid) over the wide wavelength range. Within physiological window, wavelength-dependent absorption coefficients (μ_a) of water and lipid are relative very low as compared to that of Oxy-Hemoglobin and Deoxy-Hemoglobin. Therefore, light can penetrate several centimeters into the tissue [Figure retrieved from.(Durduran et al., 2010)].

1.2.1 Continuous-wave (CW) fNIRS systems

There are three types of NIR imaging systems based on the type of light source, namely, Continuous-wave (CW), Time-resolved (TRS), and Frequency domain (FD) NIRS systems (Durduran et al., 2010). CW NIR systems are simplest, portable, inexpensive, and most commercially available systems Which use CW light as their source. In this study, I used two CW-fNIRS systems, namely, Cephalogics brain imager, and Shimadzu brain imager [Fig. 1.4]. CW-fNIRS instruments measure regional changes

in hemoglobin concentration, and oxygenation, based on the light attenuation measurements through the cortical tissue. Using these attenuation measurements, it is very difficult to obtain absolute concentrations of hemoglobin since the real path length of the light within the tissue is unknown and cannot be measured with CW-fNIRS systems. FD and TRS NIRS systems can be used to obtain information about real path length of photons along with attenuation measurements (Chance et al., 1988; Delpy et al., 1988; Patterson, Chance, & Wilson, 1989), such that the absolute concentrations of hemoglobin can be calculated. CW-fNIRS systems rely on the simplified assumptions about the tissue being probed and the changes in the sampled volume. Therefore, only relative hemoglobin concentration changes from baseline can be measured.

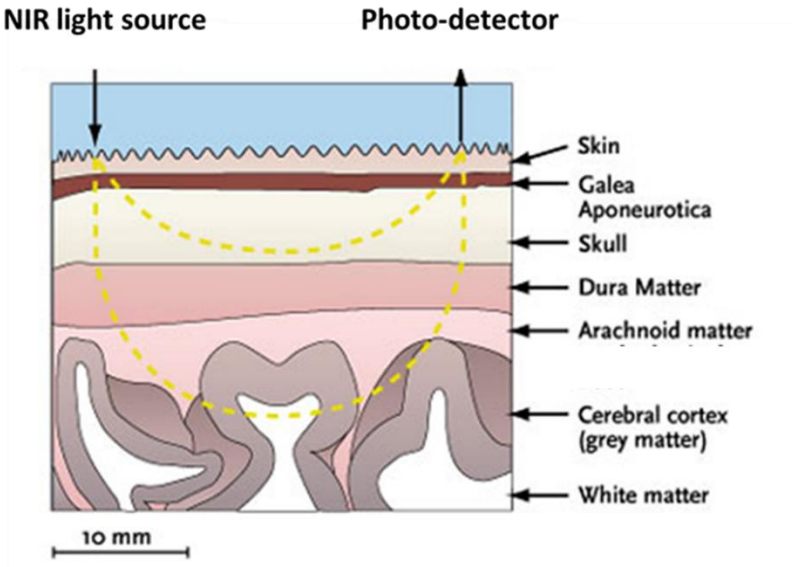

Figure 1.3 Light from the NIR light source is guided to the head by an optode. A photo-detector will collect the light which leaves the head at certain distance (typically source and detector are placed 3 centimeters apart). The photons follow a banana-shaped path from light source to the detector while passing through Skin, Galea Aponeurotica, Skull, Dura and Arachnoid matter, and superficial layers of cerebral cortex.

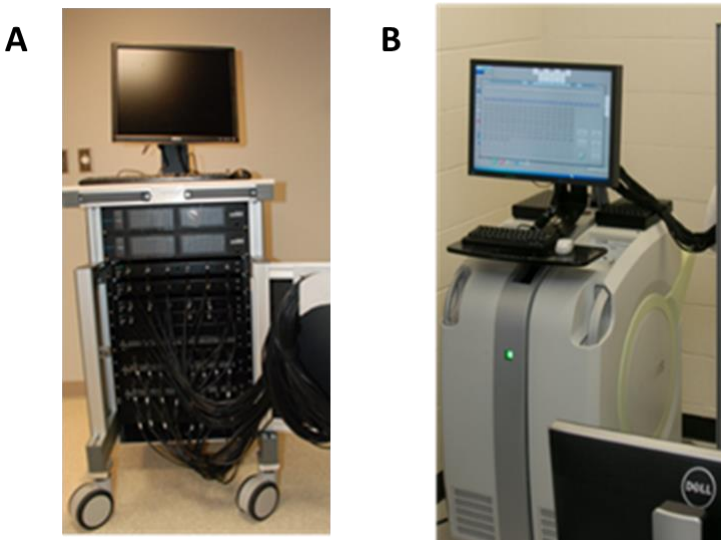

Figure 1.4 Continuous-wave fNIRS systems used in this study. (A) Cephalogics brain imager. (B) Shimadzu brain imager.

1.2.2 Modified Beer-Lambert Law

Modified Beer-Lambert law (MBLL) is based on classic Beer-Lambert law. It is a widely used model for calculating hemodynamic responses in the cerebral cortex of humans. Beer-Lambert law describes linear relationship between absorbance [also referred as Optical Density (OD)], *OD*, of light through a medium and wavelength dependent extinction coefficient (Molar absorptivity of a chromophore), $\varepsilon(\lambda)$. Beer-Lambert law is shown in equation (1.1) below.

$OD = Log\left(\frac{I}{I_0}\right) = \varepsilon(\lambda).c.L$ equation (1.1)

In equation (1.1), *I* is the intensity of detected light after transmission through the medium, I_0 is the intensity of incident light, *c* is the concentration of the chromophores, and *L* is the length of the path traveled by the light in the medium. Beer-Lambert law has been successfully applied to CW-fNIRS imaging under simplified assumptions, and it is referred as MBLL (Cope & Delpy, 1988; Reynolds et al., 1988). Assumptions are (1)

Medium is assumed to highly, but constant scattering, (2) Medium is homogeneous, and (3) Medium has a homogeneous change of properties of interest within each sampled volume (Obrig & Villringer, 2003). For scattering medium, equation (1.1) can be rewritten as equation (1.2) below.

$$OD(\lambda) = \varepsilon(\lambda).c.d.DPF(\lambda) + G(\lambda) \quad (1.2)$$

$$Where\ DPF(\lambda) = \langle L \rangle / d \quad (1.3)$$

In equation (1.2), *G(λ)* is wavelength dependent contribution of the attenuated light corresponding to scattering, *d* is the distance between source and detector, *DPF(λ)* is the wavelength dependent differential path length factor, and $\langle L \rangle$ is the mean path length travelled by the detected photons. The DPF accounts for the increase in path length due to tissue scattering. The DPF values of various tissue samples have been studied experimentally (Duncan et al., 1995; Kohl et al., 1998), and can be looked up in a table (Essenpreis et al., 1993). Based on the assumption that the tissue is highly, but constant scattering, DPF(λ) and G(λ) can be assumed to be constant. This assumption allows us for assessment of changes in chromophore concentration by subtracting out G(λ) term in equation (1.2) This is considered reasonable while measuring hemodynamic activity changes since it affects the absorption coefficient more significantly that the scattering coefficient (Obrig & Villringer, 2003). Then, equation (1.2) can be rewritten as equation (1.4) below.

$$\Delta OD(\lambda) = OD_t(\lambda) - OD_{t0}(\lambda) = \varepsilon(\lambda).\Delta c.d.DPF(\lambda) \quad (1,4)$$

In equation (1.4), OD_{t0} is the initial absorbance, and OD_t is the absorbance at time *t* after the change in concentration of chromophores. Each of the chromophores have distinct absorption spectrum in the near-infrared range of wavelengths, therefore, the

simultaneous measurements of several chromophores concentration changes by taking fNIRS measurements at multiple wavelengths is possible. The absorption spectra of main chromophores in optical window are shown in figure (1.2). In fNIRS, HbO_2 and HbR are mainly of interest since they are related to regional cerebral blood flow (rCBF) and other chromophores' changes are orders of magnitude smaller than that of HbO_2 and HbR. Using two wavelengths of light, we can derive two simultaneous equations to be solved for each of two hemoglobin ($\Delta[HbO_2]$ and $\Delta[HbR]$) chromophores changes. Equation (1.4) can be rewritten as equation (1.5) and (1.6) for two distinct wavelengths of light after separating the contributions from HbO_2 and HbR.

$$\Delta OD(\lambda_1) = (\varepsilon_{HbO}(\lambda_1)\Delta[HbO_2] + \varepsilon_{HbR}(\lambda_1)\Delta[HbR]).d.DPF(\lambda_1) \quad (1.5)$$

$$\Delta OD(\lambda_2) = (\varepsilon_{HbO}(\lambda_2)\Delta[HbO_2] + \varepsilon_{HbR}(\lambda_2)\Delta[HbR]).d.DPF(\lambda_2) \quad (1.6)$$

where $\Delta[HbO_2]$ is the change in HbO_2 concentration and $\Delta[HbR]$ is the change in HbR concentration. Assuming that $\varepsilon(\lambda)$ for each chromophore and can be looked up from the extinction spectra and DPF values of the tissue is known, concentration changes of HbO_2 and HbR can be obtained by solving the two simultaneous equations at two distinct wavelengths, i.e., equations (1.5) and (1.6).

1.3 Specific Aims

In the past two decades, fNIRS has been extensively used in the field of neuroscience for studying functional brain activities in health and disease. Researchers have utilized fNIRS to study neural correlates of seizures (Adelson et al., 1999; Sokol, Markand, Daly, Luerssen, & Malkoff, 2000; Watanabe et al., 2000), Alzheimer disease (Fallgatter et al., 1997; Hock et al., 1996), depression (Eschweiler et al., 2000; Matsuo,

Kato, Fukuda, & Kato, 2000), schizophrenia (Fallgatter & Strik, 2000; Okada, Tokumitsu, Hoshi, & Tamura, 1994), and post-traumatic stress disorder (Tian et al., 2014; Yennu et al., 2016). Also, functional NIRS-based pain studies have been reported to investigate somatosensory cortex hemodynamic responses to thermally-induced pain (Becerra et al., 2009), prefrontal hemodynamic responses to mechanically-induced low back pain (Holper et al., 2014) and somatosensory hemodynamic responses to noxious electrical stimulation of the thumb (Yucel et al., 2015). However, to date, none of the fNIRS-based studies have investigated neural correlates of either chronic pain or CLBP in the whole cortex. Functional NIRS-based brain imaging modality may have the ability to facilitate a better understanding of pain processing at the cortical regions induced by acute pain and in chronic pain condition. Understanding of temporal and spatial characteristics of such hemodynamic responses might have potential applications in a clinical setting where pain needs to be assessed objectively. The main objective of this study was to demonstrate that fNIRS can reveal cortical activities and abnormalities in patients with CLBP during pain-inducing leg raising tasks, and it can further reveal abnormal resting-state functional networks in whole cortex of CLBP, such that it could become a portable and complementary neuroimaging tool to monitor and guide treatments for patients with CLBP. Specifically, my research aims were,

1. To establish the methodology to map prefrontal hemodynamic responses measured by fNIRS, and to demonstrate the feasibility of fNIRS to be able to reveal neural correlates of selective attention in the prefrontal cortex of PTSD patients [Chapter 2; (Yennu et al., 2016)].

2. To examine whether or not noxious and innocuous thermal pain can be objectively measured and discriminated by fNIRS measurements taken in the frontal cortical regions of healthy subjects [Chapter 3, (Yennu et al., 2013)].
3. To test the robustness and consistency of temporal and spatial characteristics of hemodynamic responses in the prefrontal cortex during noxious thermal pain, induced by thermal-stimulations over three different body regions: right forearm; right temporomandibular joint, and left forearm [Chapter 4].
4. To demonstrate feasibility of fNIRS for studying and mapping whole-cortex neural correlates of pain induced by leg-raising-tasks in CLBP patients and monitoring of treatment effects [Chapter 5]
5. To demonstrate feasibility of fNIRS for studying and mapping Independent-Component-Analysis-derived resting state functional networks in whole-cortex of CLBP patients [Chapter 6].

Chapter 2

Prefrontal Responses To Stroop Tasks In Subjects With Post-Traumatic Stress Disorder Assessed By Functional Near Infrared Spectroscopy

2.1 Abstract

Studies on post-traumatic stress disorder (PTSD) showing attentional deficits have implicated abnormal activities in the frontal lobe. In this study, I utilized multichannel functional near-infrared spectroscopy (fNIRS) to investigate selective attention-related hemodynamic activity in the prefrontal cortex among 15 combat-exposed war-zone veterans with PTSD and 13 age- and gender-matched healthy controls. While performing the incongruent Stroop task, healthy controls showed significant activations in the left lateral prefrontal cortex (LPFC) compared to baseline readings. This observation is consistent with previously reported results. In comparison, subjects with PTSD failed to activate left LPFC during the same Stroop task. Observations in this study may implicate that subjects with PTSD experienced difficulty in overcoming Stroop interference. I also observed significant negative correlation between task reaction times and hemodynamic responses from left LPFC during the incongruent Stroop task in the PTSD group. Regarding the methodology used in this study, I have learned that an appropriate design of Stroop paradigms is important for meeting an optimal cognitive load which can lead to better brain image contrasts in response to Stroop interference between healthy versus PTSD subjects. Overall, the feasibility of fNIRS for studying and mapping neural correlates of selective attention and interference in subjects with PTSD is reported.

2.2 Introduction

According to American Psychiatric Association, post-traumatic stress disorder (PTSD) is an anxiety disorder that can be developed after exposure to traumatic events, such as combat environment, sexual assault, or the serious injury, resulting in psychological trauma. Patients with PTSD often re-experience the traumatic event in the form of nightmares, intrusive recollections, flashbacks, and physiological arousal and distress in response to reminders of trauma. Hyperarousal symptoms, such as hypervigilance, exaggerated startle, and difficulty sleeping or concentrating are also reported among PTSD patients. The estimated lifetime prevalence of PTSD among American adults is 7.8% (Kessler, Sonnega, Bromet, Hughes, & Nelson, 1995). Combat-related PTSD is found in 9–25% of war-zone veterans and is often persistent and comorbid with other psychiatric disorders, even after the veterans return to their civilian lives (Arbanas, 2010; Dohrenwend et al., 2006; Erickson, Wolfe, King, King, & Sharkansky, 2001; Hoge et al., 2004; Kessler et al., 1995).

Numerous neuropsychological studies have reported the presence of cognitive dysfunction associated with PTSD, including memory impairments, attention deficits and learning disabilities (Brandes et al., 2002; Bremner et al., 1993; Koenen et al., 2001; Roca, Hart, Kimbrell, & Freeman, 2006; Vasterling, Brailey, Constans, & Sutker, 1998; Vasterling et al., 2002). In recent years, neuroimaging studies using positron emission tomography (PET) or functional magnetic resonance imaging (fMRI) on PTSD patients have primarily focused on symptom provocation or responses to trauma-related or emotional stimuli. The reviews and meta-analysis of the PTSD related neuroimaging studies suggest that hyperactivation within limbic regions (mainly amygdala and insula)

may account for exaggerated fear responses and the persistence of traumatic memories (Etkin & Wager, 2007; Francati, Vermetten, & Bremner, 2007; Liberzon & Sripada, 2008; Shin & Liberzon, 2010). In addition, it is suggested that hypoactivation of prefrontal regions (mainly anterior cingulate cortex and ventromedial prefrontal cortex) associated with hyperactivation of amygdala may indicate inability of prefrontal regions to inhibit amygdala activity. A recent review article on neuropsychological and neuroimaging studies of PTSD patients highlights the importance of further understanding the PTSD related attentional and inhibitory dysfunctions in order to successfully treat PTSD patients (Aupperle, Melrose, Stein, & Paulus, 2012).

In the past decade, functional near infrared spectroscopy (fNIRS), a noninvasive optical imaging method, has been extensively used in the field of neuroimaging for studying functional brain activities. This technique measures the cerebral hemodynamics and oxygenation using near infrared light (670 to 900 nm) which can penetrate through the scalp and skull to reach superficial layers of cerebral cortex, while being partially absorbed by the oxygenated hemoglobin (HbO_2) and deoxygenated hemoglobin (Hb) in the cerebral blood (Boas, Dale, & Franceschini, 2004). In a recent report, a multi-channel fNIRS was utilized to measure prefrontal cortex hemodynamic activations from 16 veterans with PTSD and age-/gender- matched healthy controls during non- trauma-related memory tasks (Tian et al., 2014). In particular, the PTSD participants, but not the controls, appeared to suppress prefrontal activity during memory retrieval. This deactivation was more pronounced in the right dorsolateral prefrontal cortex during the retrieval phase. These deactivations in PTSD patients might implicate an active inhibition of dorsolateral prefrontal neural activity during retrieval of working memory. Overall, that

study demonstrates that fNIRS could be a portable and complementary neuroimaging tool to study the cognitive dysfunctions associated with PTSD.

In this study, I focused on an objective and quantitative understanding of the selective attention and inhibitory function of cognition in subjects with PTSD, specifically using the color-word matching Stroop task. The Stroop test (MacLeod, 1991; Stroop, 1935) was introduced by J. R. Stroop (Stroop, 1935) and has been a classic protocol utilized to measure selective attention, cognitive flexibility and processing speed, as well as executive functions. While the color-word Stroop test includes neutral, congruent, and incongruent trials conventionally, researchers often focus on brain activations or performance outcomes during incongruent Stroop trials with respect to either neutral or congruent trials. During an incongruent Stroop test, a word is displayed in an ink color different from what the name of the word means (e.g., word “BLUE” is printed in red ink). Naming the ink color of the word requires more mental effort than just reading the word. The cognitive mechanism of Stroop test is associated with selective attention; the subject has to manage his or her attention by inhibiting or interfering one response in order to promote another. This phenomenon is called ‘Stroop interference’. Numerous functional neuroimaging studies investigating neural correlates of the Stroop interference using PET and fMRI consistently reported activation in lateral prefrontal cortex (LPFC) regions, reflecting the Stroop interference along with activation of the anterior cingulate cortex (Derrfuss, Brass, Neumann, & von Cramon, 2005; Laird et al., 2005). Recent fNIRS studies on the Stroop interference also reported activation in LPFC regions, implicating that LPFC plays a critical role in coping up with the Stroop interference (Ehlis, Herrmann, Wagener, & Fallgatter, 2005; Schroeter, Zysset, Kruggel, & von Cramon, 2003;

Schroeter, Zysset, Kupka, Kruggel, & Yves von Cramon, 2002; Schroeter, Zysset, & von Cramon, 2004; Yanagisawa et al., 2010). Using fNIRS, moreover, Matsuo and colleagues revealed reduced prefrontal activity in a PTSD group when compared to a non-PTSD group during a verbal fluency task (Matsuo et al., 2003).

In this study, fNIRS was used to acquire prefrontal hemodynamic signals from a group of veterans with PTSD and age- and gender-matched healthy controls, in order to investigate both temporal and spatial patterns of pre-frontal responses during performance of a Stroop paradigm. The goal of the study was to further illustrate that fNIRS is able to reveal prefrontal activities and deficits in subjects with PTSD during selective attention processes, and that fNIRS could become a portable and complementary neuroimaging tool to monitor and guide treatments for patients with PTSD.

2.3 Materials and Methods

2.3.1 Participants

A Total of 15 combat exposed veterans diagnosed with PTSD (all males, right-handed, mean ± SD age = 29.1 ± 9.0 years) were recruited in this study. The comorbid conditions diagnosed in these 15 veterans are provided in Table 2.1. The comorbid conditions diagnosed are attention deficit hyperactivity disorder (ADHD) (n = 4), major depressive disorder (n = 5), alcohol dependence (n = 4), musculoskeletal pain (n = 4), insomnia (n = 3), history of blast exposure (n = 1), anxiety disorder (n = 2), mild traumatic brain injury (mTBI) (n = 3), and learning disorder (n = 2). The hemodynamic activations in veterans with PTSD were compared against 13 age- and gender- matched healthy

controls (all males, right- handed, mean ± SD age = 33.3 ± 10.3 years). The protocol used in the study was reviewed and approved by the Institutional Review Board (IRB) of the University of Texas at Arlington (UTA). The methods were carried out in accordance with approved guidelines by IRB of UTA. Written informed consent was obtained from all participants prior to the fNIRS scan.

Table 2.1. Comorbid conditions of veteran participants with PTSD.

Participant number	**Comorbidities**
1	PTSD and Anxiety Disorder (Not otherwise specified)
2	PTSD, ADHD and Substance Abuse Disorder
3	PTSD, ADHD and Musculo-skeletal pain
4	PTSD, Anxiety Disorder (Not Otherwise specified), Musculo-skeletal pain and insomnia
5	PTSD, Musculo-skeletal pain and Insomnia
6	PTSD, Alcohol Dependence, History of blast exposure and learning disorder
7	PTSD, Major depressive episodes and Alcohol Abuse
8	PTSD, Major depressive episodes, Insomnia and Musculo-skeletal pain
9	PTSD and Moderate Traumatic brain injury
10	PTSD, Major depressive episodes, Moderate TBI and History of learning disorder
11	PTSD, Major depressive episodes, ADHD and Insomnia
12	PTSD, Depression symptoms, Attentionality symptoms,
13	PTSD, Moderate TBI, Major depressive episodes, Alcohol abuse
14	PTSD, ADHD and Alcohol abuse
15	PTSD

2.3.2 Tasks and paradigm

The paradigm used in this study consisted of two sessions. The first session, named Stroop1, was a similar version of neutral trails of the Stroop color-word task. It consisted of word-name matching tasks and was a simple paradigm where participants had to match the name of the word displayed at the center of a computer screen to either

one of the options displayed at the bottom of the screen, by using arrow buttons on the keyboard (See Fig. 2.1A). In this task, all of the words were written in black ink color. The second session was called Stroop2 and made of incongruent trails of the Stroop color-word task. During this session, participants had to match the ink color of the displayed word, whose color was different from the name of the word itself, to the name of the word given in options (See Fig. 2.1B).

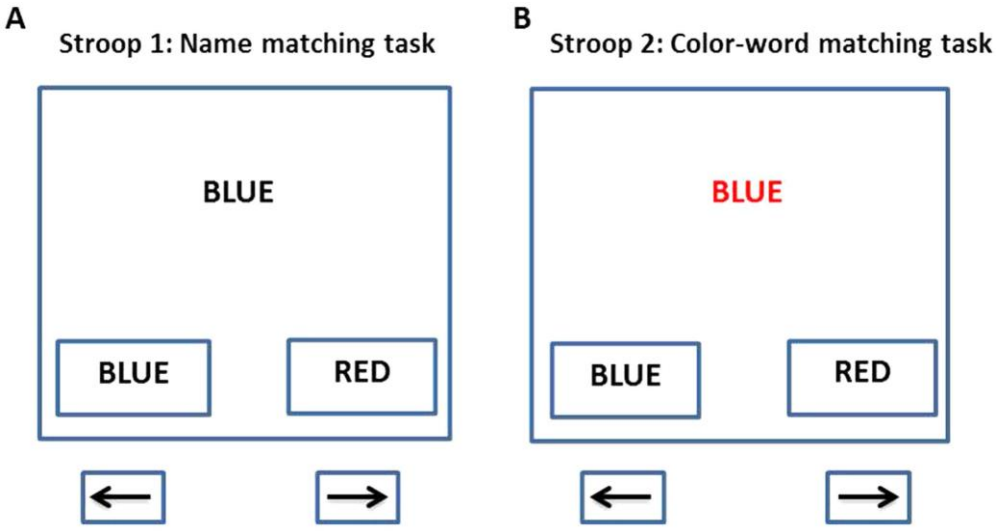

Figure 2.1. Examples of Stroop trials used in this study. (A) Stroop1 (i.e., neutral Stroop task) trial: Participants should match the word name given at the center of the screen to word name given in options at bottom of the screen, by pressing the appropriate left or right arrow key. (B) Stroop2 (i.e., incongruent Stroop task) trial: Participants should match the ink color of the word given at the center of the screen to word name given in options at the bottom of the screen, by pressing the appropriate left or right arrow key.

All the participants were asked to sit comfortably before a computer, and complete a session of Stroop1 task, followed by a session of Stroop2 task, while their brains were scanned by multichannel fNIRS. Within each Stroop1 and Stroop2 session, the paradigm

consisted of a baseline (resting) period of 30 sec, followed by eight blocks of stimulation-and-resting sequences. Within each block, five random Stroop trials (generated by computer) were given to the subjects. The subjects were instructed to select the appropriate option accurately without any time constraint. Between two blocks, there was an inter-stimulus or resting interval of 15 sec. Before each fNIRS measurement session started, all participants were trained to practice a few trials of Stroop1 and Stroop2 tasks. An experimenter observed the course of practice to confirm that the participants understood the paradigm correctly. The accuracy of each participant's performance in each of the Stroop task was measured by the percentage of correctly performed trials divided by the total number of trials (= 5 trials × 8 blocks) in each session. The reaction time measured for each participant was defined as time taken to complete a single block of five Stroop trials.

2.3.3 Functional near infrared spectroscopy

2.3.3.1 Instrument.

A multi-channel, continuous wave, fNIRS imaging system (Cephalogics LLC., Boston, MA) was used to acquire each participant's prefrontal hemodynamic activities during performance of the tasks (Zeff, White, Dehghani, Schlaggar, & Culver, 2007). The system consisted of near infrared light sources (light emitting diodes, LEDs) emitting at two wavelengths (750 nm and 850 nm) of light and avalanche photodiodes (APDs) as detectors. This system provided fNIRS signals with a sampling rate of 10.8 Hz. For this specific experiment, the fNIRS probe array composed of 12 pairs of light sources and 16 detectors, was placed symmetrically over both hemispheres of the participant's forehead (see Fig. 2.2). The bottom row of 6 pairs of light sources in the probe was placed just

above the participant's eyebrows, and its midpoint was ~3.5 cm above the nasion. This probe provided a total of 36 measurements (channels) when only the nearest source-detector pairs were considered (the nearest source-detector separation was 2.8 cm). Other measurements from larger source-detector separations were excluded because their signals were too weak to be scientifically meaningful. The probe assembly was constructed with low-weight optical fibers (TechEn Inc., Boston, MA) and thin polyethylene film to ensure participants' comfort during the experiment.

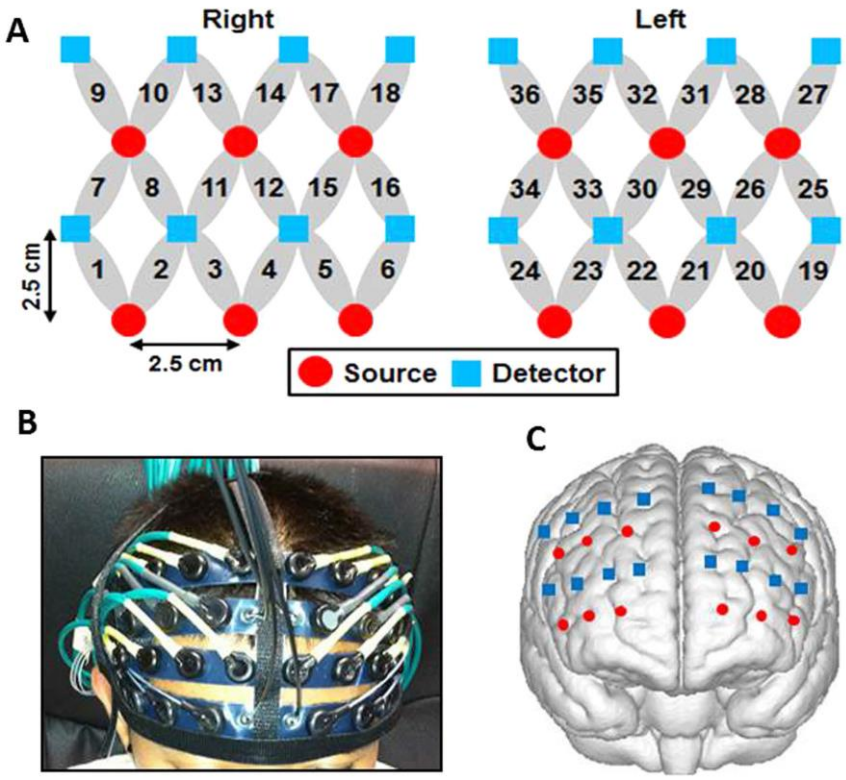

Figure 2.2. Configuration and cortical position of the multi-channel fNIRS probe array. (A) Configuration of the fNIRS probe. Red circles represent light sources, blue squares represent detectors, and gray ellipses represent the nearest source-detector pairs (as channels) to measure the brain activities. (B) Placement of the fNIRS probe on a participant's forehead. (C) Co-registration of the sources and detectors on a standard

brain atlas template. The probe partially covers the frontopolar, dorsolateral, and ventrolateral prefrontal regions on both hemispheres. The anatomical position of each channel on the brain atlas is detailed in Table 2.2.

2.3.3.2 Spatial registration

To estimate the cortical regions covered by the fNIRS probe, a spatial registration procedure was performed among six randomly selected participants (Singh, Okamoto, Dan, Jurcak, & Dan, 2005).

Once the fNIRS probe was placed on the subject's forehead (see Fig. 2.2B), the positions of light sources and detectors along with five cranial landmarks (the nasion, inion, left and right pre-auricular points, and vertex) were measured using a PATRIOT motion tracking system (Polhemus, Colchester, Vermont, USA.). The cranial landmarks served as mediators to convert the real -world stereotaxic coordinates of the optodes to the Montreal Neurological Institute (MNI) coordinates used in a standard brain MRI atlas based on the affine transformation (Tian et al., 2012). Figure 2.2C shows the registered optode positions (aver-aged over six participants) on the standard human brain atlas. The probe partially covered the frontopolar area (BA 10), dorsolateral prefrontal cortex (DLPFC; BAs 9 and 46), pars triangularis (BA 45) and pars opercularis (BA 44). A detailed report is given in Table 2.2. Because the fNIRS probe was carefully placed on each individual participant's forehead by referring to the nasion and eyebrows, the registered optode positions across individual participants were relatively consistent (positional variations were about 5 mm) in comparison with the separation of two neighboring measurement channels.

Table 2.2. Registration of the fNIRS channel positions on a standard brain atlas. The channel numbers are defined in Fig. 2.2A.

Hemisphere	**Brodmann Area (BA)**	**Channel #**
Right	BA9	13, 14, 15, 16, 17, 18
	BA10	4, 5, 6
	BA44	9, 10
	BA45	1, 7, 8
	BA46	2, 3, 11, 12
Left	BA9	28, 31, 32, 33, 34, 35, 36
	BA10	22, 23, 24
	BA44	27
	BA45	19, 25, 26
	BA46	20, 21, 29, 30

2.3.3.3 Data screening and processing

The temporal evolutions of light intensities measured during both Stroop1 and Stroop2 sessions were screened and processed using a publically available toolbox (Homer, http://www.nmr.mgh. harvard.edu /PMI/resources/ homer/home.htm) (Huppert, Diamond, Franceschini, & Boas, 2009). First, the raw light intensity signals were visually inspected to exclude blocks associated with significant motion artifacts (with an intensity fluctuation of 15% or larger from the baseline) during each session. Then the resulted signals free from motion artifacts were low-pass filtered at a cut- off frequency of 0.2 Hz to remove electronic noise and systemic noise (cardiac and respiratory oscillations) and high-pass filtered at a cut-off frequency of 0.01 Hz to remove any possible slow baseline drift. Then, changes of oxygenated and deoxygenated hemoglobin concentrations (i.e., HbO_2 and Hb, respectively) relative to the baseline were quantified following the modified Beer- Lambert Law (Cope et al., 1988). At this step, we estimated the differential

pathlength factor (DPF) to be 6.2 at 750 nm and 5.8 at 850 nm, based on published data for adult heads (Essenpreis et al., 1993).

2.3.3.4 Linear regression for reaction times and HbO_2 changes

For both Stroop tasks, correlations between the participants' reaction times and corresponding HbO_2 changes (i.e., β-values) were tested using linear regression at each measurement channel for both control and PTSD groups, separately. In addition, correlations between participants' reaction times and ROI-averaged HbO_2 responses (i.e., Mean β-values over the ROI) were calculated for both the control and PTSD groups, separately.

2.3.3.5 General linear model (GLM) analysis

To quantify cerebral hemodynamic activities during Stroop1 and Stroop2 tasks, a model-based statistical analysis tool, general linear model (GLM), was utilized. GLM analysis has been increasingly utilized to analyze fNIRS data over the last decade to identify cortical areas which are significantly stimulated during a given task (Hassanpour et al., 2014; Plichta et al., 2006; Tian & Liu, 2014; Ye, Tak, Jang, Jung, & Jang, 2009). In GLM, a hemodynamic response function (HRF) is used to serve as a model to predict the change in HbO_2 signals due to task stimulation; GLM can be expressed by equation (2.1):

$$z(t) = \beta\, f(t) + \varepsilon, \qquad (2.1)$$

where $f(t) = h(t) \otimes s(t)$. (2.2)

In equation (2.1), *z(t)* represents the temporal profile of HbO_2 or Hb changes at each measurement channel, *f(t)* is the predicted stimulation-specific response and is

expected to match the profiles of measured signals, *h(t)* is a given HRF, and *s(t)* is the stimulation-specific boxcar function for a given task. Moreover, *β* is the estimated amplitude of HbO_2, while εis an error term to account for any residual due to the mismatch between the actual data and the model. By fitting equation (2.1) to the temporal profile of HbO_2 obtained from each channel from each participant, I would be able to obtain (i) the estimated amplitude, (ii) its variance, and thus (iii) a statistical t-value representing the statistical significance of the brain activation at each respective channel.

Ideally, the HRF derived from the fNIRS signals via an event-related experimental paradigm would be appropriate for this study. However, to the best of my knowledge, such an HRF is not available for attention-evoked responses in the prefrontal cortex. Therefore, I used a standard HRF derived from BOLD fMRI as a surrogate (Glover, 1999). By fitting the predicted stimulation response function to the channel-wise, temporal profiles of HbO_2 responses, the amplitudes (expressed by *β*-values in μM) of prefrontal activations or deactivations in response to each Stroop task were obtained.

2.3.3.6 Random effects

For group-level hemodynamic measures, *β*-values at each channel were calculated by aver-aging *β*-values across each group of the subjects. Random-effect analysis was performed in order to generate statistically meaningful quantities at the group level. This was accomplished by conducting the one-sample t-test on *β*-values from all subjects at each channel for each subject group. For both control and PTSD subjects, group- level t-statistic analysis parameters (expressed by t-values) were obtained to show statistically increased and/or decreased brain activations during Stroop1 and Stroop2

tasks when compared to the baseline readings. To identify the regions showing significant differences in brain activations or deactivations between the control and PTSD groups, two sample t-tests were performed on *β*-values obtained from individual subjects. Both t-statistic values (expressed by t-values) and p-values were derived from the t-tests for each channel and used to generate t-maps in topographic images.

2.3.3.7 Topography.

Topographic images of prefrontal activations and/or deactivations were generated using EasyTopo, an optical topography toolbox (Tian et al., 2012). EasyTopo overlays 2D images of HbO_2 or Hb activations/ deactivations over a standard brain MRI atlas after 2D angular interpolation of the channel-wise activation data in a spherical coordinate system. In this study, the channel-wise β-values derived from GLM analysis and t-values from subsequent statistical comparisons were interpolated to generate activation maps (β-maps and t-maps) induced by Stroop1 and Stroop2 tasks.

2.4 Results

2.4.1 Behavioral measures

Table 2.3 reports the reaction times (i.e. average time taken to complete a block of 5 Stroop trials) of the control and PTSD groups for Stroop1 (i.e., neutral Stroop trials) and Stroop2 (i.e., incongruent Stroop trials) tasks (See Table 2.3). For statistical comparison of reaction times, Student t-test was used. As listed in Table 2.3, each group of healthy and PTSD subjects took significantly longer time to complete Stroop2 task than that to finish Stroop1 task. However, no significant difference in reaction times was

observed between the control and PTSD groups for either Stroop1 ($p = 0.41$) or Stroop2 ($p = 0.49$) tasks. Both groups responded to Stroop1 and Stroop2 with 100% accuracy.

Table 2.3. Task-dependent reaction times (sec) of control and PTSD groups

	Control group		**PTSD group**	
	Stroop 1	**Stroop 2**	**Stroop 1**	**Stroop 2**
Reaction time (Mean ± SD)	4.78±0.62	6.28±0.74	5.06±1.12	6.54±1.27
p value within each group	$<10^{-6}$		$<10^{-4}$	
p value between two groups	> 0.41	> 0.49		

2.4.2 Hemodynamic responses.

2.4.2.1 HbO_2 changes induced by Stroop1 and Stroop2 tasks in control group

For healthy controls, Fig. 2.3A shows a topographic image of prefrontal HbO_2 changes (β-map) by Stroop1 task, and Fig. 2.3C is a 3D rendered t- map ($p < 0.05$, FDR corrected) to display brain regions where the HbO_2 changes are significantly different from the baseline readings induced by Stroop1 task. Fig. 2.3A shows that during Stroop1 task, prefrontal regions towards the midline (line separating two hemispheres) are deactivated and lateral prefrontal regions are slightly activated. Similarly, Fig. 2.3B illustrates a topographic image of prefrontal HbO_2 β -map by Stroop2, and Fig. 2.3D marks regions where the HbO_2 changes are statistically different from the baseline readings (t-map, $p < 0.05$, FDR corrected). Close comparison between Fig. 2.3A,B hinted that the prefrontal β-map induced by Stroop2 exhibits a similar spatial pattern to that evoked by Stroop1 task. Further statistical analysis revealed that Stroop1 task did not stimulate any significant activations and/or deactivations in any channels (Fig. 2.3C), but Stroop2 task

resulted in significant alternations of HbO_2 in three distinct small regions, as shown in Fig. 2.3D.

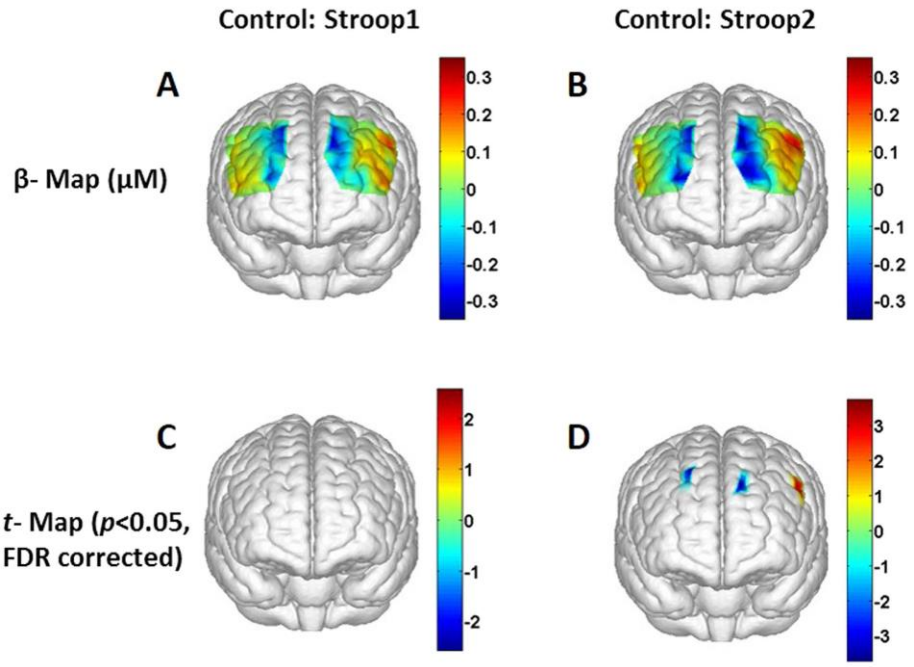

Figure 2.3. Topographic images of the task-evoked prefrontal activations derived from changes in HbO2 in control group. (A) Group-averaged prefrontal activation (β-map in μ M) evoked by Stroop1 tasks; (B) Group-averaged β-map (in μM) evoked by Stroop2 tasks. (C) A t-statistical map (t-map) that shows significant activations and/or deactivations (one sample t-test, $p < 0.05$; FDR corrected) on the brain template during Stroop1 tasks. (D) A t-map showing significant activations and/or deactivations evoked by Stroop2 tasks.

To be more specific for demonstrating deactivations and/or activations at the identified regions, I have shown group-averaged HbO_2 time courses evoked by Stroop1 and Stroop2 at channel 34 around the medial LPFC (see Fig. 2.4E,F for channel location), as shown in Fig. 2.4A,B, respectively. These two figures show clear reduction of HbO_2 responses in the cortical region near Channel 34 by both Stroop trials (i.e., neutral versus

incongruent trails) with very similar magnitude and temporal pattern, implying that no significant difference existed between HbO_2 responses by the two Stroop trials at this cortical region.

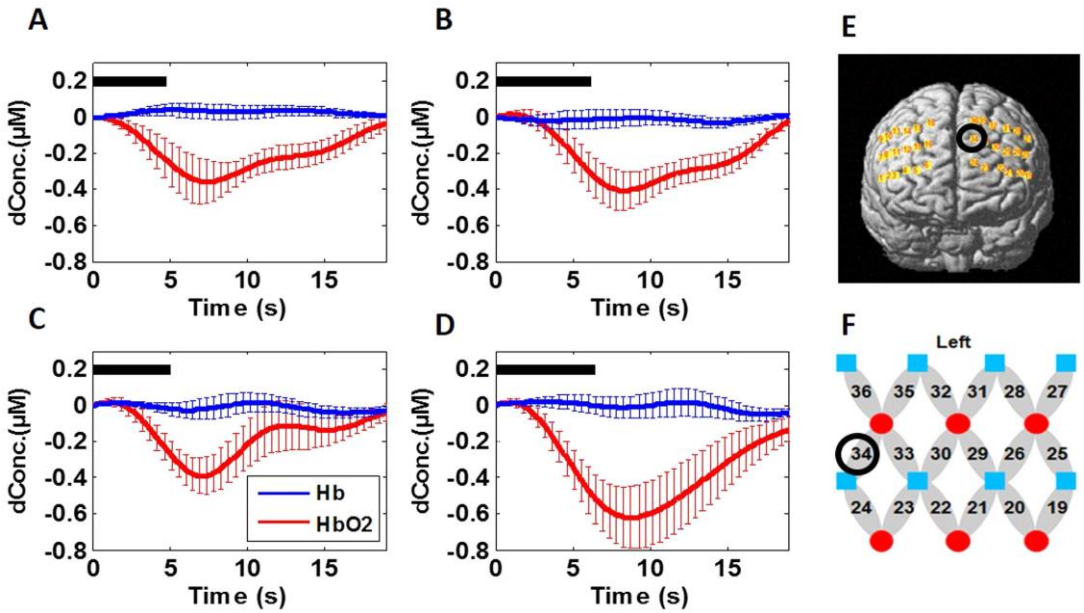

Figure 2.4. Mean Stroop-evoked hemodynamic changes of HbO2 in left DLPFC (i.e., channel 34 shown in Panels (E,F)) from both groups. (A,B) Group-averaged HbO_2 response from the healthy group evoked by Stroop1 and Stroop2 tasks, respectively. (C,D) Group-averaged HbO_2 response from the subjects with PTSD evoked by Stroop1 and Stroop2, respectively. In all four panels, the thick black bars represent the stimulation periods; the red lines represent the mean time courses of HbO_2; the blue lines represent the mean time courses of Hb; the error bars represent the standard errors of mean. (E) It shows the position or location of channel 34 on a standard human brain template. (F) It shows the configuration of fNIRS channels on the left frontal cortex. Red circles represent light sources, blue squares represent detectors, and gray ellipses represent the nearest source-detector pairs (as channels) to measure the brain activities.

On the other hand, channel-wise data analysis revealed a significant increase in HbO_2 response ($p = 0.007$) near left LPFC (BA 44, Channel 27; see Fig. 2.5E,F for channel location). Then, group-averaged HbO_2 time courses were taken and plotted from channel 27 under both Stroop1 and Stroop2 tasks, as Fig. 2.5A,B show, respectively. Close visual inspection between these two figures suggests that Stroop2 evoked more HbO_2 signals than Stroop1, resulting in significant changes with respect to the baseline readings (as seen in Fig. 2.3D).

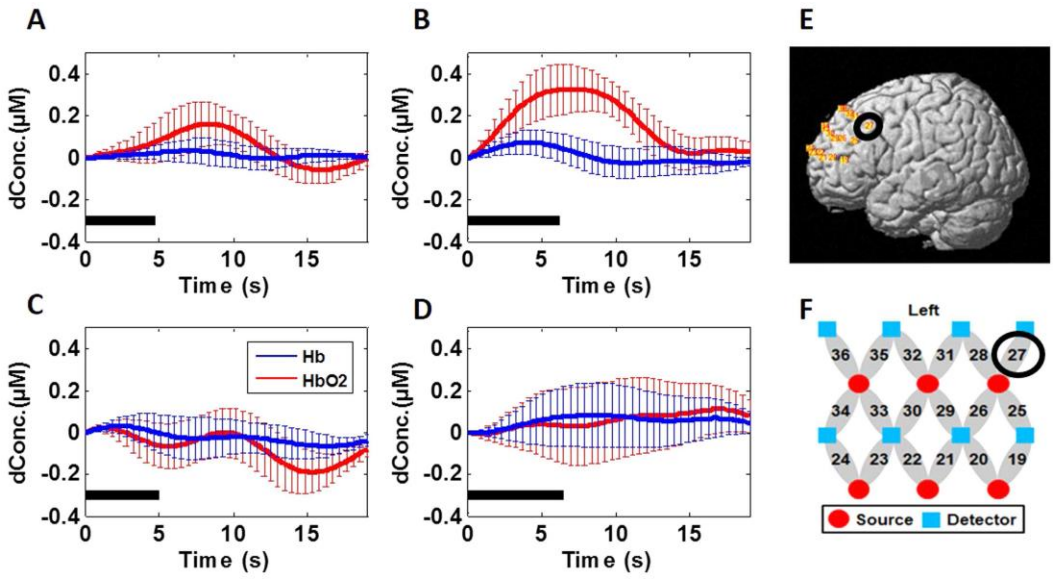

Figure 2.5. Mean Stroop-evoked hemodynamic changes of HbO_2 in left pars opercularis (see channel 27 shown in Panels E,F) from both groups. (A,B) Group-averaged HbO_2 response from the healthy group evoked by Stroop1 and Stroop2 tasks, respectively. (C,D) Group-averaged HbO_2 response from the subjects with PTSD evoked by Stroop1 and Stroop2, respectively. In all four panels, the thick black bars represent the stimulation periods; the red lines represent the mean time courses of HbO_2; the blue lines represent the mean time courses of Hb; the error bars represent the standard errors of mean. (E) It shows the position or location of channel 27 on a standard human brain template. (F) It

shows the configuration of fNIRS channels on the left frontal cortex. Red circles represent light sources, blue squares represent detectors, and gray ellipses represent the nearest source-detector pairs (as channels) to measure the brain activities.

2.4.2.2 HbO_2 changes induced by Stroop1 and Stroop2 tasks in PTSD group.

For the PTSD group, Fig. 2.6A shows a topographic image of prefrontal HbO_2 β-map by Stroop1 task, and Fig. 2.6C is a 3D rendered t-map ($p < 0.05$, FDR corrected) to mark regions that have significant HbO_2 changes from the baseline induced by Stroop1. Fig. 2.6A shows that prefrontal regions are mildly deactivated by Stroop1 task. Similarly, Fig. 2.6B illustrates a topographic image of prefrontal HbO_2 β-map by Stroop2. It is clear that deactivations induced by Stroop2 task are widespread across the prefrontal cortex. Fig. 2.6D marks regions where the HbO_2 changes are statistically different from the baseline readings (t-map, $p < 0.05$, FDR corrected). Overall, in the PTSD group, spatial extent of pre-frontal deactivation induced by Stroop2 task has been observed much larger than that induced by Stroop1 task.

To better understand and demonstrate deactivations and/or activations at the identified regions in the PTSD group, I have also plotted group-averaged HbO_2 time courses evoked by Stroop1 and Stroop2 at channel 34 (as I did for the control group in Fig. 2.4A,B), as shown in Fig. 2.4C,D, respectively. These two figures also show clear reduction of HbO_2 responses near the medial LPFC by both Stroop trials, with a larger deactivation magnitude by Stroop2 task. Regarding HbO_2 activation, for easy and quantitative comparison between the control and PTSD groups, I have also shown group-averaged HbO_2 time courses from channel 27 under both Stroop tasks, as Fig. 2.5C,D show, respectively. Close visual inspection between these two figures suggests that

neither of the Stroop tasks evoked much HbO_2 signals with respect to the baseline readings.

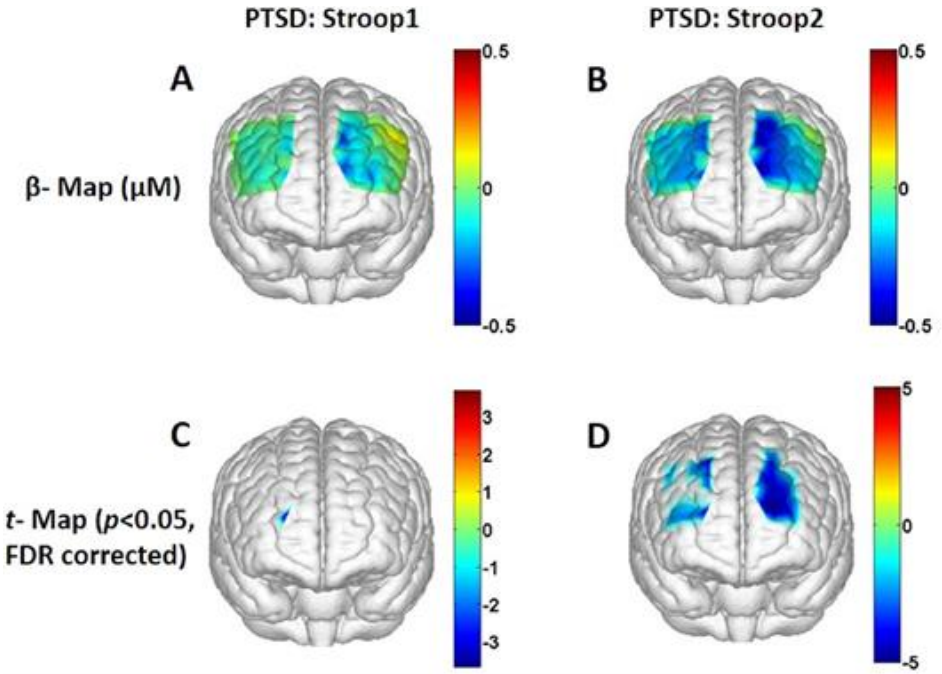

Figure 2.6. Topographic images of the task-evoked prefrontal activations derived from changes in HbO_2 from the PTSD group. (A) Group-averaged prefrontal activation (β-map in μM) evoked by Stroop1 tasks; (B) Group-averaged β-map (in μM) evoked by Stroop2 tasks. (C) A t-statistical map (t-map) that shows significant activations and/or deactivations (one sample t-test, $p < 0.05$; FDR corrected) on the brain template during Stroop1 tasks. (D) A t-map showing significant activations and/or deactivations evoked by Stroop2 tasks.

It is clear that deoxy-hemoglobin responses in both control and PTSD groups under both Stroop tasks were relatively low and insignificant (See Figs 2.4A–D and 2.5A–D). Therefore, Hb responses were excluded from further data analysis.

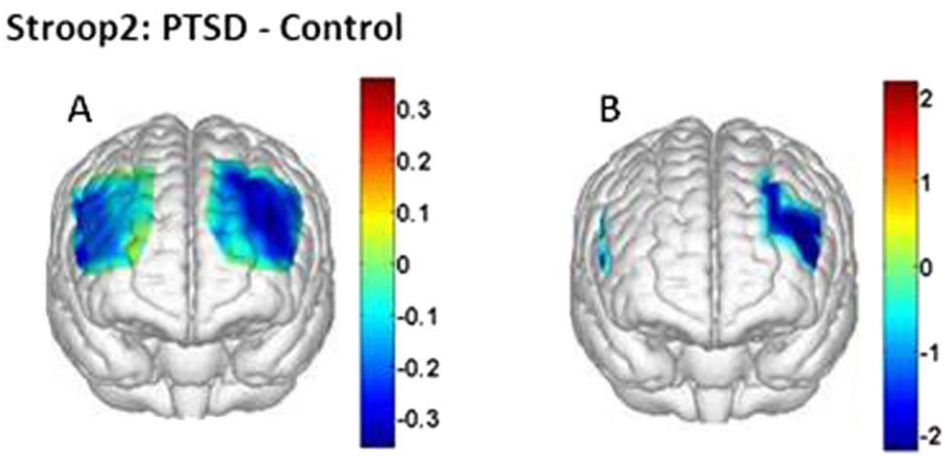

Figure 2.7. Topographic images of the prefrontal activations derived from HbO2, showing differences between the PTSD and control groups in response to Stroop2 (incongruent Stroop) tasks. (A) Group-averaged differences in activations or β-maps (in μM) between the two groups. (B) A t-map (p-value <0.1; FDR corrected) showing the regions of significantly different activations and deactivations between the groups.

2.4.2.3 HbO_2 changes induced by Stroop interference in control versus PTSD group

The main focus of this study was to explore differences of prefrontal hemodynamic signals in response to Stroop interference between a group of veterans with PTSD and age- and gender-matched healthy controls, in order to investigate possible deficits of selective attention processes in PTSD subjects. Furthermore, both Figs 2.3C and 2.6C do not show any significant cortical activation or deactivation evoked by Stroop1 task. Thus, I directed my attention to only Stroop2 task hereafter. Specifically, I found distinct differences of HbO_2 changes in both temporal and spatial patterns between the two subject groups only during incongruent trials. Figure 2.7A shows a differential topographic HbO_2 β-map between the PTSD and control groups, while Fig. 2.7B marks regions where the differential HbO_2 responses between the two groups are significantly different (t-map,

$p < 0.1$, FDR corrected) in response to incongruent Stroop trials. Specifically, channel-wise data analysis revealed that nine out of total 36 channels exhibited significantly reduced HbO_2 values in the PTSD group when compared to the control group. Two channels were located in right pars triangularis [Brodmann Area 45, Channels 1 ($p = 0.04$) and 7 ($p = 0.04$)]. Seven channels were located on the left LPFC: three on the left pars triangularis [BA 45, Channels 19 ($p = 0.02$), 25 ($p = 0.03$) and 26 ($p = 0.02$)] and four on the left dorsal LPFC (DLPFC) [BAs 9 & 46, Channels 20 ($p = 0.03$), 29 ($p = 0.02$), 30 ($p = 0.04$), 32 ($p = 0.03$)]. For better visualization of the mentioned channel locations, Fig. 2.2 presents the configuration and cortical position of the multi-channel fNIRS probe array.

2.4.2.4 Correlation between behavioral and hemodynamic measures

Linear regression analyses were performed between the task reaction times and corresponding HbO_2 response magnitude (i.e., β-values) at each channel during Stroop1 and Stroop2 tasks. For Stroop1 task, neither control nor PTSD group showed any significant correlation between the task reaction times and HbO_2 responses in any of the 36 channels. However, for Stroop2 task, two of total 36 channels exhibited a significant negative correlation between the task reaction times and HbO_2 responses from only the PTSD group, Those channels were located in left DLPFC [BA 9, Channels 28 ($R = -0.55$, $p = 0.03$) and 31 ($R = -0.52$, $p = 0.04$)]. The control group did not present a Stroop2-activated linear correlation between the task reaction times and HbO_2 responses.

2.4.2.5 Left DLPFC as Region of Interest (ROI)

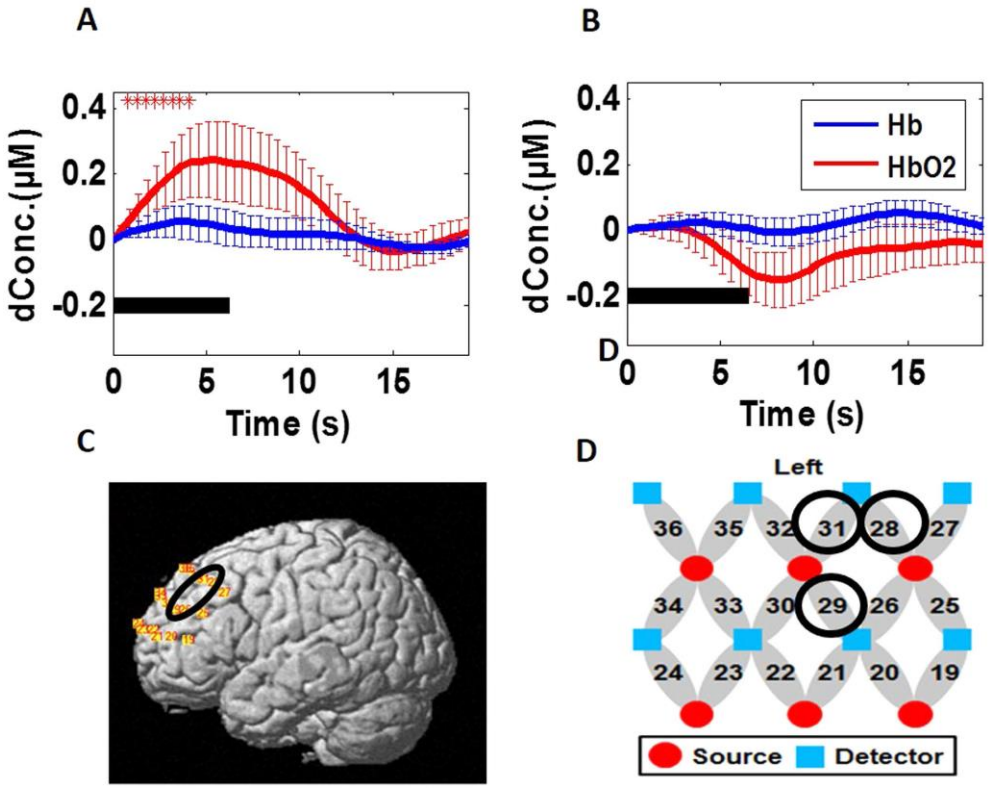

Figure 2.8. Mean Stroop2-evoked hemodynamic responses from the selected ROI, which includes channels 28, 29 and 31 from left DLPFC, from both groups. (A) Group-averaged, ROI-averaged HbO_2 responses from the control group evoked by Stroop2 tasks. (B) Group-averaged, ROI-averaged HbO_2 responses from the PTSD group evoked by Stroop2 tasks. In both panels, the thick black lines represent the stimulation period; the thick red lines represent the mean time courses of changes in HbO_2; the thick blue lines represent the mean time courses of changes in Hb; the error bars represent standard errors of mean. Asterisks '*' indicate significant ($p < 0.05$) HbO_2 responses with respect to the mean baseline at different time points.

While the above t-maps shown in Figs 2.3D, 2.6D and 2.7B were corrected by the FDR (false discovery rate), the correction was less stringent for Type I errors compared to the familywise error correction. In particular, the FDR-corrected confidence level for

Fig. 2.7B was set to be 90% with a p value less than 0.1. Therefore, it was necessary to perform an ROI-based data analysis according to recently published and accepted findings (Ehlis et al., 2005; Schroeter et al., 2003; Schroeter et al., 2002; Schroeter et al., 2004; Yanagisawa et al., 2010), which consistently reported bilateral LPFC activation with predominant activation in left LPFC due to Stroop interference (Schroeter et al., 2002; Yanagisawa et al., 2010).

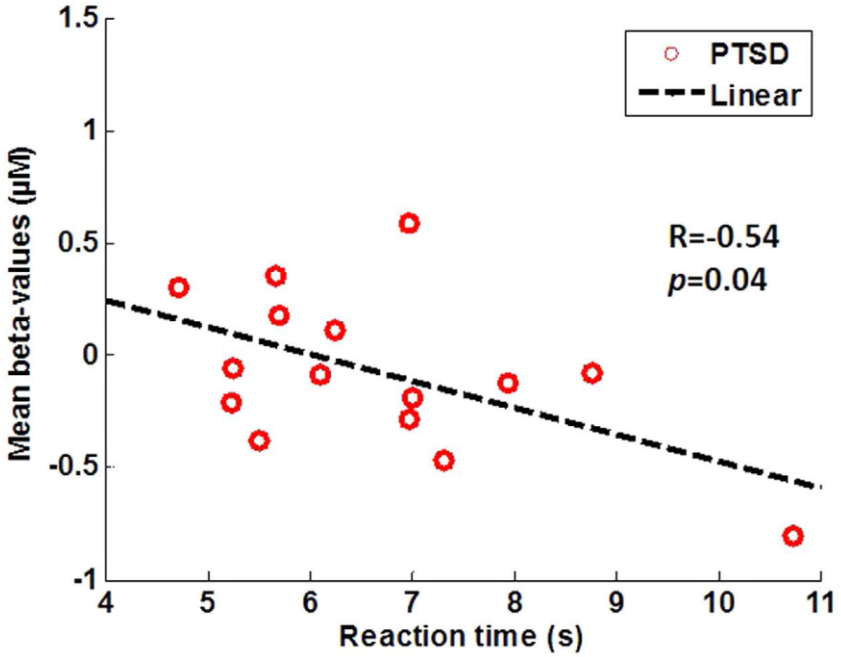

Figure 2.9. Correlation between individual task reaction times and ROI-averaged HbO2 responses (i.e., β-values) from the ROI (i.e., channels 28, 29 and 31) in the left DLPFC under Stroop2 task, taken from PTSD subjects.

In this current study, I thus selected Channels 28, 29 and 31 (See Fig. 2.8C,D for channel locations) as the ROI, which corresponded to the left DLPFC and roughly matched the activation sites in aforementioned studies. Given this ROI, I investigated the ROI-averaged HbO_2 signals induced by the incongruent Stroop task in both control and

PTSD groups. Fig. 2.8A,B plot group-averaged, ROI-based temporal HbO_2 responses from the control and PTSD group, respectively. The control group shows a Stroop2-evoked significant increase ($p < 0.05$) in HbO_2 response during the first several seconds of stimulation from the mean baseline within the ROI (See Fig. 2.8A), but the PTSD group did not show any significant difference in HbO_2 response from the mean ROI-averaged baseline (See Fig. 2.8B). Furthermore, Stroop2 task resulted in a marginally significant negative correlation ($R = -0.54$, $p = 0.04$) between the individual task reaction times and the ROI-averaged HbO_2 responses from the PTSD group (See Fig. 2.9) while no significant correlation was seen in the control group.

2.5 Discussion

2.5.1 Experimental Observations

The present study compared and contrasted prefrontal hemodynamic responses during the Stroop color-word neutral and incongruent tasks between the veterans with PTSD and age- and gender-matched controls. The observed results under the incongruent task are meaningful and thus summarized first as follows:

Observation 1: When being compared to the baseline, the healthy group exhibited significant hemodynamic activation in the left pars opercularis of control subjects (see Figs 2.3D and 2.5B).

Observation 2: When being compared to the baseline, both the healthy and PTSD groups showed significant hemodynamic deactivations, particularly in the bilateral frontal polar area (FPA) and bilateral DLPFC regions towards the midline (see Figs 2.3B,D and 2.6B,D).

Observation 3: The PTSD group presented reduced hemodynamic activity in the left DLPFC and bilateral pars triangularis (BA 45) significantly when being compared to the control group (see Fig. 2.7).

Observation 4: The ROI-based analysis confirmed that healthy subjects displayed significant hemodynamic activation in the selected ROI (i.e., left DLPFC) (see Fig. 2.8A), while the PTSD group did not show any significant hemodynamic activation or deactivation in the ROI during the same Stroop task (see Fig. 2.8B).

Observation 5: Regarding the brain imaging and behavioral relationship, I observed a marginally significant negative correlation between the task reaction time and HbO_2 response amplitude taken from the ROI of the PTSD group (see Fig. 2.9).

2.5.2 Interpretations

Interpretation for Observation 1: Activation of left pars opercularis by Stroop2 task in control subjects. Hemodynamic activations observed in this study in the LPFC regions, especially in the left DLPFC, were consistent with numerous fNIRS and fMRI studies that reported earlier neural correlates of Stroop interference (Banich et al., 2000; Ehlis et al., 2005; Schroeter et al., 2003; Schroeter et al., 2002; Schroeter et al., 2004; Yanagisawa et al., 2010). Particularly, a recent fNIRS study has demonstrated that Stroop interference evoked significantly the left DLPFC after acute bout of exercise, and that such increased activation in the mentioned cortical region in turn matched with improved Stroop task performance after the exercise (Yanagisawa et al., 2010). Therefore, it is reasonable to expect that cerebral hemodynamic activation in the left DLPFC is highly associated or linked with Stroop interference.

Interpretation for Observation 2: Deactivations in the bilateral FPA and bilateral DLPFC in both groups. In this study, I observed deactivations in channels from the DLPFC (BA 9) area towards midline and FPA (BA 10) during Stroop2 task in healthy subjects. However, the deactivations observed were not statistically significant compared to the baseline for most of channels (see Fig. 2.3D). For the PTSD group, more channels from similar DLPFC area towards midline and FPA illustrated deactivations (see Fig. 4D) than the healthy group. In comparison, functional NIRS study by Matsuda and colleagues reported deactivations in dorsal prefrontal cortex (DPFC, BAs 9 and 10) of adults and children during videogame tasks (Matsuda & Hiraki, 2006). This fNIRS study implicated that deactivations observed in DPFC were due to neural inhibition derived from continuous attention demand for video game tasks. A meta -analysis of 9 PET studies also reported regional cerebral blood flow (rCBF) decreases in medial frontal regions running along a dorsal-ventral axis (BAs 8, 9, 10 and 32), during 9 goal-directed tasks (such as spatial attention, visual search, and language tasks) (Shulman et al., 1997). The goal-directed tasks, which were analyzed in the meta-analysis report, had nothing in common except that all tasks required a response to certain visual stimuli. In an fMRI study, Mazoyer and colleagues demonstrated deactivations in dorsal medial prefrontal cortex (DMPFC; BAs 9, 10) during sustained attention to visual stimuli. In the meantime, a negative correlation between the load of sustained attention towards visual stimuli and blood oxygenation level dependent (BOLD) signal in DMPFC was reported as well (Mazoyer, Wicker, & Fonlupt, 2002). Based on those reported findings, therefore, it is reasonable to attribute the deactivations observed in this study as the response to visual stimuli or sustained attention to visual stimuli rather than Stroop specific deactivations.

Interpretation for Observations 3 and 4: Reduced response in left DLPFC in PTSD group than healthy group. For between-group differences in behavioral measures, I did not observe any significant difference in either performance accuracy or reaction times during Stroop interference task between the control and PTSD groups. However, in hemodynamic measures, during Stroop2 task, PTSD subjects showed significant reduction in HbO_2 responses in right pars triangularis (BA 45, Channels 1 and 7), left pars triangularis (BA 45, Channels 19, 25 and 26) and left DLPFC (BAs 9 & 46, Channels 20, 29, 30, 32) when compared to controls (see Fig. 2.7). This reduced response was expected since the control group exhibited significant activation in left lateral prefrontal regions, especially in the left DLPFC region to overcome Stroop interference, whereas the PTSD group failed to activate left lateral prefrontal regions. This result might implicate the difficulty experienced by PTSD subjects in coping up with Stroop interference. Therefore, restoration of left DLPFC activity in PTSD participants might improve their selective attention performance. Such improvements can be monitored and/or revealed by multi-channel fNIRS combined with the conventional Stroop color-word task.

The Stroop color-word test used in this study can also be thought as a measure of inhibitory control. Each participant performing this task had to inhibit the automatic or prepotent response of word naming in order to choose the appropriate color name of the word. During the Stroop2 color-word matching task, I observed significant reduction/deactivation in HbO_2 responses in bilateral pars triangularis (BA 45) in the PTSD group than in the control group. Pars triangularis is a part of ventrolateral prefrontal cortex (VLPFC). This reduction in VLPFC activations during Stroop2 task may suggest abnormal inhibitory mechanism in PTSD subjects. A recent fMRI study reported that

during the task involving inhibitory control (such as go-nogo task), PTSD patients exhibited reduced activation in the inferior frontal cortex, VLPFC and DLPFC relative to controls (Falconer et al., 2008).

Observation 5: Negative correlation between the brain imaging and behavior. Furthermore, results in this study illustrated that the brain responses within the selected ROI during Stroop2 task were negatively correlated with the reaction time (see Fig. 2.9) in the PTSD group. This observation may imply that the attenuated activations may be well correlated with inhibitory control. Several neuroimaging studies investigating neural correlates of emotion regulation have reported increased PFC activity and associated decrease in amygdala activity during successful emotion regulation (Delgado, Nearing, Ledoux, & Phelps, 2008; Erk et al., 2010; Lieberman et al., 2007; Ochsner, Bunge, Gross, & Gabrieli, 2002; Wager, Davidson, Hughes, Lindquist, & Ochsner, 2008). These published studies suggest that activities in several sub-regions of PFC, such as VLPFC and DLPFC, are involved in emotion control, including inhibition of Stroop interference. The reason for not being able to observe such a negative correlation in the control group could be attributed to the relative easiness of the tasks for the healthy subjects.

2.6 Limitation

A few limitations exist in this current study, including both the protocol design and technical limitations. In protocol design, Stroop1 task (i.e., neutral task) was too easy for the study, based on two experimental outcomes: (1) the brain responses to Stroop1 did not show any significant difference from the baseline readings, in both healthy and PTSD groups (see Figs 2.3C and 2.6C); (2) there was no significant difference in brain response

to Stroop1 between the healthy and PTSD group (see Fig. 2.4A vs 2.4C; Fig. 2.5A vs. 2.5C). Similarly, in behavioral measures, both groups took longer time to complete Stroop2 task when compared to Stroop1 task, as expected because of the Stroop interference effect. However, no significant difference in reaction times and accuracy was observed between the two groups (see Table 2.3). It is clear that more challenging or complex neural and interference Stroop tasks should be designed or used in future studies in order to gain better contrasts in brain responses between neutral/congruent versus incongruent tasks and between healthy and PTSD subjects.

Furthermore, there are three technical limitations in the present study. First, I had only a limited region of the prefrontal cortex covered by the fNIRS probe, so functions of other cortical regions involved during the Stroop tasks were not studied. Second, most veterans with PTSD in the study suffered from comorbid conditions, which could confound or bias the measured signals that were considered only from PTSD conditions. Lastly, it was possible that the fNIRS signals used for cerebral -hemodynamic quantification could include some contamination from extra cranial vasculature, such as from the scalp and skull. This contamination may be minimized by regression of the signals from superficial layers that are recorded with short source-detector separations of 0.8–1 cm.

2.7 Conclusions

In the present study, functional near infrared spectroscopy was utilized to assess the involvement of the prefrontal cortex in selective attention processes among 15 veterans with PTSD and 13 age-/gender- matched healthy controls. While performing Stroop (color-word) incongruent task, healthy controls showed hemodynamic activations

in lateral prefrontal cortex regions, especially in left DLPFC and left Pars opercularis, whereas veterans with PTSD failed to activate those cortical regions during the same Stroop task. These observations might implicate difficulty experienced by the PTSD subjects in coping up with Stroop interference. In addition, significant negative correlation was observed between task reaction times and HbO_2 responses from left DLPFC during color-word matching task. The present study clearly demonstrates that fNIRS is a portable and complementary neuroimaging tool to study the neural correlates of selective attention and interference in subjects with PTSD.

Chapter 3

A Preliminary Investigation Of Human Frontal Cortex Under Noxious Thermal Stimulation Over The Temporomandibular Joint Using Functional Near Infrared Spectroscopy

3.1 Abstract

Functional near infrared spectroscopy (fNIRS) was used to explore hemodynamic responses in the human frontal cortex to noxious thermal stimulation over the right temporomandibular joint (TMJ). fNIRS experiments were performed on nine healthy volunteers under both low-pain stimulation (LPS) and high-pain stimulation (HPS), using a temperature-controlled thermal stimulator. By analyzing the temporal profiles of changes in oxy-hemoglobin concentration (HbO) using cluster-based statistical tests, several regions of interest in the prefrontal cortex, such as the dorsolateral prefrontal cortex and the anterior prefrontal cortex, were identified, where significant differences ($p < 0.05$) between HbO responses to LPS and HPS were shown. In order to classify these two levels of pain, a neural network-based classification algorithm was utilized. With leave-one-out cross-validation, the two levels of pain were identified with 99% mean accuracy to high pain. Furthermore, the “internal mentation hypothesis” and the default-mode network were introduced to explain my observations of the contrasting trend, as well as the rise and fall of HbO responses to HPS and LPS.

3.2 Introduction

Pain is the primary symptom for physician consultations in the United States; it can significantly interfere with a person’s quality of life and general functioning (Breivik et al., 2008; Turk & Dworkin, 2004). Impairments in cognitive functioning, such as attention

control, working memory, mental flexibility, problem solving, and information processing speed, are observed in patients suffering from acute and chronic pain (R. P. Hart et al., 2003). Pain can also aggravate psychological attributes, such as depression, anxiety, fear, and anger (Bruehl et al., 2009). It is highly desirable to be able to quantitatively assess pain, which may aid patients suffering from chronic pain, and for patients who lack communication ability (e.g., infants and patients with a speech disability). However, because of the lack of a reliable quantitative measure of pain, it is often difficult for clinicians to evaluate the degree of pain to help guide its' clinical management.

In order to understand pain processing in humans, neuroimaging studies have been performed on the central nervous system using position emission tomography (PET) and functional magnetic resonance imaging (fMRI). Such studies have shown the involvement of pain in various cortical and subcortical regions of the brain (Casey, 1999; Peyron, Laurent, & Garcia-Larrea, 2000), which are often grouped together and referred to as the "pain matrix" (Mackey & Maeda, 2004; Neugebauer, Galhardo, Maione, & Mackey, 2009; Seminowicz, Mikulis, & Davis, 2004; Tracey & Mantyh, 2007; Zhuo, 2008), because they are highly associated during pain processing. The pain matrix includes the primary (S1) and secondary (S2) somatosensory cortices; they are known to be associated with sensory-discriminative aspects and additional affective/cognitive functions, respectively. Insular cortex and anterior cingulate cortex (ACC) are involved in affective-motivational and various cognitive aspects of pain, including anticipation, attention, and evaluation (Apkarian et al., 2005; Neugebauer et al., 2009; Ohara, Vit, & Jasmin, 2005; Seminowicz et al., 2004). Other prefrontal cortical and subcortical areas besides ACC, such as the amygdala, are also shown to play a role in secondary pain

effect, namely conscious awareness and cognitive evaluation of pain (Kulkarni et al., 2007; Neugebauer, Li, Bird, & Han, 2004; Ochsner et al., 2006; Price, 2000; Tracey & Mantyh, 2007). Thus, while the somatosensory cortex is shown to be primarily responsible for the perception of pain sensations, activity in the prefrontal cortex (PFC) during pain sensation is acknowledged as well (J. Lorenz, Minoshima, & Casey, 2003; Park, 2011). Also, a recent study has reported physiology-based pain measures using fMRI signal patterns, and demonstrated the feasibility of discriminating painful from non-painful stimulations (Brown, Chatterjee, Younger, & Mackey, 2011).

In the past decade, functional near infrared spectroscopy (fNIRS), a non-invasive optical imaging method, has been extensively investigated in the field of neuroimaging for studying functional brain activities. However, very little has been reported on pain processing measured by noninvasive fNIRS until a study by Becerra and colleagues (Becerra et al., 2009), which found qualitative correlations or relationships between pain and temporal characteristics of the hemodynamic responses observed by fNIRS in the sensory cortex. No finding however, has been reported to discriminate noxious pain from innocuous pain using fNIRS-derived signals seen at the PFC or frontal cortex. The aim of this present study was to therefore examine whether or not noxious and innocuous thermal pain can be objectively measured and discriminated by fNIRS measurements taken in the frontal cortical regions. The portable, easy-to-use, cost-effective, fNIRS-based brain imaging modality may have the ability to facilitate a better understanding of pain processing at the cortical regions induced by acute pain. my long-term goal is to utilize fNIRS as an objective imaging modality to explore and detect hemodynamic activities in the frontal cortical regions induced by pain, as well as to reveal if there exist

any characteristic distinctions in such hemodynamic signals between normal subjects and pain patients. Specifically, my study population focuses on patients with temporomandibular joint and muscle disorder (i.e., TMJMD), of which 75% of the US population experiences symptoms during their lifetime, according to the American Academy of Orofacial Pain. While the prevalence of TMJMD varies widely among studies, researchers surveying the prevalence literature estimated that, in any given year, 10% of women and 6% of men have TMJMD pain, which translates to some 20 million adults (Drangsholt & LeResche, 1999). Keeping my long-term goal in mind, I initiated this study by performing fNIRS measurements in the frontal regions of normal subjects who were under thermal stimulation by a computer-controlled thermode placed on each subject's skin over TMJ region. Channel-wise hemodynamic signals in response to two levels of thermal pain were quantified, analyzed, and compared, as reported in following sections.

3.3 Materials and Procedure

3.3.1 Subjects

A total of nine healthy volunteers from the University of Texas at Arlington (UTA) community were recruited for this study. The subjects taking part in the study were right-handed, and in the age range of 22–35 years. Prior to the study, none of the subjects had any neurological or psychological disorder, or were taking any kind of medications. Written informed consent was obtained from all the subjects before the measurement. The protocol used in the study was reviewed and approved by the Institutional Review Board at UTA.

3.3.2 Instruments

The instrument used for data acquisition was a multi-channel, continuous-wave, fNIRS imaging system (Cephalogics, Boston, MA; see Figure 3.1A), consisting of three 750nm and one 830nm light emitting diodes to form a source optode (Zeff et al., 2007). The detector optodes used in the system were connected to avalanche photo diodes. The head optode array utilized for the study consisted of 18 source optodes and 18 detector optodes (see Figure 3.3B,C for more details). For generating pain stimuli, I employed a temperature-controlled pain generator (MEDOC PATHWAY ATS MODE; see Figure 3.1B), which can generate a wide range of temperatures (–10°C to 55°C) in order to evoke various levels of innocuous and noxious pain.

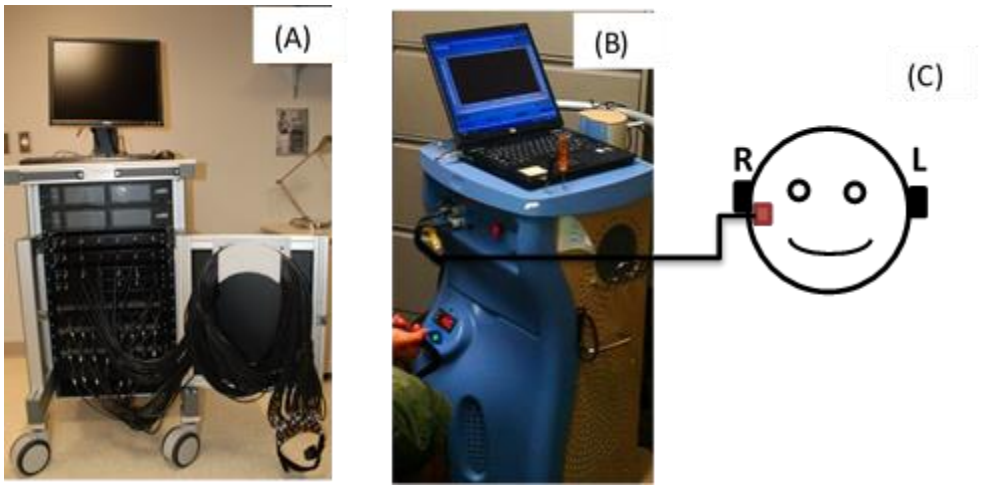

Figure 3.1. (A) A multichannel functional near infrared spectroscopy-based brain imager. (B) A temperature-controlled pain generator. (C) Placement of the thermode over the right side of each subject's temporo-mandibular joint region.

3.3.3 Experimental Paradigm

In order to estimate the magnitude of thermal pain to be applied, a staircase

approximation method was utilized when I first conducted pain perception estimation. A thermode of 16X16 mm^2 from the ATS thermal stimulator was attached to each subject's skin, over the right TMJ region (see Figure 3.1C), with variable temperatures from 41°C to 47°C. Using the visual analog pain rating scale (0–10), each subject was asked to rate the perception of pain before the actual pain-dependent measurements took place. Perception rating levels of 0, 3, 7 and 10 corresponded to no pain, low pain, high pain and extreme pain conditions, respectively. A linear correlation (R^2 = 0.98) between the stimulus temperatures (41°C-47°C) used and the average of pain perception rated by the nine subjects is presented in Figure 3.2. In the actual measurements, two levels of thermal stimuli (one rated at 3 and the other at 7) were selected. These pain stimuli are termed as low-pain stimuli (LPS) and high-pain stimuli (HPS), respectively. During fNIRS measurements, average temperatures over all the subjects to create the LPS and HPS were 43.0 1.4°C and 46.1 0.6°C, respectively.

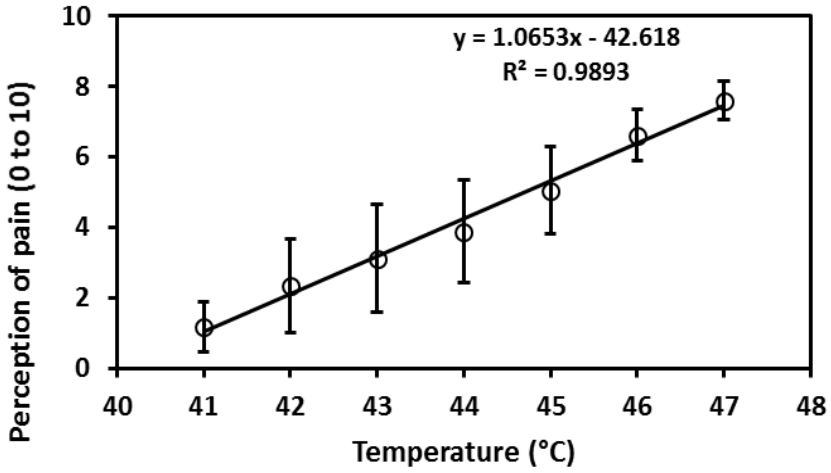

Figure 3.2. Linear correlation between pain stimulus temperatures (41–47°C) used and average of pain perception rated by nine subjects, when skin over the temporomandibular joint was thermally stimulated. Pain perception rating levels of 0, 3, 7, and 10

corresponded to no pain, low pain, high pain, and extreme pain conditions, respectively. Error bars are standard deviation of pain perception across nine subjects.

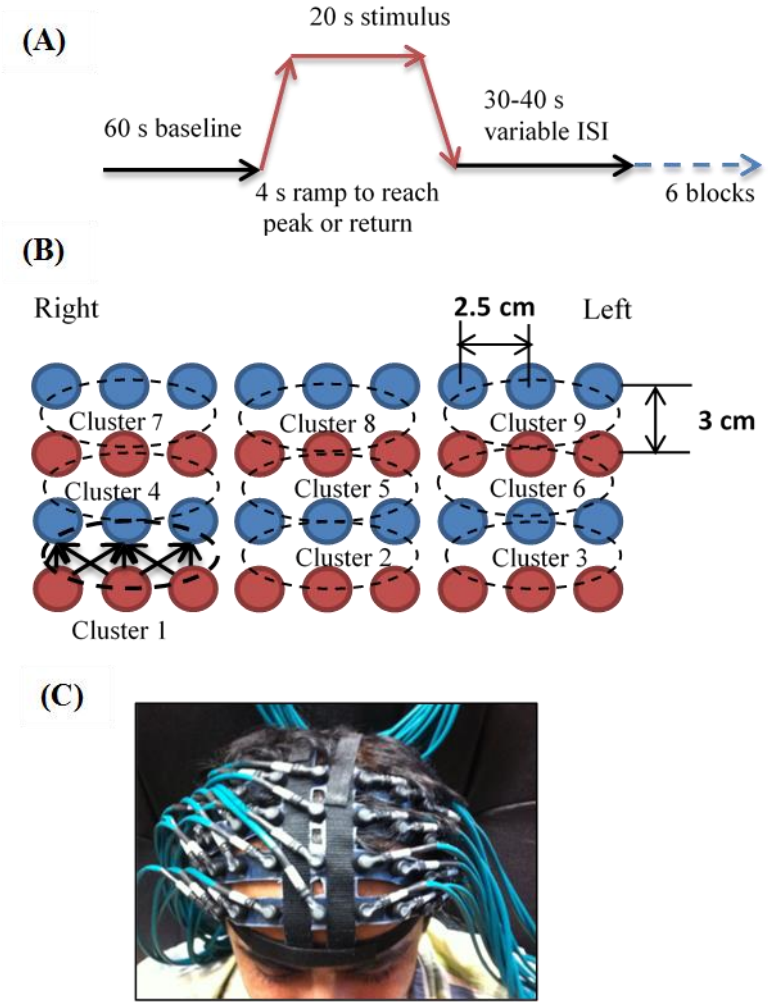

Figure 3.3. (A) Experimental paradigm used in this study for thermal stimulation. (B) Selection of nine clusters for data analysis. The first and third rows from the bottom represent light sources; the second and fourth rows from the bottom represent detectors. Solid black arrows (n = 7) are channels (source-detector pairs) grouped as one cluster. Right is each subject's right side. (C) Optical optode array placed on a subject's head with the geometry shown in Figure 3.3B.

The experimental protocol was a blocked design with variable inter-stimulus intervals (ISI). The paradigm had an initial baseline of 60 seconds, during which the temperature applied was 27°C, followed by a 4-sec ramp increase in temperature to reach the desired/designed stimulus temperature. Then, the temperature remained constant for 20 seconds, followed by a 4-sec ramp decrease in temperature to return to the baseline temperature. The complete protocol consisted of six blocks, each of which had a 30–40 seconds variable ISI between two adjacent blocks (see Figure 3.3A).

3.3.4 Data Acquisition

For data acquisition of fNIRS signals, 18 sources and 18 detectors (see Figure 3.3B) were placed on each subject's frontal cortex region (see Figure 3.3C). The distance between source-to-source, as well as detector-to-detector, horizontally was 2.5 cm. I obtained data from 75 source-detector pairs (i.e., channels), using the first and second nearest neighbors with 3 cm and 3.9 cm separations, respectively. The total area covered by the optode probe (TechEn, Inc., Milford, MA) on the brain was 20 X 9 cm^2 (see Figure 3.3C).

To find the corresponding neuro-anatomical positions of the optodes, an international 10–20 system of electrodes placement was used (Okamoto et al., 2004). Subjects were made to sit comfortably, and the distances between nasion (Nz) to inion (In), and left ear (AL) to right ear (AR), were measured, respectively. Also, the cross point between Nz-In and AL-AR, denoted as Cz, was identified. Using a marker, Nz, In, AL, AR, and Cz were highlighted and used as coordinate references for optode co-registration on a human brain template. The coordinates of all optodes along with Nz, In, AL, AR and Cz were recorded using a 3D Patriot digitizer (Polhemus Inc., Colchester, VT). A

MATLAB-based, open-source software (i.e., NIRS-SPM) was used to obtain spatial locations of the optodes on a human brain template (Ye et al., 2009). This software enabled us to identify each of the Brodmann Areas (BA) interrogated by the fNIRS optodes and the respective percentage of covered BA over the entire area of the optode array, as listed in Table 3.1. It is clear that my optode array covered seven major BAs: BAs 6, 8, 9, 10, and BAs 44, 45, 46, all of which took 96.62% of the area interrogated by the optode array. A very small portion of the optode array (1.52%) interrogated S2 (BA 43).

Table 3.1 Percentages of Covered BAs over the Entire Area of the Optode Array

Brodmann Area	Cerebral region	Percent (%)
3	Primary somatosensory cortex	0.06
4	Primary motor cortex	1.03
6	Premotor cortex	6.03
8	Frontal eye fields	14.60
9	Dorsolateral prefrontal cortex	24.96
10	Anterior prefrontal cortex	11.99
38	Temporopolar area	0.37
43(S2)	Secondary somatosensory cortex	1.52
44	Pars opercularis	5.56
45	Pars triangularis Broca's area	18.95
46	Dorsolateral prefrontal cortex	14.53
48	Retrosubicular area	0.41

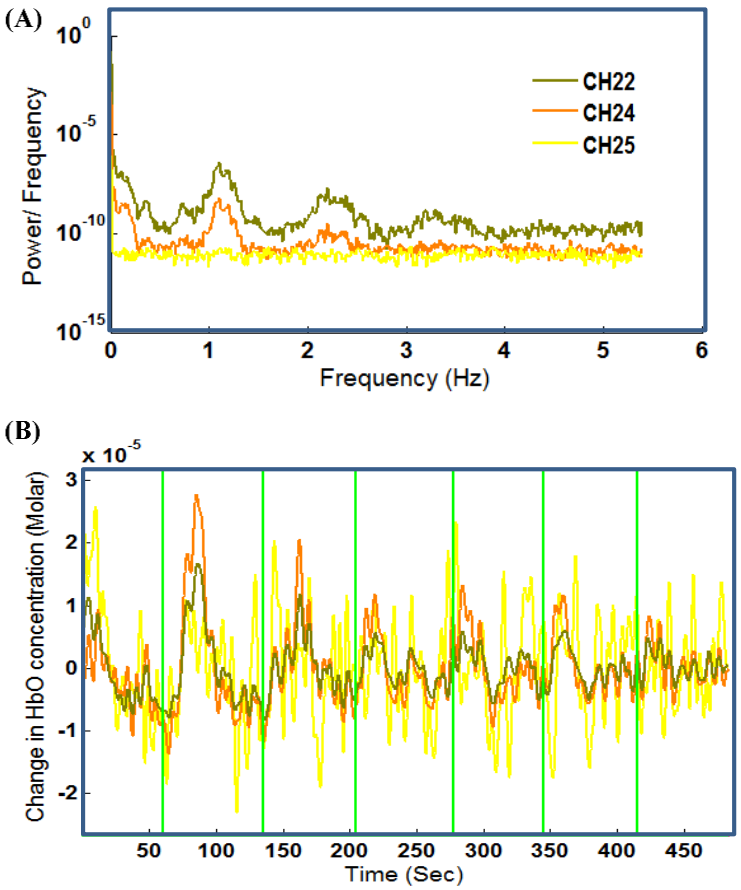

Figure 3.4. (A) Power spectral density (PSD) of raw optical intensities obtained from channels 22, 24, and 25, respectively, during high pain stimulation. (B) Temporal changes in oxy-hemoglobin concentration (HbO) obtained from channels 22, 24, and 25 during high pain stimulation. Green lines mark stimulus starting times.

3.3.5 Data Analysis

For processing the fNIRS data, an open-source, MATLAB-based software, called HomER, was used (Huppert et al., 2009). The raw optical intensities from all the channels were checked individually for each subject in order to identify any channels with large noise. The channels showing large noise were further inspected by performing power

spectral density (PSD) analysis on the raw optical intensities. An example is shown in Figure 3.4: Figure 3.4A displays PSD curves of two uncorrupted (channels 22 and 24) and one corrupted (channel 25) raw optical intensity profiles, while Figure 3.4B presents temporal changes in oxygenated hemoglobin concentration (HbO) from the corresponding channels during high-pain stimulation. It is seen that PSD of the two uncorrupted signals show a clear fundamental frequency around 1.1 Hz because of cardiac pulsation, whereas PSD of a noisy channel 25 does not exhibit any characteristic frequency. In order to exclude noisy channels from data analysis, I introduced a functional signal to noise ratio (fSNR) of changes in HbO for all channels; fSNR was defined as the averaged HbO value over the stimulation phase divided by the standard deviation (SD) of HbO during the 5-sec baseline prior to stimulation. The corresponding fSNR for channels 22, 24, and 25 were found to be 6.3, 6.1, and -2.3, respectively. Consequently, channels without the characteristic cardiac pulsation frequency and fSNR between -3 and 3 (i.e., signal magnitude < 3 SD) were considered to be noisy and were excluded from further analysis. The large noise may have resulted from various factors, such as the subject's high density or dark color of hair, imperfect probe placement on the scalp, and/or body motion artifact.

Apart from the signals coming from activation of the cerebral cortex, fNIRS signals may contain various other physiological components, such as systemic physiological noise caused by cardiac pulsation, respiratory signal and systemic blood pressure. Also, because of a relatively high sampling rate of the fNIRS system, the measured signals could include instrumental noise as well (Jang et al., 2009). Thus, to remove such noise within the fNIRS signals, as well as to correct the low-frequency baseline drift, the optical

signals were band-pass filtered from 0.01 to 0.2 Hz. Then, using the stimulus timing information, the fNIRS signals were averaged over the six blocks: the averaged temporal block had a time span of 65 seconds, namely 5-sec pre-stimulus, followed by 28-sec stimulation, and 32-sec recovery (see Figure 3.3). Averaging fNIRS signals over six blocks for each of the channels was performed in order to improve the signal-to-noise ratio. Last, the temporal profiles of HbO and deoxygenated hemoglobin concentration (HbR) were obtained for all the channels of each subject, using modified Beer– Lambert's law (Cope et al., 1988).

3.4 Results

After obtaining channel-wise HbO and HbR temporal files, spatially dependent hemodynamic responses to the pain stimulation were obtained. Specifically, all the channels were grouped into nine different clusters (see Figure 3.3B), covering the PFC and major regions of the frontal lobe (see Figure 3.3C). Each cluster consisted of seven channels. For group-level cluster analyses, the temporal profiles of seven channels in each cluster were averaged first for each subject, and then further averaged across all nine subjects. The grand-averaged temporal profiles of HbO signals for all the clusters are labeled as C1, C2, . . . , and C9, as shown in Figure 3.5, in response to both LPS and HPS. Clusters C1, C4, and C7 are on the ipsilateral (right) side of the frontal lobe with respect to the stimulation side; C3, C6, and C9 are on the contralateral (left) side; C2, C5, and C8 are located around the medial portion of the forehead. In most of these clusters, the temporal profiles of HbO in response to LPS (blue curves) show a slight decrease in HbO concentration during the stimulus period, followed by recovery to baseline. However,

the temporal profiles of HbO in response to HPS show a slight increase in HbO concentration during the stimulation phase, followed by a noticeable decrease in HbO during recovery before returning to baseline. In the meantime, the grand-averaged temporal profiles of HbR signals for all the clusters are shown in Figure 3.6, demonstrating little changes in HbR signals in response to either LPS or HPS, during or post stimulation.

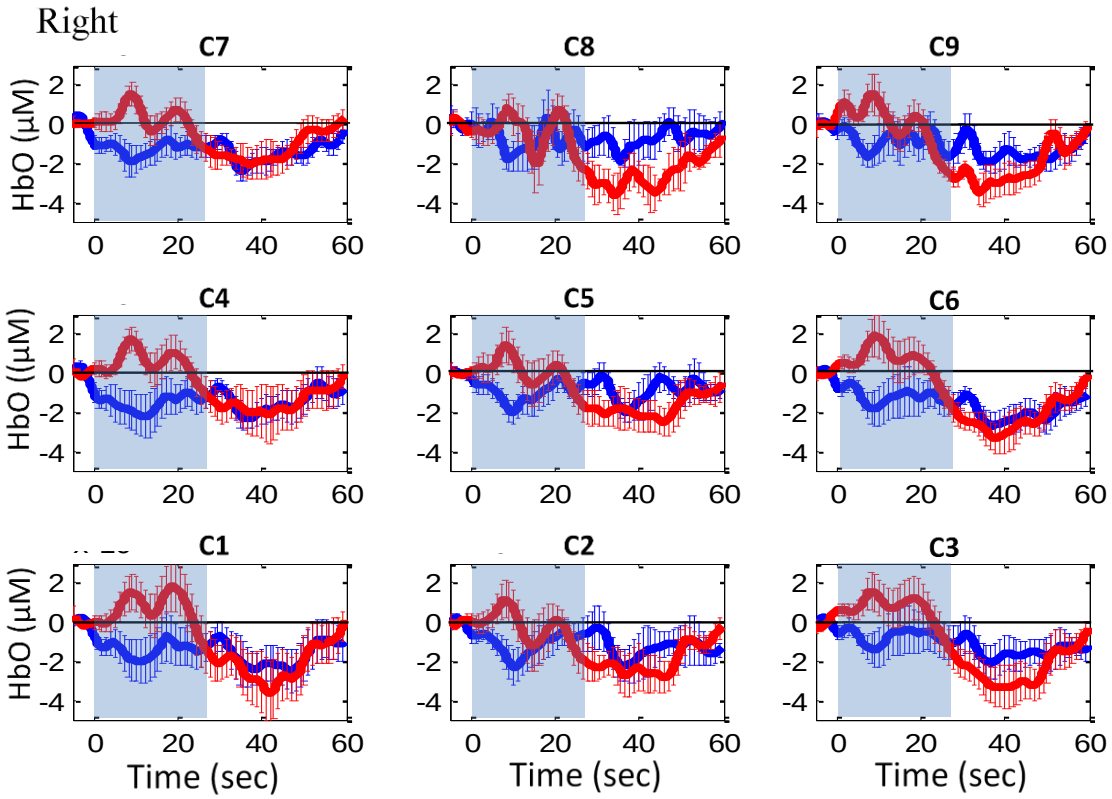

Figure 3.5. Grand average of temporal profiles of oxy-hemoglobin concentration (HbO) (in microMolar) across nine subjects under temporomandibular joint (TMJ) thermal stimulation, for all clusters (labeled as C1, C2 . . . C9). Dark and light colored curves represent grand-averaged temporal profiles of HbO in response to low pain and high pain stimulation, respectively.

In order to understand the spatial coverage of fNIRS optode array on the frontal

cortex, I present a 3D-rendered human brain map with BAs labeled ("Brodmann Areas . . ." 2013) and also mark optode locations on the human brain template (see Figure 3.7). As listed in Table 3.1 earlier, large portions of the optode array covered the anterior PFC (BA 10), dorsolateral PFC (BAs 9 and 46), frontal eye fields (BA 8), as well as BAs 45 and 44. By comparing the two panels in Figure 3.7, I expect that the clusters C3 and C6 (also C1 and C4) possibly cover the left (right) side of BAs 10, 9, 46, 45, and 44, while C9 (and also C7) may cover some portions of BA 8 and BA 6. While BA 43 (i.e., S2) is not clearly covered by the optodes, it is in the vicinity of clusters C6 and C9 (see Figure 3.7B). According to Table 3.1 and Figure 3.7, it is possible that signals obtained at clusters C9 and C7 may include small contribution from S2 because of the scattering or diffuse nature of light in tissue.

To identify hemodynamic signals in different cortical regions induced by HPS and LPS, areas-under-the-curve (AUC) within a selected time window (0–20 seconds) for each HbO profile in each cluster was calculated as the average concentrations of HbO during the thermal stimulations. Statistical comparison of AUC in response to LPS or HPS and baseline was conducted using paired *t* tests (N = 9) for each cluster individually. Statistical analysis of the AUC demonstrated that significant differences in AUC of HbO temporal profiles between the response to LPS and baseline occurred in clusters C4 ($p < .05$), C6 ($p < .05$), C7 ($p < .03$), and C9 ($p < .03$) during the 20-sec stimulation phase. The HbO responses were significantly decreased during LPS when compared with baseline. In contrast, significant differences in AUC of HbO profiles between the response to HPS and baseline occurred in clusters C3 ($p < .05$), C4 ($p < .05$), C6 ($p < .05$), C7 ($p < .05$), and C9 ($p < .01$) during the 20-sec stimulation phase, with significant increases

in HbO during HPS. Further statistical analysis revealed the most significant differences in AUC of HbO signals between the responses to LPS and to HPS occurred in clusters C3 ($p < .03$), C4 ($p < .02$), C6 ($p < .01$), C7 ($p < .01$), and C9 ($p < .01$) during the 20-sec stimulation phase. Then, only these clusters were chosen for the next step of data processing, namely, pain classification and discrimination. Note that C3, C6, and C9 were contralateral, while C4 and C7 were ipsilateral, with respect to the pain stimulation side (i.e., over the right TMJ region). HbR signals were excluded from further analysis because they did not show significant difference between responses to LPS or HPS and baseline.

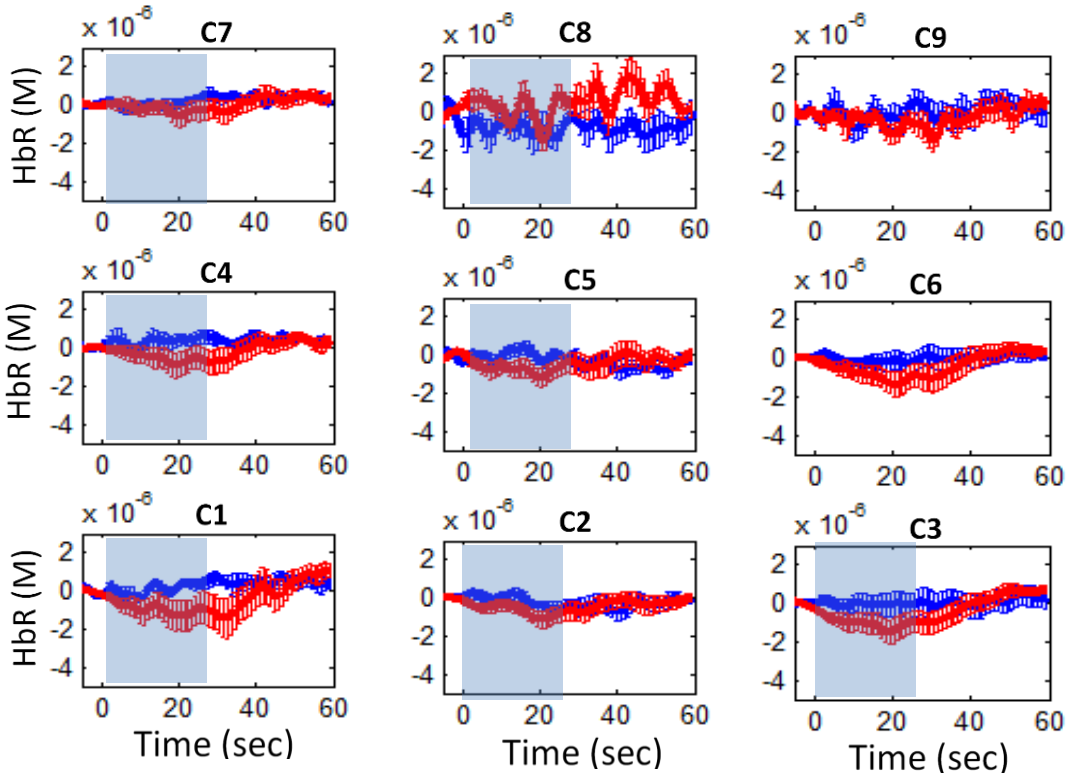

Figure 3.6. Grand average of temporal profiles of deoxygenated hemoglobin concentration (HbR) (in Molar) across nine subjects under temporomandibular joint (TMJ) thermal stimulation, for all clusters (labeled as C1, C2 . . . C9). Dark and light colored

curves represent grand-averaged temporal profiles of HbR in response to low pain and high pain stimulation, respectively.

3.4.1 Pain Classification

A multilayer perceptron (MLP) neural network-based classification algorithm was used to classify two levels of pain. Figure 3.8 provides an overview of the classification steps. In this procedure, only those clusters (C3, C4, C6, C7, and C9), which showed significant difference between LPS and HPS, were considered.

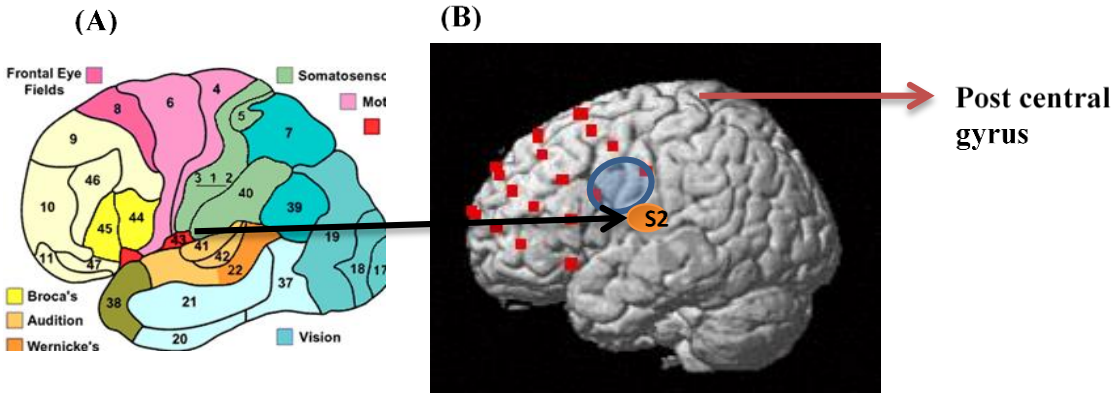

Figure 3.7. (A) A standard human cortex surface map marked by Brodmann areas ("Brodmann Areas . . ." 2013). (B) Brodmann areas covered by the optical optode array on the frontal cortex; it was obtained by marking the optode positions with a 3-D digitizer. Small solid squares are the optode positions superimposed on the brain template. The shaded portion around the center represents the area/volume interrogated by a particular source-detector pair.

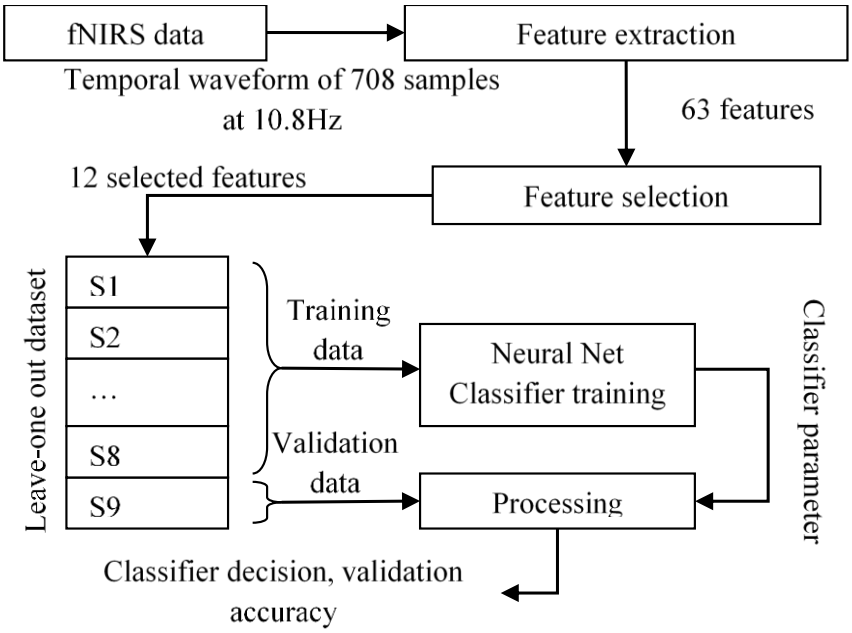

Figure 3.8. Classification flowchart, including (1) feature extraction to reduce 708 temporal points to 63 features, then (2) feature selection to further reduce features to 12 time points, followed by leave-one-out cross-validation using neural net classifier training.

The block averaged temporal curve of a cluster had 5 seconds of baseline prior to the stimulus, followed by 28 seconds of stimulus including a ramp increase and decrease in temperature, and followed further by 32 seconds of recovery. In total, I had 90 (5 clusters x 2 classes x 9 subjects) of 65-sec temporal curves, 45 each for the LPS and HPS classes, respectively, which were used to perform pain classification and cross-validation.

3.4.2 Feature Selection and Feature Extraction

Because 708 data points in a temporal curve (i.e., a 65-sec profile with a data acquisition rate of 10.8 Hz) from each cluster were too many to be used for pain

classification, it was necessary to down-sample the data points by more than 10-fold. To do so, each temporal curve was averaged in temporal blocks of approximately 1.1 seconds each, to produce 63 time points or features. Then, these selected features were the input to a feature-extraction algorithm. In order to find near-optimal feature subsets, the 63 features were evaluated using the piecewise linear orthonormal floating search (PLOFS) algorithm (Li, Manry, Narasimha, & Yu, 2006). PLOFS comprises: (1) the floating search subset generation algorithm; and (2) a piecewise linear network's mean-squared error (MSE) to calculate the subset evaluation function (Chandrasekaran & Kim, 1999; Fukunaga, 1990; Pudil, Novovicová, & Kittler, 1994; Yuc & Manry, 2007). PLOFS is a wrapper-based approach to feature selection (Kohavi & John, 1997). The feature selection algorithm yielded the best subset of features between sizes 1–63, and also calculated their performance. On the basis of the performance error, the subset of size 12 (or 12 features corresponding to 12 specific time points) was found and selected to be the most appropriate. The top portion of Figure 3.8 illustrates these steps.

3.4.3 Classifier Design and Cross-Validation

A leave-one-out method for cross-validation was used to test the classification algorithm. In order to keep the training and validation data independent, all observations (i.e., five selected clusters) from a subject were treated as a single unit, which was used only in the training or validation process, but not for both. Specifically, in this study, nine leave-one-out data sets were generated by keeping one set of the nine subjects' data as a validation set, and the remaining eight as the training sets (see Figure 3.8). A feed-forward neural net classifier was trained for each cross-validation data set, and the

accuracy of each set was calculated. The network was trained using output weight optimization–hidden weight optimization (OWO–HWO; (Yu, Manry, Li, & Lakshmi Narasimha, 2006)).

Table 3.2 Leave-One-Out Cross-validation Results for Right Temporomandibular Joint Thermal Stimulation

Data set #	Sensitivity	Specificity	Accuracy	AUC
1	1	1	1	1
2	1	1	1	1
3	1	1	1	1
4	1	1	1	1
5	1	1	1	1
6	1	1	1	1
7	1	0.8	0.9	0.88
8	1	1	1	1
9	1	1	1	1
Mean	1.00	0.98	0.99	0.99
SD	0.00	0.07	0.03	0.04

AUC = areas-under-the-curve; SD = standard deviation.

In order to properly size the MLP during training, the number of hidden units was adjusted such that the validation error was minimized. The network produced an approximate probability for each possible classification outcome (Wan, 1990), of which the class with the highest probability was chosen to be the classification decision (Ruck, Rogers, Kabrisky, Oxley, & Suter, 1990). The classification accuracy was defined as the percentage of patterns correctly classified. In this way, several network configurations with different number of units in the hidden layer, and different number of training iterations, were evaluated during cross-validation process; the best configuration was chosen. An MLP with 10 hidden units trained for a single iteration produced the best

results.

Based on the cross-validation results, I was able to classify high pain from low pain, with a 100% mean sensitivity, 98% mean specificity, and 99% mean accuracy based on nine subjects' data (see Table 3.2) in response to thermal stimulation given on the TMJ. The corresponding receiver operating characteristics curve was obtained and is shown in Figure 9, with an AUC of 0.99.

3.5 Discussion

In this present study, temporal changes in HbO signals showed an initial activation in the frontal cortex during the high-pain stimulation phase, followed by deactivation during the recovery phase before returning to the baseline. In the meantime, deactivation was also observed during low-pain stimulation in the frontal cortex. Cluster-based analyses allowed us to investigate pain-induced HbO changes in different cortical locations. In this study, a comparison of characteristic parameter (i.e., AUC) of HbO temporal curves for all the clusters was performed. Significant differences ($p < .05$) in AUC of HbO temporal profiles between LPS and HPS conditions were observed in clusters C3, C4, C6, C7 and C9 during the stimulation phase (0–20 seconds), but not during the recovery phase (30–40 seconds). Specifically, Clusters C3 and C6, covering a sizeable portion of the left dorsolateral PFC (BAs 9 and 46), showed significant differences between the LPS and HPS conditions. Also, clusters C7 and C9, covering a portion of dorsolateral PFC (BA 9) and frontal eye fields (BA 8), showed significant differences in AUC of HbO signals between LPS and HPS within the stimulation period. While this study is at its preliminary phase, the results are promising and encouraging, indicating that fNIRS-derived hemodynamic responses are able to give rise to different

temporal characteristics in response to high-pain or low-pain stimulation in several cortical regions (such as BAs 9 and 46). Further confirmation and quantification of such cerebral signals in response to pain given at different pain levels, and at different body locations, will be further carried out and explored in future studies.

It should be noted that, because pain is a very complex neurological process and phenomenon, a variety of studies for a better understanding of pain and pain mechanisms have been conducted using neuroimaging tools. Several fMRI-based studies have recently revealed possible interrelationships between pain and brain functions. For example, Kong and colleagues reported significant increases in fMRI signals in a number of brain areas under HPS as compared with LPS (Kong et al., 2010). I also obtained the similar conclusion on several prefrontal cortical areas (i.e., BAs 8, 9, 10, 44, 45, and 46), as shown earlier in this paper. Another fMRI study demonstrated the role of the anterolateral PFC in expected and perceived control over pain (Wiech et al., 2006). It was also reported by a separate group that the dorsolateral PFC (DLPFC) and caudate nucleus were activated when healthy subjects made efforts to disengage from feeling of pain during constant thermal stimulation. This study suggested the crucial role of the caudate nucleus and PFC in the initiation and maintenance of suppression of pain, respectively (Freund et al., 2009). In addition, a PET-based study of pain demonstrated the influence of DLPFC on pain perception by modulating cortico-subcortical and cortico-cortical pathways (J. Lorenz et al., 2003). Relatedly, in order to obtain relief from intractable pain, surgical removal of PFC was performed on patients with treatment-refractory pain syndromes via cingulotomy or capsulotomy (Bouckoms, 1994; Davis, Hutchison, Lozano, & Dostrovsky, 1994; Talbot, Villemure, Bushnell, & Duncan, 1995).

All of these studies have clearly demonstrated that the PFC is one of the key elements in the “pain matrix” and plays a significant role in pain processing.

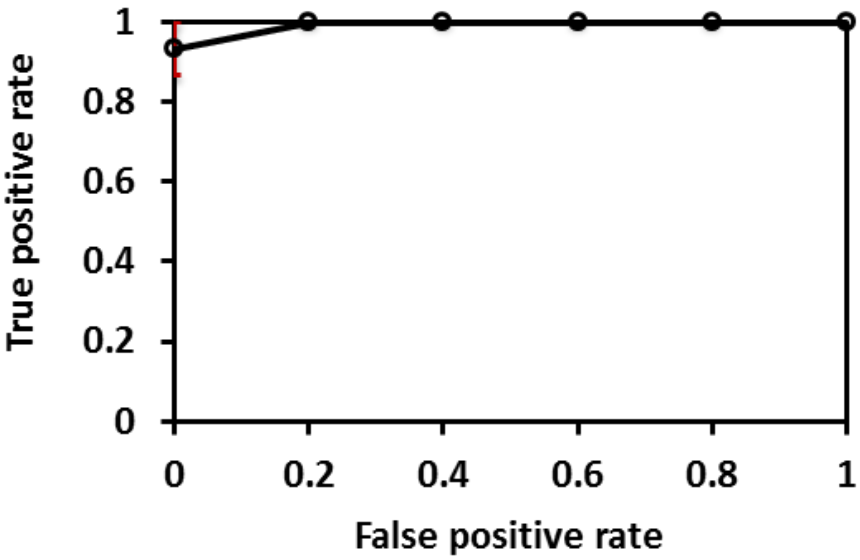

Figure 3.9. Receiver operating characteristics curve obtained using leave-one-out cross-validation for discrimination of high pain from low pain induced by thermal stimulation on the skin of under right temporomandibular joint (TMJ).

One of the interesting findings in this paper is the observation that LPS generated decreases in HbO responses in most of prefrontal cortical areas, namely, anterior PFC (BA 10) and DLPFC (i.e., BAs 8, 9, 44, 45, and 46), while HPS produced increases in HbO signals in the respective locations. This set of results is actually in excellent agreement with the report given by Kong and colleagues (Kong et al., 2010). They clearly demonstrated that LPS induced widespread brain deactivations in several key regions of the default-mode network (DMN), including bilateral BAs 8, 9, and 10 and many other subcortical areas, and that HPS induced brain activations in many cortical and subcortical regions, also including prefrontal regions of BAs 8, 9, 10, 44, and 46. The explanation for

the contrasting trend of brain responses to HPS and LPS was based on the understanding of DMN. DMN is an extensive network of brain structures that are engaged when individuals are left undisturbed as a baseline or default state, and attenuated during specific goal-directed behaviors (Gusnard, Akbudak, Shulman, & Raichle, 2001; Kong et al., 2010). The hypothesis and explanation given by Kong et al. works well for us to interpret and understand the HbO changes induced by HPS and LPS. The given and supported hypothesis is the “internal mentation hypothesis,” which states that “the DMN would support internally directed cognitive activity that is largely detached from the external world” (Kong et al., 2010, p. 8). According to this hypothesis, I expect that LPS may require the brain network to evaluate painfulness of LPS, resulting in the decoupling from the default mode and presenting deactivation in key regions of DMN. When HPS is given, however, the subject needs to instinctively find a potential solution to the current threat by partially counteracting the DMN inhibition.

Furthermore, the fact that HbO recovery trends during the post-stimulation phase in response to both HPS and LPS followed the same pattern without significant difference can be explained using the same argument or hypothesis. Regarding LPS, DMN restores its connection when the evaluation of painfulness is complete; so, the deactivated HbO functions within key regions of DMN recover gradually to their pre-LPS baseline. In case of HPS, HbO responses of the PFC network were increased during the stimulation period, but decreased during the post-HPS period. This was due to the demand to continuously evaluate painfulness with DMN suppressed and then to return to the default mode. Thus, during the recovery phase, HbO signals were reduced and then gradually returned to the pre-HPS baseline.

Besides the PFC, the bilateral activation in the secondary somatosensory cortex (i.e., S2) was reported by a magnetoencephalography study in response to unilateral painful heat stimulation applied to upper and lower limb of normal subjects, using a CO2 laser beam (Kakigi et al., 1995). In an fMRI study, bilateral activation in S2 was observed during mechanical-impact pain. These activations were significantly correlated with scores for the sensory discriminative component, demonstrating the crucial role of S2 in the sensory discriminative dimension of pain (Maihofner, Herzner, & Otto Handwerker, 2006). Consistently, it has recently been shown that Blood Oxygen Level Dependent (BOLD) signals taken only from S2 could give rise to 71.9% accuracy when classifying painful stimuli, significantly better than those when the BOLD signals from any other brain region were utilized for pain classification (Brown et al., 2011). All of these studies strongly indicate that S2 should be another important “pain matrix” element to consider in the future pain and pain-mechanism studies. In this study, as pointed out earlier, only a small portion of the optode array interrogated S2 (see Table 3.1 and Figure 3.7B), but it is possible that clusters C9 and C7 may include small contribution from S2 due to the scattering or diffuse nature of light in tissue.

In terms of further developing an objective measure of pain, a recent fMRI-based study was able to distinguish painful from non-painful thermal stimulation, with 81% accuracy using support vector machine learning on BOLD responses to thermal pain from several brain regions combined, including the PFC and S2 (Brown et al., 2011). In comparison, the present study was able to discriminate HPS from LPS, stimulated thermally on the TMJ, with 99% accuracy, using a multilayer perceptron-based classification algorithm. Specifically, I selected HbO responses from several key cortical

regions, which were within or near several key components of the “pain matrix,” namely the anterior PFC and DLPFC (i.e., BAs 8, 9, 10, 44, 45, and 46). the results of achieving high mean sensitivity, specificity, and accuracy (see Table 2) suggest that the anterior PFC and DLPFC play a significant role in pain processing, as reported by other groups, and thus may serve as biomarker locations for an objective measure to monitor and/or assess pain by fNIRS.

3.6 Limitations

Because this study was my first-step, preliminary investigation toward using fNIRS to quantify acute pain in control subjects, a few limitations need to be noted. First, the sample size was relatively small (n = 9); an increase in sample size in future studies will enhance the statistical power of the findings. Second, in the cluster-based analysis, the size of the clusters chosen (seven channels combined) was spatially large, so I could not identify very accurately the cortical sites or locations that showed strong HbO responses to pain stimulation. In particular, the cortical regions near S2 were not covered by the fNIRS optode array; otherwise, the discrimination between HPS and LPS might have been more distinct with an easier and more general classification algorithm. Future studies will need to either reduce the cluster size or co-register the optodes with a human brain template in order to better localize the pain-stimulated cortical regions with a good spatial resolution. Covering the S2 area more adequately in order to better detect sensory discriminative and affective/cognitive responses induced by pain is further needed. A third limitation was associated with the fact that, because this was my initial effort to apply a feature extraction/selection algorithm to fNIRS temporal patterns, the selected features used in pain classification might have been too specific or restrictive (i.e., only for thermal

stimulations over the subjects' right TMJ). It needs to be relaxed and valid with different types of pain stimulations at different body locations. Along these lines, more general temporal/spatial features can be identified through current feature extraction/selection algorithms, and be used to develop an effective classifier, suitable for a broad range of quantitative pain measurement and discrimination. Finally, while I acknowledge the depth limitation of fNIRS, my goal was to focus on the relationships between pain and cerebral/cortical activations/deactivations induced by pain. Once I can integrate additional subcortical, pain-processing knowledge with these fNIRS data, I will be able to gain a better understanding of pain mechanisms and pain pathways. The hope is that fNIRS-derived HbO signals taken in the PFC during pain sensation can serve as biomarkers for an objective measure of pain in the future.

Chapter 4

Prefrontal Hemodynamic Mapping By Functional Near-Infrared Spectroscopy In Response To Thermal Stimulations Over Three Body Regions

4.1 Abstract

Functional near infrared spectroscopy (fNIRS) was used to map and test the robustness of hemodynamic responses in the prefrontal cortex during noxious thermal pain, induced by thermal-stimulations over three different body regions over the: right forearm; right temporomandibular joint (TMJ); and left forearm. Functional NIRS measurements were obtained from three groups of healthy volunteers (one group for each body region). Each group was subjected to both low-pain stimulation (LPS) and high-pain stimulation (HPS) administered by a 16×16 mm^2 thermode of a temperature-controlled pain generator or thermal stimulator over the respective three mentioned body regions. During HPS, it was found that, in all three regions, changes in oxy-hemoglobin concentration (ΔHbO) in the prefrontal cortex, especially in the dorsolateral prefrontal cortex [i.e., Broadmann Areas (BA) 9 and 46], were significantly increased ($p<0.05$, False Discovery Rate corrected), with similar temporal patterns and spatial localizations. None of the three groups, however, exhibited any significant changes in HbO in the prefrontal regions under LPS. The observed prefrontal cortical activations induced by acute HPS were consistent with previous reports by fMRI-based pain studies. Furthermore, it was also revealed that there was a peculiar global trend of deactivation in the prefrontal cortex during the post-HPS period, which may be attributed to global vasoconstriction due to induction of acute nocuous pain. Overall, these results indicate that the temporal and

spatial characteristics of hemodynamic activities in the prefrontal cortex in response to actute thermal stimulation were robust across all three body regions. They have significant clinical implications for imaging the brain without the need for the constraints and patient phobias associated with remaining in a magnet chamber.

4.2 Introduction

4.2.1 Relationship between Pain and the Prefrontal Cortex

In order to understand pain processing in humans, functional neuroimaging studies using position emission tomography (PET) and functional magnetic resonance imaging (fMRI) have been performed on the central nervous system. Such studies have shown that pain processing involves various cortical and sub-cortical regions of the brain (Casey, 1999; Peyron et al., 2000) , which are often grouped together and referred to as the “pain matrix” (Mackey & Maeda, 2004; Neugebauer et al., 2009; Seminowicz et al., 2004; Tracey & Mantyh, 2007; Zhuo, 2008). The pain matrix mainly includes the primary (S1) and secondary (S2) somatosensory cortices, which are known to be associated with sensory-discriminative aspects and additional affective/cognitive functions, respectively. Sub-cortical regions, such as insular cortex and anterior cingulate cortex (ACC), are often involved in affective–motivational and cognitive aspects of pain, including anticipation, attention, and evaluation (Apkarian et al., 2005; Neugebauer et al., 2009; Ohara et al., 2005; Seminowicz et al., 2004). Prefrontal cortical and sub-cortical areas other than ACC are also shown to play a role in secondary-pain effects, namely, conscious awareness and the cognitive evaluation of pain (Ji, Fu, Ruppert, & Neugebauer, 2007; Kulkarni et al., 2007; Neugebauer et al., 2004; Ochsner et al., 2006; Price, 2000; Tracey & Mantyh,

2007). Although the somatosensory cortex is shown to be primarily responsible for the perception of pain sensations, activity in the prefrontal cortex (PFC) during pain sensation is acknowledged as well (J. Lorenz et al., 2003; Park, 2011). Recent fMRI studies have reported the role of the medial prefrontal area in pain encoding (J. Lorenz et al., 2003), and the role of the dorsolateral prefrontal area in expected and perceived control over pain (Wiech et al., 2006). Several other neuroimaging studies also demonstrated involvement of prefrontal cortical regions in pain processing, which includes the orbitofrontal gyrus, the dorsolateral prefrontal cortex, and the medial prefrontal cortex during acute pain in multiple chronic pain conditions, such as neuropathic pain and complex regional pain syndromes (Baliki et al., 2006; Becerra, Breiter, Wise, Gonzalez, & Borsook, 2001; Becerra et al., 2006; Geha et al., 2008; Lebel et al., 2008). Furthermore, the role of prefrontal regions in pain, placebo analgesia, and their modulations by analgesic drugs is also demonstrated (Craggs, Price, Verne, Perlstein, & Robinson, 2007; I. H. Lorenz et al., 2008). These studies provide us with the motivation to further explore the role of the prefrontal cortical regions in cognitive evaluation of pain by using functional near infrared spectroscopy (fNIRS).

4.2.2 Motivation of this Study

In the past decade, fNIRS, a non-invasive, portable, easy-to-use, cost-effective, optical-imaging method, has been extensively used in the field of neuroimaging for studying human brain functions. This complementary brain imaging modality may have the ability to facilitate a better understanding of pain processing at the cortical regions induced by acute pain. A better understanding of temporal and spatial characteristics of pain-induced hemodynamic responses might have potential applications in a clinical

setting where pain needs to be assessed objectively. A recent fNIRS-based pain study by Becerra and colleages found qualitative correlations or relationships between thermally-induced pain and temporal characteristics of hemodynamic responses in the somatosensory cortex (Becerra et al., 2009). Also, several other fNIRS-based pain studies have been reported to investigate prefrontal hemodynamic responses to mechanically-induced low back pain (Holper et al., 2014) and somatosensory hemodynamic responses to noxious electrical stimulation of the thumb (Yucel et al., 2015). However, to date, none of the fNIRS-based studies have reported robustness of prefrontal hemodynamic responses to noxious thermal stimuli over different body regions. In this present study, we mapped and examined hemodynamic responses in the prefrontal cortex of three groups of healthy subjects in response to thermal pain stimulations at three different body sites, by applying thermal stimulations over the: right forearm; right temporomandibular joint (TMJ); and left forearm. The results unambiguously showed robustness and consistency of hemodynamic activities in the prefrontal cortex under actute thermal stimulations administered at three different body parts. However, it was also revealed that there was a peculiar global trend of deactivation in the prefrontal cortex during the post pain-stimulation period, which needs to be further explored for its physiological mechanism.

4.3 Material and Methods

4.3.1 Subjects

A total of 16 adults (all males, right-handed, mean ± SD age = 24.8 ± 4.1 years) were recruited to study prefrontal cortical responses to the thermal stimulation given on the right forearm. A total of 9 adults (all males, right-handed, mean ± SD age = 25.5 ± 5.3

years) were recruited to study the prefrontal cortical responses to the thermal stimulation on the right TMJ. A total of 9 adults (all males, right-handed, mean ± SD age = 24.5 ± 3.8 years) were recruited to study prefrontal cortical responses to the thermal stimulation on the left forearm. The protocol used was reviewed and approved by the Institutional Review Board (IRB) of the University of Texas at Arlington (UTA). The methods were carried out according to approved guidelines by the IRB of UTA. Written informed consent was obtained from each of the participants before the thermal stimulation and the fNIRS measurements were performed.

4.3.2 Instruments

In this study, a continuous-wave, multichannel, fNIRS imaging system (Cephalogics, Boston, MA) was used, consisting of near infrared light emitting diode sources (at 750 nm and 850 nm) and avalanche photodiode detectors (Zeff et al., 2007). A head optode array consisting of 18 source optodes and 18 detector optodes [see Fig. 4,1(C) and 4.1(D)] was utilized to probe the human prefrontal cortex when the participants underwent two levels of (noxious and innocuous) thermal stimulation over three different parts of the body. A temperature-controlled pain generator (MEDOC PATHWAY ATS MODE) was utilized to produce a range of temperatures to evoke various levels of innocuous and noxious thermal stimulations.

4.3.3 Experimental Paradigm

In order to estimate the magnitude of thermal pain generated by the thermal stimulator, a thermode of 16×16 mm^2 from the stimulator was attached on the surface or

skin in the region of interest, such as on the arm or TMJ. Then, the temperature was varied between 41 °C to 48 °C with an interval of 1°C to generate thermal stimulation, which could be either innocuous or noxious. Next, using the visual analog pain rating scale (0-10), each participant was asked to rate the perception of pain before the actual pain-dependent fNIRS measurements were taken. Perception rating levels of 0, 3, 7 and 10 corresponded to no pain, low pain, high pain and extreme pain conditions, respectively. While taking pain-related fNIRS measurements, two levels of thermal stimuli (one rated at 3 and the other at 7) were used to induce low pain and high pain, which were termed as low-pain stimuli (LPS) and high-pain stimuli (HPS), respectively.

For noxious thermal stimulation over the right forearm paradigm, average temperatures over all the subjects (n=16) to create the LPS and HPS were 43.4±1.3 °C and 47.1±0.7 °C, respectively. For noxious thermal stimulation over the the right TMJ paradigm, average temperatures over all the subjects (n=9) to create the LPS and HPS were 43.0±1.4 °C and 46.1±0.6 °C, respectively. For noxious thermal stimulation over left forearm paradigm, average temperatures over all the subjects (n=9) to create the LPS and HPS were 42.1±1.1 °C and 46.0±0.6 °C, respectively.

The experimental paradigm was a blocked design, with variable inter-stimulus-intervals (ISI). The paradigm had an initial baseline period of 60 seconds, during which a 27 °C temperature was applied, followed by a 4-sec ramp increase in temperature to reach the destination stimulus temperature. Subsequently, the temperature remained constant for 20 sec, followed by a 4-sec ramp decrease in temperature to return to the baseline temperature. The complete protocol consisted of six blocks of stimulus-resting periods, with a 30-40 sec variable ISI between two adjacent blocks [see Figure 4.1(A)].

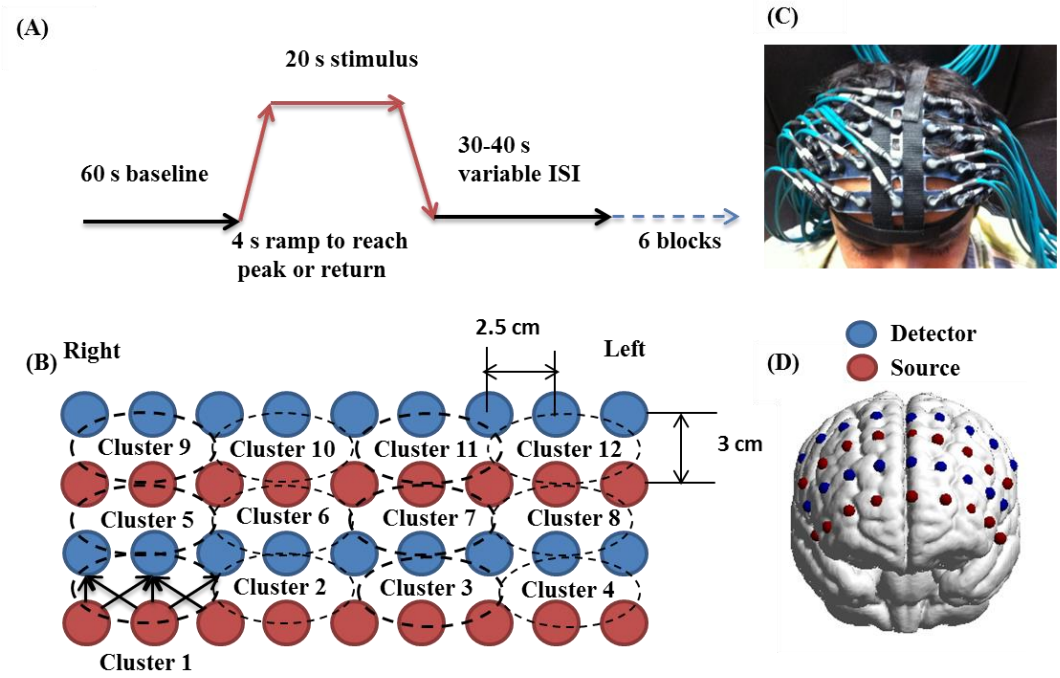

Figure 4.1 (A) Experimental paradigm used in this study for thermal stimulation. (B) Selection of 12 clusters for data analysis. Red circles are light sources, and blue circles are light detectors. Solid black arrows at the left bottom (n=6) show the six channels (source-detector pairs) grouped as one cluster. The word “Right” marks each subject’s right side. (C) Optical optode array placed on a subject’s head with the geometry shown in Fig. 4.1(B). (D) Co-registration of the light sources and detectors on a standard human brain template.

4.3.4 Data Acquisition

For fNIRS data acquisition, an optical optode array, consisting of 18 sources and 18 detectors, was placed on each subject’s prefrontal cortex region [see Fig 4.1(C)]. The distance between source-to-source, as well as detector-to-detector, horizontally was set as 2.5 cm. The nearest distance between source and detector vertically was 3 cm [see

Fig. 4.1(B)]. Using this probe geometry, I was able to obtain fNIRS signals from 75 source-detector pairs (i.e., channels) when the first and second nearest neighbors with 3 cm and 3.9 cm separations, respectively, were utilized. The total surface area covered by the optode probe on the frontal lobe was ~20×9 cm^2.

A co-registration procedure was applied based on four randomly-selected participants to estimate the frontal/prefrontal cortical regions covered by the fNIRS probe (Singh et al., 2005). After placing the fNIRS probe on each subject's forehead [see Fig. 4.1(C)], positions of five reference cranial landmarks, (i.e., the nasion, inion, left and right pre-auricular points, and vertex), light sources, and detectors, were measured or marked using a motion tracking system (PATRIOT, Polhemus, USA.). These cranial landmarks served as reference positions to convert the real-world stereotaxic coordinates of the optodes to the Montreal Neurological Institute (MNI) coordinates used in a standard brain MRI atlas, based on the affine transformation (Tian et al., 2012). Using NIRS-SPM software (Ye et al., 2009). Each of the Brodmann Areas (BA) probed by the fNIRS optode array, and the respective percentage of covered BA over the entire area of the optode array, were identified. It was observed that the optode array mainly examined seven major Brodmann Areas: BAs 6, 8, 9, 10, 44, 45, and 46, all of which covered 96.62% of the area interrogated by the optode array. The percentage of probe area covered by the premotor cortex (PMC; BA 6) is 6.03%, the percentage by the frontal eye fields (FEF, BA 8) is 14.60%, percentage by the frontopolar area (FPA; BA 10) is 11.99%, percentage by the dorsolateral prefrontal cortex (DLPFC; BAs 9 & 46) is 39.89%, and percentage by the ventrolateral prefrontal cortex (VLPFC; BAs 44 & 45) is 24.91%. Figure 4.1D shows the

registered optode positions (averaged over four participants) on the standard human brain atlas.

4.3.5 Data Screening and Pre-processing

The temporal profiles of light intensities obtained after fNIRS measurements were screened and pre-processed using a publically-available toolbox known as HOMER (Huppert et al., 2009). First, the raw light intensity signals were visually inspected to exclude blocks associated with motion artifacts. Then, the resultant signals free from motion artifacts were low-pass filtered at a cut-off frequency of 0.2 Hz to remove systemic or physiological noise (such as cardiac and respiratory oscillations) and electronic noise, and then high-pass filtered at a cut-off frequency of 0.01 Hz to exclude any possible baseline drift. Using the modified Beer-Lambert Law, changes of oxygenated and deoxygenated hemoglobin concentrations (i.e., ΔHbO_2 and ΔHb, respectively) relative to the baseline were quantified (Cope et al., 1988).

4.3.6 Data Analysis

To quantify cortical hemodynamic activities during the thermal stimulation, a model-based statistical analysis tool [namely, general linear model (GLM)] was utilized. Over the last several years, GLM analysis has been extensively used to analyze fNIRS data to identify cortical areas which are significantly activated during a given task (Hassanpour et al., 2014; Plichta et al., 2006; Tian & Liu, 2014; Ye et al., 2009). In GLM, a hemodynamic response function (HRF) is used to serve as a model to predict the

change in HbO signals due to task stimulation; GLM can be expressed by the equation (4.1):

$$z(t) = \beta f(t) + \mathcal{E}, \quad (4.1)$$

where, $f(t) = h(t) \otimes s(t)$. (4.2)

In equation (4.1), *z(t)* represents the temporal profile of ΔHbO or change in deoxyhemoglobin concentration (ΔHb) at each measurement channel; *f(t)* is the stimulation-specific predicted response which is expected to match the temporal profiles of measured hemodynamic signals (i.e., ΔHbO or ΔHb); *h(t)* is a given hemodynamic response function (HRF); and *s(t)* is the stimulation-specific boxcar function for a given task. Moreover, β is the estimated amplitude of ΔHbO, while ε is residual due to the mismatch between the actual data and the predicted model. By fitting the equation (4.1) to the temporal profile of ΔHbO obtained or measured from each channel of each participant, I would be able to obtain: (a) the estimated amplitude, β; (b) its variance, and thus (3), a statistical t-value representing the statistical significance of the brain activation at each respective channel. In this way, the amplitudes (expressed by β values in μM) of prefrontal or frontal activations or deactivations in response to thermal stimulation were obtained by fitting the predicted stimulation response function to channel-wise, temporal profiles of ΔHbO responses.

For group-level hemodynamic analyses, group-level β values at each channel were averaged over each group of subjects. Random-effect analysis was performed to generate statistically-meaningful quantities at the group level. For each of three measurement groups, it was accomplished by conducting the one-sample t-test on β values obtained from all subjects at each channel. In this way, a group-level t-statistic

(expressed by t-values) was obtained to show statistically increased and/or decreased brain activations during thermal stimulation compared to the baseline readings. Both t-statistic values and p-values were derived from the t-tests for each channel and used to generate t-maps in topographic images.

Topographic images of prefrontal activations and/or deactivations were generated using EasyTopo, an optical topography toolbox (Tian et al., 2012). It overlays 2D images of HbO or Hb activations/deactivations over a standard human brain MRI atlas after 2D angular interpolation of the channel-wise activation data in a spherical-coordinate system. The channel-wise β-values derived from GLM analysis and t-values from subsequent statistical comparisons were used to generate activation maps (i.e., β-maps and t-maps) induced by thermal stimulation over different body regions.

4.4 Results

4.4.1 Channel-wise HbO Data Analysis

After obtaining channel-wise HbO and Hb temporal profiles, spatially-dependent hemodynamic responses to the pain stimulation were obtained. Initially, all the channels were grouped into 12 different clusters [see Figure 4.1(B)], probing the prefrontal cortex [see Figure 4.1(D)]; each cluster consisted of six channels. Then, using the stimulus timing information, mean ΔHbO and ΔHb signals from each cluster were further averaged over the six temporal blocks: the block- averaged temporal profile of ΔHbO and ΔHb had a time span of 65 seconds, namely 5-sec prior to the stimulation, followed by 28-sec thermal stimulation, and ~35-sec recovery. For qualitative assessment of group-level

temporal hemodynamic responses, ΔHbO profiles were averaged (across six channels) within each cluster for each subject, and then further averaged across all subjects.

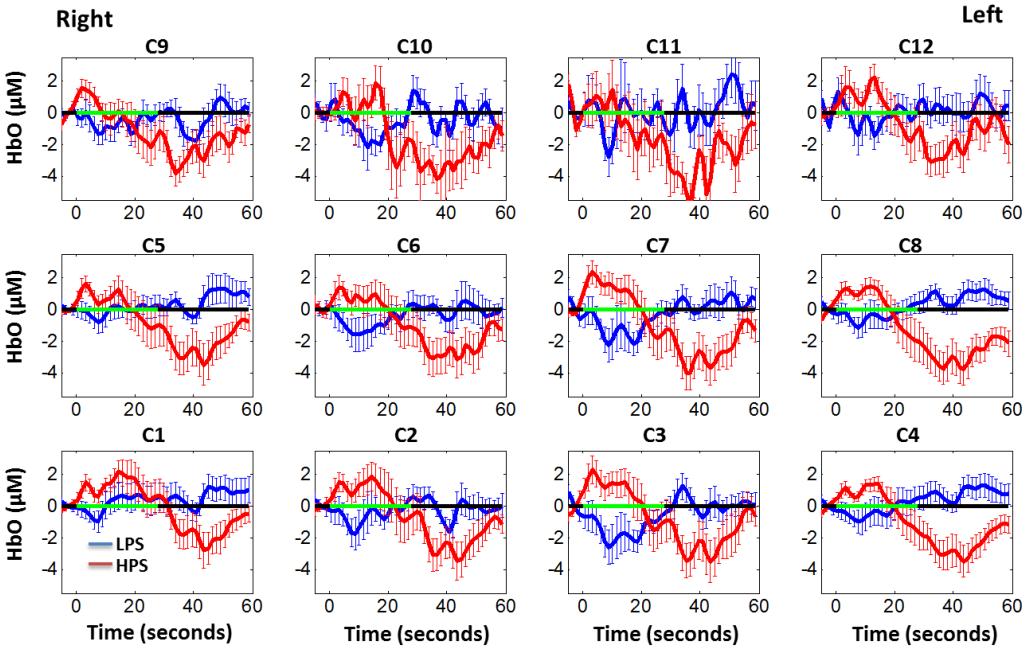

Figure 4.2 Group average of temporal profiles of ΔHbO concentration (in microMolar) across 16 subjects under the right forearm thermal stimulation, for all clusters (labeled as C1, C2 …. C12). Blue and red curves represent group-averaged temporal profiles of ΔHbO in response to low pain and high pain stimulation, respectively. Error bars are standard errors. Solid green lines represent the stimulation period.

The group-averaged temporal profiles of ΔHbO and ΔHb for all the clusters in response to both LPS and HPS are shown in Figures 4.2, 4.3, and 4.4, respectively, for the stimulations on (1) the right forearm, (2) the right TMJ region, and (3) the left forearm. Clusters are labeled as C1, C2 … C12. Clusters C1, C2, C5, C6, C9, and C10, are located on the right side of the frontal lobe, while C3, C4, C7, C8, C11, and C12 are located on the left side of the frontal lobe [see Figs. 4.1(B)]. In most of the clusters, the temporal

profiles of ΔHbO in response to LPS show a slight decrease in HbO concentration during the stimulation period, followed by recovery to baseline, in all the three groups [see Figs. 4.2, 4.3, and 4.4]. On the other hand, the temporal profiles of ΔHbO in response to HPS show a slight increase in HbO concentration during the stimulation period, followed by a decrease in HbO during the recovery period before returning to baseline. Overall, the temporal characteristics of prefrontal ΔHbO responses were consistent when thermal stimulation was applied to the right forearm, right TMJ region, and left forearm, separately [Compare Figs. 4.2, 4.3, and 4.4].

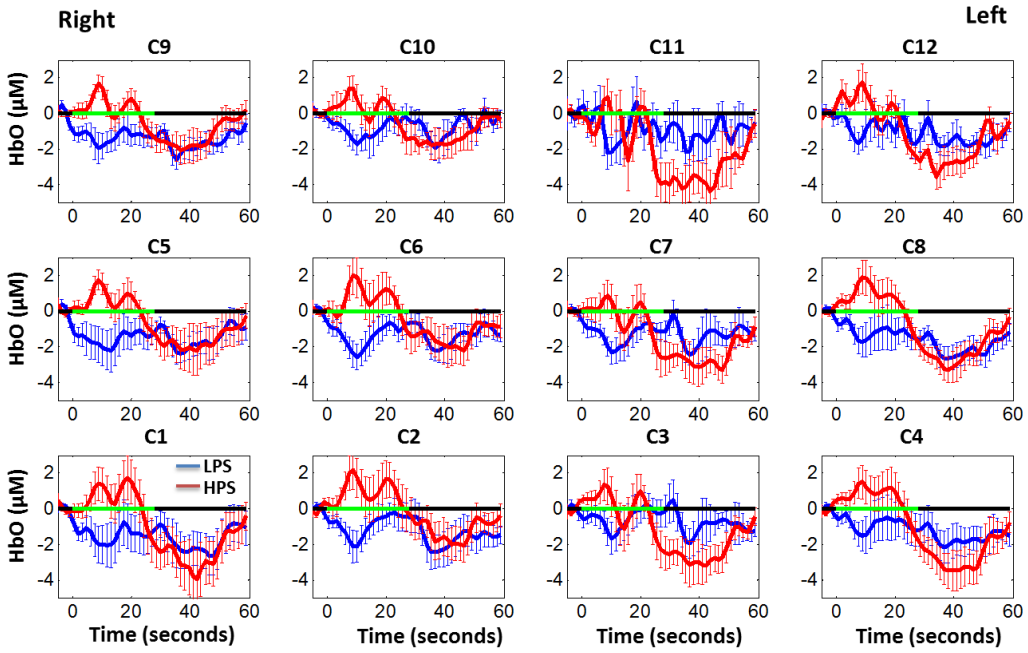

Figure 4.3. Group average of temporal profiles of ΔHbO concentration (in microMolar) across 9 subjects under right TMJ thermal stimulation, for all clusters (labeled as C1, C2 …. C12). Blue and red curves represent group-averaged temporal profiles of ΔHbO in response to low pain and high pain stimulation, respectively. Error bars are standard errors. Solid green lines represent the stimulation period.

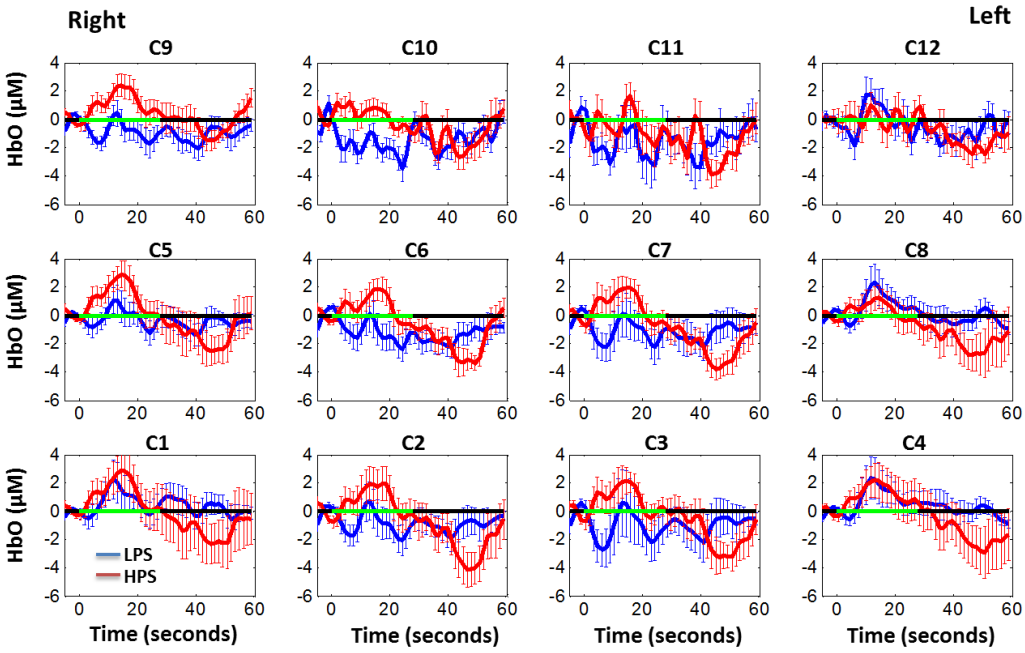

Figure 4.4 Group average of temporal profiles of ΔHbO concentration (in microMolar) across 9 subjects under left forearm thermal stimulation, for all clusters (labeled as C1, C2 …. C12). Blue and red curves represent group-averaged temporal profiles of ΔHbO in response to low pain and high pain stimulation, respectively. Error bars are standard errors. Solid green lines represent the stimulation period.

4.4.2 Deactivation of ΔHbO during Post-HPS Recovery

While channel-wise data analysis provided excellent temporal profiles for each cluster, it did not afford adequate spatial resolution to mark/map pain-evoked cortical regions with statistical significance. Thus, GLM was used to obtain topographic mapping for each of the three groups for respective thermal stimulation.

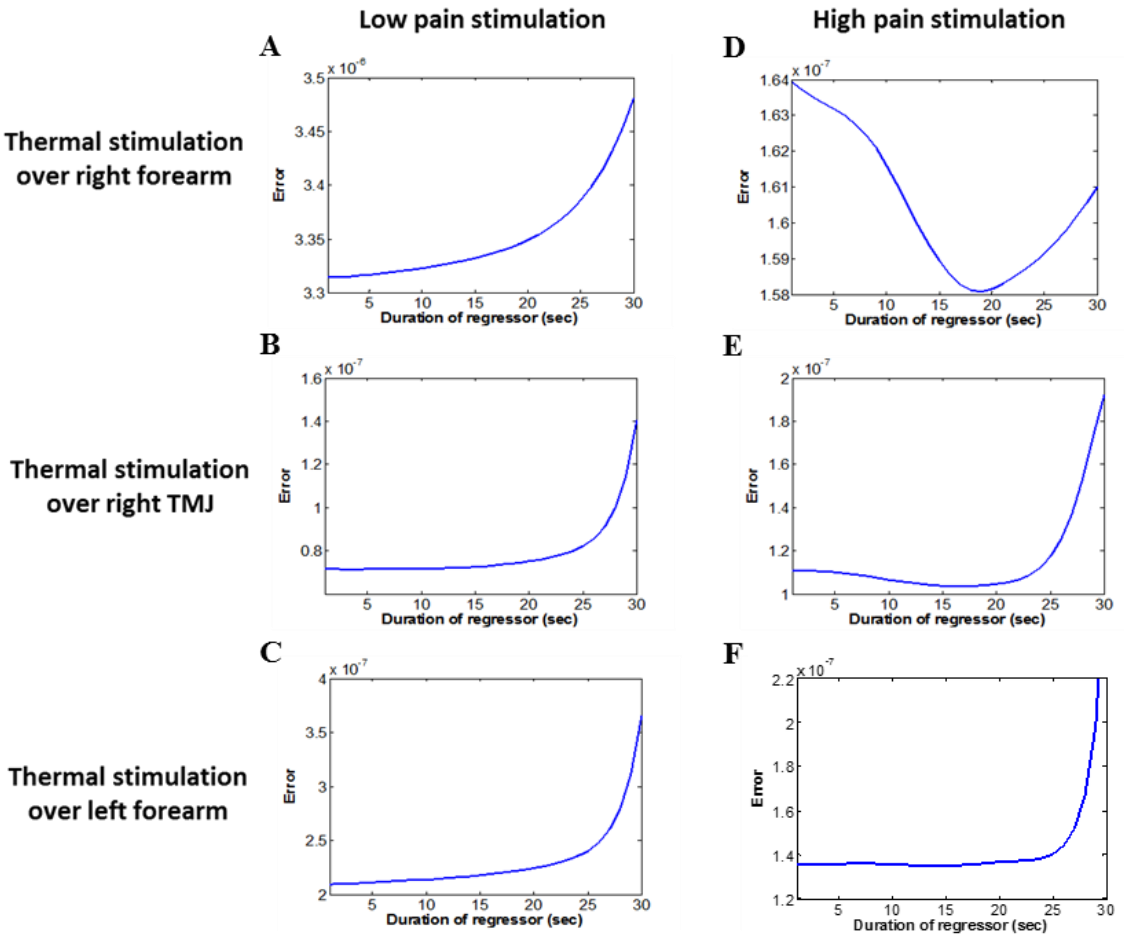

Figure 4.5 (A-C) show group-averaged norms of residuals averaged across respective subjects when the recovery predictor duration was varied (between 1 s to 30 s with an increment of 1s) to fit ΔHbO in response to LPS over the right forearm, right TMJ, and left forearm, respectively. (D-F) show group-averaged norms of residuals averaged across respective subjects when the recovery predictor duration was varied to fit ΔHbO in response to HPS over the right forearm, right TMJ, and left forearm, respectively.

Because there existed a clear, negative post-stimulation phase in ΔHbO responses under either LPS or HPS, I assumed two regressors or predictors to better fit the data by GLM. The first regressor was to reflect ΔHbO in response to the thermal stimulation, and

the second was to match the post-stimulation recovery phase. Since the duration of this recovery regressor was unknown, I varied the recovery duration and produced a duration-dependent error function (norm of residuals), averaged across all subjects for each of the three groups. Specifically, the recovery regressor duration was varied between 1s to 30s with an increment of 1s, to fit either post-LPS or post-HPS ΔHbO responses.

Figures 4.5A, 4.5B, and 4.5C show averaged norms of residuals across all subjects with LPS on the right forearm, right TMJ, and left forearm, respectively. Because the least-fitting errors appeared when the recovery regressor duration was at 1 sec in all three groups, this recovery regressor was not needed to fit ΔHbO in response to LPS. On the other hand, Figures 4.5D, 4.5E, and 4.5F illustrate averaged norms of residuals across all subjects with HPS on the right forearm, right TMJ, and left forearm, respectively. In the HPS case, the least averaged errors were obtained when the recovery predictor durations were at 19 s, 17 s, and 15 s when HPS was given over the right forearm, right TMJ, and left forearm, respectively. Thus, I employed two predictors in the GLM fitting for HPS data, one for high thermal stimulation and another for post-HPS recovery. After GLM analysis, group-averaged β-maps and corresponding *t*-maps were generated, with different reference contrasts for statistical comparisons, such as statistical differences in brain activation: (a) between LPS phase and baseline (i.e., LPS-baseline); (b) between HPS phase and baseline (HPS-baseline); and (c) between post-HPS recovery phase and baseline (recovery-baseline). These comparisons are shown in the following sub-sections.

4.4.3 Changes in HbO Induced by Noxious Thermal Stimulation Given on the Right Forearm

Figures 4.6A, 4.6B, and 4.6C show topographic images of prefrontal ΔHbO responses (β-maps) during LPS (β_{stim}-map), HPS (β_{stim}-map), and post-HPS recovery ($\beta_{post\text{-}stim}$-map) periods, respectively, when the thermal stimulations were given over the right forearm of the study group (n=16). Correspondingly, Figures 4.7A, 4.7B, and 4.7C show respective topographic *t*-maps with significant difference [$p<0.05$, False Discovery Rate (FR) corrected]. According to the β-map of Fig. 4.6A, the prefrontal regions in the left hemisphere were de-activated during LPS over the right forearm. However, none of the regions showed a significant difference from the baseline readings (see Fig. 4.7A).

On the other hand, during HPS, 20 out of total 75 channels measured from the prefrontal cortex were significantly activated with increased ΔHbO responses (Fig. 4.7B). Out of these 20 activated channels, 2 channels were located on the left pre-motor area (PMA; BA 6), 7 channels were located on the left DLPFC (BA 9 & 46), 8 channels were located on the left VLPFC (BA 44 & 45), 1 channel was located on the right FEF (BA 8), 1 channel was located on the right VLPFC, and 1 channel was located on the right DLPFC. These activated regions are all marked or shown by Fig. 4.7B. It is clear that the activation was predominant in the left prefrontal cortex during HPS of the right forearm.

Additionally, I observed significant deactivations with decreased ΔHbO, when compared to the baseline, in most of the prefrontal cortical regions during the post-HPS recovery period: 59 out of total 75 channels showed significant deactivations in the prefrontal cortical regions measured (see Fig. 4.7C). It is seen from this Figure that the

59 deactivated channels cover the PMA, FEF, DLPFC, VLPFC, and FPA on both hemispheres bilaterally.

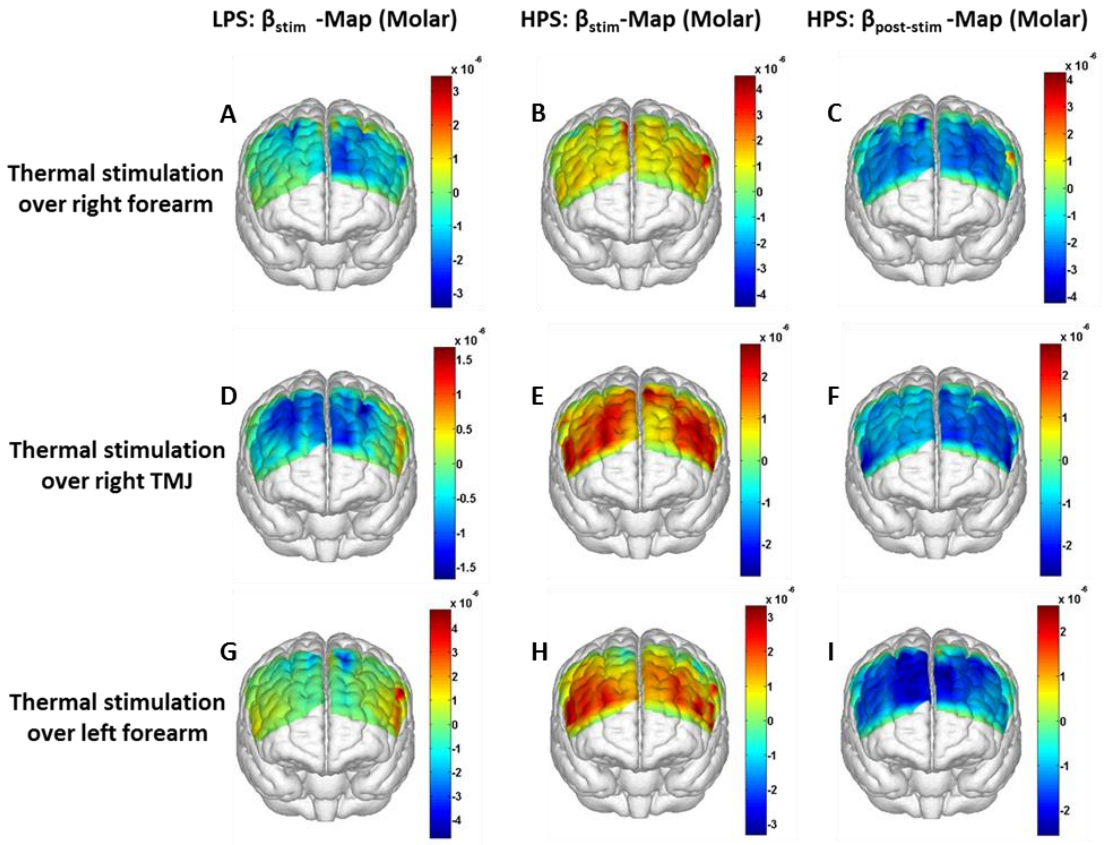

Figure 4.6 (A-C) Topographic images of group-averaged prefrontal cortical activations and/or deactivations (i.e., β-maps derived from ΔHbO) during LPS, HPS, and post-HPS recovery periods, respectively, with thermal stimulation given on the right forearm. (D-F) Topographic images of group-averaged prefrontal cortical activations and/or deactivations (β-maps) during LPS, HPS, and post-HPS periods, respectively, with thermal stimulation on the right TMJ region. (G-I) Topographic images of group-averaged frontal cortical activations and/or deactivations (β-maps) during LPS, HPS, and post-HPS periods, respectively, with thermal stimulation over the left forearm.

4.4.4 Changes in HbO Induced by Noxious Thermal Stimulation Given Over the Right TMJ

Figures 4.6D, 4.6E, and 4.6F show topographic images of prefrontal ΔHbO responses (β-maps) during LPS, HPS, and post-HPS recovery periods, respectively, when the thermal stimulations were given over the right TMJ area of the study group (n=9). Correspondingly, Figs. 4.7D, 4.7E, and 4.7F show respective *t*-maps with significant difference ($p<0.05$, FDR corrected) for those contrasts. According to the β-map and t-map shown in Figs. 4.6D and 4.7D, the bilateral prefrontal regions were deactivated during LPS, but none of the regions showed a significant difference from the baseline readings (see Fig. 4.7D). During HPS over the right TMJ, 14 out of total 75 channels measured from the prefrontal cortex were significantly activated bilaterally (see Fig. 4.7E). The 14 activated channels covered the left DLPFC and left VLPFC; on the right hemisphere side, one channel was located on the right FEF, two channels were on the right VLPFC, and four channels were on the right DLPFC.

In addition, we observed significant deactivations in most of prefrontal cortical regions during the post-HPS recovery from the thermal stimulation over the right TMJ (see Fig. 4.7F). During this recovery phase, 29 out of total 75 channels showed bilateral deactivation; they covered the left PMA, left DLPFC and left VLPFC, right PMA, right DLPFC, and right FPA.

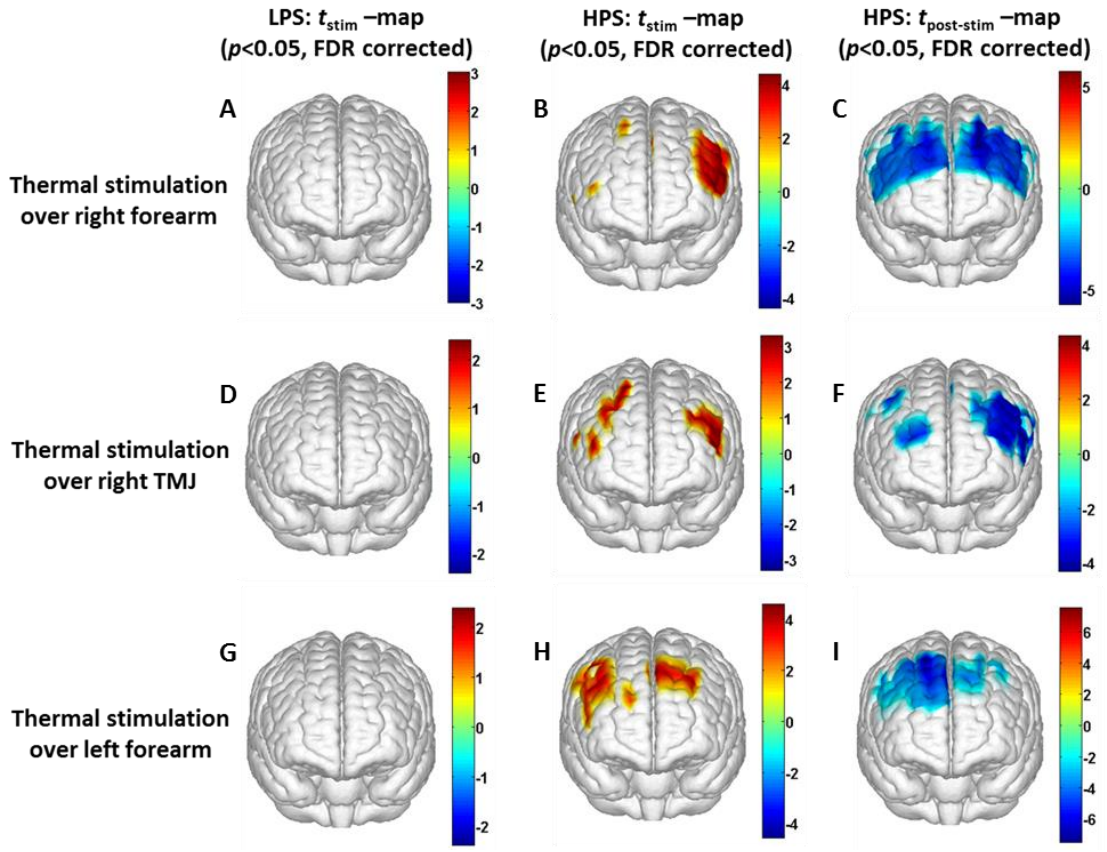

Figure 4.7 (A-C) Topographic images of statistical t-maps (p<0.05, FDR corrected) for LPS versus baseline, HPS versus baseline, and post-HPS recovery versus baseline, respectively, with thermal stimulation given on the right forearm. (D-F) Topographic images of t-maps (p<0.05, FDR corrected) for LPS versus baseline, HPS versus baseline, and post-HPS recovery versus baseline, respectively, with thermal stimulation over the right TMJ area. (G-I) Topographic images of t-maps (p<0.05, FDR corrected) for LPS versus baseline, HPS versus baseline, and post-HPS recovery versus baseline, respectively, with thermal stimulation over the left forearm.

4.4.5 Changes in HbO Induced by Noxious Thermal Stimulation over the Left Forearm

Figures 4.6G, 4.6H, and 4.6I show topographic images of prefrontal ΔHbO responses (β-maps) during LPS, HPS, and post-HPS recovery periods, respectively, when the thermal

stimulations were given over the left forearm of the study group (n=9). Correspondingly, Figs. 4.7G, 4.7H, and 4.7I show respective *t*-maps with significant difference ($p<0.05$, FDR corrected) for those contrasts. According to the β-map and t-map shown in Figs. 4.6G and 4.7G, the bilateral prefrontal regions did not show significant changes from the baseline readings. During HPS over the left forearm, 17 out of total 75 channels from the prefrontal cortex were significantly activated bilaterally but not symmetrically (see Fig. 4.7H). The 17 channels covered the left DLPFC, but covered more on the right prefrontal region: one channel on the right PMA, one channel on the right VLPFC, eight channels on right the DLPFC, and one channel on the right FPA.

Additionally, I found significant deactivations in most of the prefrontal cortical regions during the post-HPS recovery from the thermal stimulation over the left forearm. During the recovery phase, 29 out of total 75 channels showed significant deactivations bilaterally, but not symmetrically (see Fig. 4.7I). The deactivation areas covered the left FEF, left DLPFC, and left VLPFC, but there were more deactivation channels seen on the right prefrontal cortex: 5 channels were located on the right FEF, 10 channels on the right DLPFC, and 4 channels on the right FPA.

4.5 Discussion

The results presented in Section 4.4 demonstrate that HbO signals were significantly increased with respect to the baseline in the prefrontal cortex during the high-pain stimulation period, followed by a significant decrease from the baseline during the recovery period (see Figs. 4.2-4.4). On the other hand, during the low-pain stimulation period, HbO deactivation was observed in the frontal cortex, although the deactivation

was not significantly different from the baseline (also see Figs. 4.2-4.4). During HPS over the right forearm, it was found that the HbO activation was predominant in the left frontal cortex, which includes left PMA (BA 6), left DLPFC (BAs 9 & 46) and left VLPFC (BAs 44 & 45) (see Fig. 4.7B). During HPS over the right TMJ region, I noted bilateral HbO activation in the prefrontal cortex, which includes left DLPFC, left VLPFC, right FEF (BA 8), right VLPFC, and right DLPFC (see Fig. 4.7E]. During HPS over left forearm, HbO activation was also bilateral in the prefrontal cortex, which includes left DLPFC, right PMA, right VLPFC, right DLPFC, and right FPA (BA10) (see Fig. 4.7H). Overall, I noted that the temporal hemodynamic characteristics obtained from the prefrontal cortex were consistent and robust during noxious thermal stimulation over the three different body sites, while they were stimulated separately. Additionally, high-pain thermal stimulation activated a large portion of the prefrontal cortex, especially in the left DLPFC (BAs 9 & 46) and left VLPFC (BAs 44 & 45) regions.

In recent years, a variety of studies have been conducted using neuroimaging tools in order to develop a better understanding of complex neurological process and phenomena underlying pain. Several fMRI-based studies have revealed possible inter-relationships between pain and brain functions non-invasively. In particular, Kong and colleagues reported significant activations (i.e., BOLD signal increase from baseline) in several cortical and subcortical regions during high-pain thermal stimulation over the right forearm of a group of controls using fMRI. Some of the activated regions reported included, but were not limited to, the prefrontal (BAs 9, 10, 44, 46) and somatosensory cortices (i.e., S1 and S2 regions) (Kong et al., 2010). Another recent fMRI study also reported significant activations in several cortical and sub-cortical regions when a high-

pain cold stimulus was applied to the thenar surface of the right hand. The activated regions included, but were not limited to, the bilateral anterior insula, bilateral dorsal anterior cingulate cortex extending into the pre-supplementary motor area (BAs 6, 8, 24, 32), and the right lateral PFC (i.e., DLPFC and VLPFC; BAs 9, 10, 44, 45, 46, 47) (Wilcox et al., 2015). In this present study, the results also present similar activations in several prefrontal cortical areas (such as BAs 8, 9, 10, 44, 45, and 46) during high-pain thermal stimulation given at different body sites or regions [see Figs. 4.6 and 4.7]. These consistent HPS-evoked activations within the PFC might suggest its critical role in the cognitive evaluation of noxious stimuli. However, this interpretation or expectation needs to be further confirmed by correlating its hemodynamic responses with different levels of noxious stimuli (which was not available in this present study).

An fMRI-based pain study by Freund and colleagues reported that the DLPFC and caudate nucleus were significantly activated when healthy subjects made efforts to disengage from feeling pain during constant thermal stimulation (Freund et al., 2009). In addition, they suggested that caudate nucleus and PFC play a crucial role in initiation and maintenance of suppression of pain, respectively (Freund et al., 2009). Another fMRI study by a separate group also demonstrated the role of the anterolateral prefrontal cortex in expected and perceived control over pain (Wiech et al., 2006). Also, a PET-based study of pain reported the influence of DLPFC on pain perception by modulating cortico-subcortical and cortico-cortical pathways (J. Lorenz et al., 2003). All of these published studies suggest that the prefrontal cortex is one of the key elements in the “pain matrix,” and it plays a significant role in pain processing. the present results are in good agreement with, and strongly support, this overall observation and scientific findings.

Apart from ΔHbO activations in the prefrontal cortex during high-pain thermal stimulation at three different body sites or regions, I also consistently observed a significant deactivation of ΔHbO in most of the prefrontal cortical regions during the post-HPS recovery period (see Figs. 4.6 & 4.7). However, I did not detect any significant deactivation during the post-LPS recovery phase. A recent fNIRS-based pain study reported post-stimulus HbO deactivation in the frontal cortex during noxious electrical stimulation of the left thumb (Yucel et al., 2015). Furthermore, another recent fNIRS-based pain study reported a decrease in prefrontal ΔHbO, along with reduced levels of end tidal CO_2, during noxious mechanical stimulation in the low back region (Holper et al., 2014). They attributed the observed PFC deactivations to pain-related hyperventilation. Hyperventilation can result in reduced levels of end-tidal CO_2, which is a reliable estimate of partial pressure of CO_2. Since CO_2 is a known vasodilator, reduction in end tidal CO_2 should result in global vasoconstriction. In present study, I observed robust post-HPS hemodynamic deactivations in most of the frontal cortical regions. Therefore, I attributed the observed post-stimulation deactivations to vasoconstriction, caused by high pain thermal stimulation.

Several potential limitations of this present study should be noted. First, my speculation on reduction of end-tidal CO_2 during post-HPS could not be investigated because I did not use capnography to measure it while taking fNIRS measurements. Thus, simultaneous measurements of fNIRS with end-tidal CO_2 are recommended in future pain-related studies, particularly under high-pain stimulations. Second, global physiological noises that may have contaminate pain-induced HbO changes were not

removed. In future studies, such potential limitations can be minimized. One approach is to collect short separation fNIRS measurements as systemic/physiological noise predictors for adaptive noise cancellation (Tian et al., 2011). Another approach is based on global signal regression by averaging fNIRS signals over the entire measurement channels as a noise predictor to remove global systemic effects (Mesquita, Franceschini, & Boas, 2010; Murphy, Birn, Handwerker, Jones, & Bandettini, 2009).

In conclusion, this present study reported robust temporal characteristics and cortical mapping of prefrontal hemodynamics in response to noxious thermal stimulation over three body sites by using fNIRS. While the stimulations were given over the right forearm, right temporomandibular joint, and left forearm, separately, to three different groups of healthy subjects, changes of HbO in the prefrontal cortex, especially in the dorsolateral prefrontal cortex, were significantly increased ($p<0.05$, FDR corrected), with similar temporal patterns and spatial localizations. In contrast, low-pain stimulation did not result in any significant changes in HbO in the prefrontal regions in any of the three groups. The observed results were highly consistent with previous reports by other pain-related studies. In addition, I introduced and optimally selected a variable recovery regressor to account for a peculiar global trend of deactivation in the prefrontal cortex during the post-HPS period. This post-stimulation recovery regressor allowed us to identify and map deactivation regions in the prefrontal cortex, which may be attributed to global vasoconstriction due to induction of acute nocious pain. Overall, this investigation concluded that the temporal and spatial hemodynamic activities in the prefrontal cortex in response to actute thermal stimulation were consistent and robust regardless of the stimulation sites, and that multi-channel fNIRS can be used to reveal such changes

quantitatively, and may have great potential for future clinical applications. This has major clinical implications for imaging the brain without the need of the constraints and patient phobias associated with remaining in a magnet chamber.

Chapter 5

Mapping Cortical Hemodynamic Responses From Chronic Low-Back Pain Patients During Pain-Inducing Leg Raising Tasks: A Functional Near-Infrared Spectroscopy Study.

5.1 Abstract

Previous structural and functional neuroimaging studies have revealed abnormal cerebral structure and function in Chronic Low Back Pain (CLBP) patients. In this study, I utilized multichannel functional near-infrared spectroscopy (fNIRS) to investigate leg-raising-task induced pain related hemodynamic activity in the cerebral cortex among 16 elderly CLBP patients and 15 age- and gender-matched healthy controls. I compared cortical responses from controls and CLBP patients, patients before treatment versus after treatment. CLBP patients before treatment exhibited significant activations in a number of pain-related cortical regions during leg raising tasks; particularly robust widespread activations in the prefrontal cortex (BAs 9, 10, 46) were observed. Also, CLBP patients before treatment exhibited significant activations in the left frontopolar area (FPA) and left dorsolateral prefrontal cortex (DLPFC) relative to controls, during right-leg-raising (RLR) task. After treatment, CLBP patients did not show any significant differences in cortical responses relative to controls, during RLR task. Also, CLBP patients after treatment exhibited reduced prefrontal responses as compared to that of before treatment, during RLR task. My observations may implicate that abnormal prefrontal cortex function of CLBP patients was reversed to normal following treatment. Overall, the

feasibility of fNIRS for studying and mapping neural correlates of pain induced by leg-raising-tasks in CLBP patients and monitoring of treatment effects is reported.

5.2 Introduction

Chronic low back pain (CLBP) is a major public health problem throughout the world. The lifetime prevalence of non-specific low back pain is reported to be as high as 84%, and the lifetime prevalence of CLBP is about 23%, with 11-12% of the population being disabled by low back pain(van Dieen et al., 2012). Previous neuroimaging studies using structural and functional magnetic resonance imaging (MRI) have revealed the cerebral abnormalities (both structural and functional) associated with CLBP condition [for review see (Wand et al., 2011)]. Structural MRI studies have demonstrated reduced grey matter in several cortical and subcortical regions, such as the posterior parietal cortex (Buckalew, Haut, Morrow, & Weiner, 2008), the dorsolateral prefrontal cortex (DLPFC) (Apkarian, Sosa, Sonty, et al., 2004; Schmidt-Wilcke et al., 2006), the right anterior thalamus (Apkarian, Sosa, Sonty, et al., 2004), the brainstem, the somatosensory cortex (Schmidt-Wilcke et al., 2006) of CLBP patients. Functional neuroimaging studies using fMRI, and PET reported abnormal cerebral hemodynamic activities in CLBP patients (Baliki et al., 2006; Baliki et al., 2008; Derbyshire et al., 2002; Tagliazucchi et al., 2010). Also, several other neuroimaging studies have reported increased cortical responses to noxious subcutaneous stimulation of back (Flor et al., 1997), acute experimental muscle pain (Diers et al., 2007), and peripheral noxious input (Giesecke et al., 2006; Giesecke et al., 2004; Kobayashi et al., 2009) in the CLBP patients. A recent MRI-based study demonstrated that functional and structural brain abnormalities

(specifically the left DLPFC) are reversible and thus treating chronic pain can restore normal brain (Seminowicz et al., 2011). The development of assessment tools for monitoring CLBP is, therefore, crucial to improve the understanding of neural representations of CLBP and to assess potential brain plasticity resulting from physical or pharmacological treatment in CLBP condition.

In the past decade, functional near-infrared spectroscopy (fNIRS), a noninvasive, portable, easy-to-use, cost-effective, optical imaging modality, has been extensively used in the field of neuroimaging for studying brain function. This complementary brain imaging modality may have the ability to facilitate a better understanding of pain processing in the cortical regions, and monitoring therapeutic effects in CLBP patients. However, to date, none of the fNIRS-based studies have investigated (1) hemodynamic responses from whole cortical of CLBP patients during leg raising tasks, and (2) the effects of therapy on cortical hemodynamic responses from CLBP patients. In this study, fNIRS was used to acquire cortical hemodynamic signals from a group of CLBP patients and age- and gender-matched healthy (elderly) controls, to investigate both temporal and spatial patterns of cortical responses during performance of pain inducing right leg raising and left leg raising tasks. I compared and contrasted cortical hemodynamic responses during the leg raising tasks between (1) CLBP group before treatment and control group, (2) CLBP group after treatment and control group, and (3) CLBP group after treatment and CLBP group before treatment. The goal of the study was to illustrate that fNIRS can reveal cortical activities and abnormalities in patients with CLBP during pain-inducing leg raising tasks and that fNIRS could become a portable and complementary neuroimaging tool to monitor and guide treatments for patients with CLBP.

5.3 Material and Methods

5.3.1 Participants

A total of 16 elderly participants diagnosed with CLBP (six males, ten females, mean ± SD age = 73.3 ± 7.4 years) were recruited to study cortical hemodynamic responses to low-back pain induced by leg raising tasks. A total of 14 healthy participants (five males, nine females, mean ± SD age =73.4 ± 7.7 years) matched with the CLBP group on gender and age were also recruited to study cortical responses to the leg raising tasks. Also, fifteen out of 16 CLBP patients underwent therapy sessions so that I could study the aftereffects of therapeutic sessions on CLBP patients'. The protocol used was reviewed and approved by the Institutional Review Board (IRB) of the University of Texas at Arlington (UTA). The methods were carried out according to approved guidelines by the IRB of UTA. Written informed consent was obtained from each of the participants before the tasks and the fNIRS measurements were performed.

5.3.2 Instruments

In this study, a continuous-wave, multichannel, fNIRS imaging system (LABNIRS, Shimadzu Corp., Kyoto, Japan) was used, consisting of near infrared light emitting semiconductor lasers (at 780 ± 5 nm, 805 ± 5 nm, and 830 ± 5 nm) and photomultiplier tube detectors [see Fig. 5.1(A)]. An fNIRS head probe consisting of 40 source optodes and 40 detector optodes was utilized to probe the whole cerebral cortex while the participants were performing leg raising tasks [see Fig. 5.1(A)]. The fNIRS probe

configuration is shown in Fig. 5.1B. Each source optode connects to three near infrared light emitting lasers with three different wavelengths.

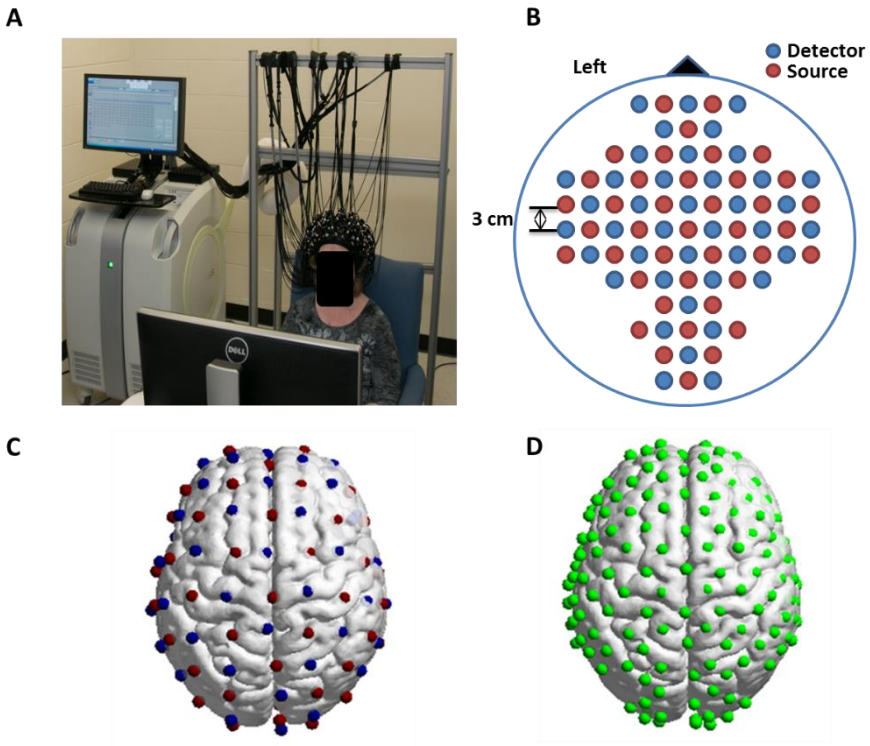

Figure 5.1 (A) Experimental setup showing LABNIRS brain imager and an optical head probe placed on a subject's head with the geometry shown in Fig. 5.1(B). (B) Probe geometry. Red circles are light sources, and blue circles are light detectors. The word "left" marks each subject's left side. (C) Co-registration of the light sources and detectors on a standard human brain template. (D) Co-registration of the channels (source-detector pairs) on a standard human brain template. Channels are marked by green circles.

5.3.3 Experimental Paradigm

The paradigm used in this study consisted of two sessions of leg raising tasks. Each participant performed right leg raising (RLR) task in the first session, followed by

left leg raising (LLR) task in the second session. These two tasks were performed to induce low-back pain in the CLBP patients'. All the participants were asked to sit in an upright position in front of a computer, and complete a session of RLR task, followed by a session of LLR task, while their brains were scanned by multichannel fNIRS. The experimental paradigm was a blocked design, with variable inter-stimulus-intervals (ISI) [see Fig. 5.2]. Within each RLR and LLR session, the paradigm consisted of a baseline (resting) period of 60 seconds, followed by six blocks of stimulus-and-resting sequences. Within each stimulus period of 14 seconds, participants performed seven cycles of raising the leg and placing it back on the ground with a frequency of 0.5 Hz (Instructed by computer). Between two stimulus blocks, there was a variable inter-stimulus interval or resting interval ranging between 10 to 15 seconds. Then, each participant was asked to rate the perception of pain after each leg raising task session, using the visual analog pain rating scale (0-10). Perception rating levels of 0, 3, 7 and 10 corresponded to no pain, low pain, high pain and extreme pain conditions, respectively. Before each fNIRS measurement session started, all the participants were trained to practice a few trials of RLR and LLR tasks. An experimenter observed the course of practice to confirm that the participants understood the paradigm correctly.

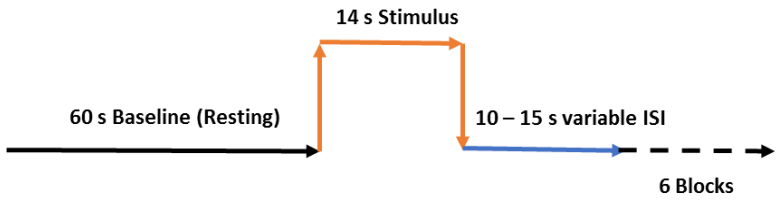

Figure 5.2 Experimental Paradigm used in this study.

5.3.4 Data Acquisition

For fNIRS data acquisition, an optical head probe, consisting of 40 sources and 40 detectors, was placed bilaterally and symmetrically over the each participant's cerebral cortex. The nearest distance between source and detector was 3 cm [see Fig. 5.1(B)]. Using this probe geometry, I were able to obtain raw optical intensities from 133 source-detector pairs (i.e., channels) when the first nearest neighbors with 3 cm separations were used. The data sampling rate was 8.13 Hz.

5.3.5 Optode co-registration

A co-registration procedure was applied based on four randomly-selected participants to estimate the cortical regions covered by the fNIRS probe (Singh et al., 2005). After placing the fNIRS probe over each subject's cerebral cortex [see Fig. 5.1(A)], positions of four reference cranial landmarks, (i.e., the nasion, left and right pre-auricular points, and vertex), light sources and detectors were measured or marked using a motion tracking system (FASTRAK, Polhemus, VT, USA). These cranial landmarks were used as reference positions while converting the real-world stereotaxic coordinates of the optodes to the Montreal Neurological Institute (MNI) coordinates which are used in a standard brain MRI atlas, based on the affine transformation (Tian et al., 2012). Using NIRS-SPM software (Ye et al., 2009). Each of the Brodmann Areas (BA) probed by the fNIRS optode array were identified. It was observed that the fNIRS probe examined almost all superficial layers of cortical Brodmann Areas. Figure 5.1C shows the registered positions (averaged over four participants) of sources' and detectors' on the standard

human brain atlas. Figure 5.1D shows the registered positions (averaged over four participants) of source-detector pairs on the standard human brain atlas.

5.3.6 Data Screening and Pre-processing

The temporal profiles of light intensities obtained after fNIRS measurements were screened and pre-processed using an LABNIRS data analysis software. First, the raw light intensity signals were visually inspected to exclude data from source-detector pairs which were associated with motion artifacts. Then, the resultant signals free from motion artifacts were low-pass filtered at a cut-off frequency of 0.2 Hz to remove systemic or physiological noise (such as cardiac and respiratory oscillations) and electronic noise, and then high-pass filtered at a cut-off frequency of 0.01 Hz to exclude any possible baseline drift. Using the modified Beer-Lambert Law (Cope et al., 1988), changes of oxygenated and deoxygenated hemoglobin concentrations (i.e., ΔHbO_2 and ΔHb, respectively) relative to the baseline were quantified.

5.3.7 Global Signal Regression

In order to remove the effect of global systemic noises on the measured hemoglobin concentration signals, a global signal regression (GSR) method was carried out on every concentration time series obtained from all the measurement sessions. I followed the GSR method described in the previous fMRI (Buckner, Andrews-Hanna, & Schacter, 2008; Murphy et al., 2009) and fNIRS (Mesquita et al., 2010) studies. Regression of the global signal is achieved by solving equation (5.1), where $s_i(t)$ is a column vector representing the time series of the ith channel's measurement (ΔHbO_2 or

∆Hb). The global signal *g(t)* is a column vector calculated by averaging the time series of hemoglobin concentrations obtained from all measurement channels over the whole cortex (See equation 5.2); the global signal calculated is used as a global noise predictor in a general linear model. N is a total number of measured channels, β_i is the regression coefficient, $z_i(t)$ is desired noise free hemoglobin concentration time series obtained after global signal regression.

$$s_i(t) = g(t)\beta_i + z_i(t) \quad (5.1)$$

$$\text{Where, } g(t) = \frac{1}{n}\sum_{i=1}^{n} s_i(t) \quad (5.2)$$

5.3.8 Data Analysis

In this study, a model-based statistical analysis tool, general linear model (GLM) was used to quantify cortical hemodynamic activities during the leg raising tasks. Over the last several years, GLM analysis has been extensively used to analyze fNIRS data to identify cortical areas which are significantly activated during a given task (Hassanpour et al., 2014; Plichta et al., 2006; Tian & Liu, 2014; Ye et al., 2009). In GLM, a hemodynamic response function (HRF) is used to serve as a model to predict the change in HbO signals due to task stimulation; GLM can be expressed by the equation (5.3):

$$z(t) = \beta f(t) + \mathcal{E}, \quad (5.3)$$

$$\text{where, } f(t) = h(t) \otimes s(t). \quad (5.4)$$

In equation (5.3), *z(t)* represents the time series of ΔHbO_2 or ΔHb at each measurement channel after global signal regression. *f(t)* is the stimulation-specific predicted response which is expected to match the temporal profiles of measured

hemodynamic signals (i.e., ΔHbO_2 or ΔHb); *h(t)* is a given hemodynamic response function (HRF); *s(t)* is the stimulation-specific boxcar function for a given task. *f(t)* is obtained by convolving *h(t)* and *s(t*) (Equation 5.4). Moreover, β is the estimated amplitude of ΔHbO_2, while ε is residual due to the mismatch between the actual data and the predicted model. By fitting the *f(t)* to the temporal profile of ΔHbO_2 obtained or measured from each channel of each participant, I would be able to obtain: (a) the estimated amplitude, β; (b) its variance, and thus (c), a statistical t-value representing the statistical significance of the brain activation at each respective channel. In this way, the amplitudes (expressed by β values in mM.cm) of cortical activations or deactivations in response to leg raising tasks were obtained by fitting the predicted stimulation response function to channel-wise, temporal profiles of ΔHbO_2 responses.

For group-level hemodynamic analyses, β values at each channel were averaged over each group of participants. Random-effect analysis was performed to generate statistically-meaningful quantities at the group level. For each of three measurement groups, it was accomplished by conducting the one-sample t-test on β values obtained from all subjects at each channel. In this way, a group-level t-statistic (expressed by t-values) was obtained to show statistically increased and/or decreased brain activations during leg raising task compared to the baseline readings. Both t-statistic values and p-values were derived from the t-tests for each channel and used to generate t-maps in topographic images.

Topographic images of cortical activations and/or deactivations were generated using EasyTopo, an optical topography toolbox (Tian et al., 2012). It overlays 2D images of ΔHbO_2 or Hb activations/deactivations over a standard human brain MRI atlas after 2D

angular interpolation of the channel-wise activation data in a spherical-coordinate system. The channel-wise β-values derived from GLM analysis and t-values from subsequent statistical comparisons were used to generate activation maps (i.e., β-maps and t-maps) induced by leg raising tasks.

5.4 Results

5.4.1 Behavioral measures

Figure 5.3A shows the comparison of pain perception ratings reported by the control group, CLBP group before treatment (CLBP-Pretreatment), and CLBP group after treatment (CLBP-Posttreatment), following RLR task session. I observed that pain perceived by CLBP-pretreatment group was significantly higher (p=0.002) as compared to that of the control group, during RLR task. Furthermore, pain perceived by CLBP-posttreatment group was also significantly higher (p=0.02) as compared to that of the control group, during RLR task. However, no significant difference (p>0.05) in pain perception between CLBP-pretreatment and CLBP-posttreatment groups was observed, during RLR task. For all statistical comparisons throughout this study, Student t-tests were used.

Figure 5.3.B shows the comparison of pain perception ratings reported by the control group, CLBP-Pretreatment group, and CLBP-Posttreatment group, following LLR task session. I observed that pain perceived by CLBP-pretreatment group was significantly higher (p = 0.0004) as compared to that of the control group, during to LLR task. Also, pain perception reported by CLBP-posttreatment group was significantly higher (p = 0.03) when compared to compared to control group, during LLR task.

However, no significant difference (p>0.05) in pain perception was observed between CLBP-pretreatment and CLBP-posttreatment groups during LLR task.

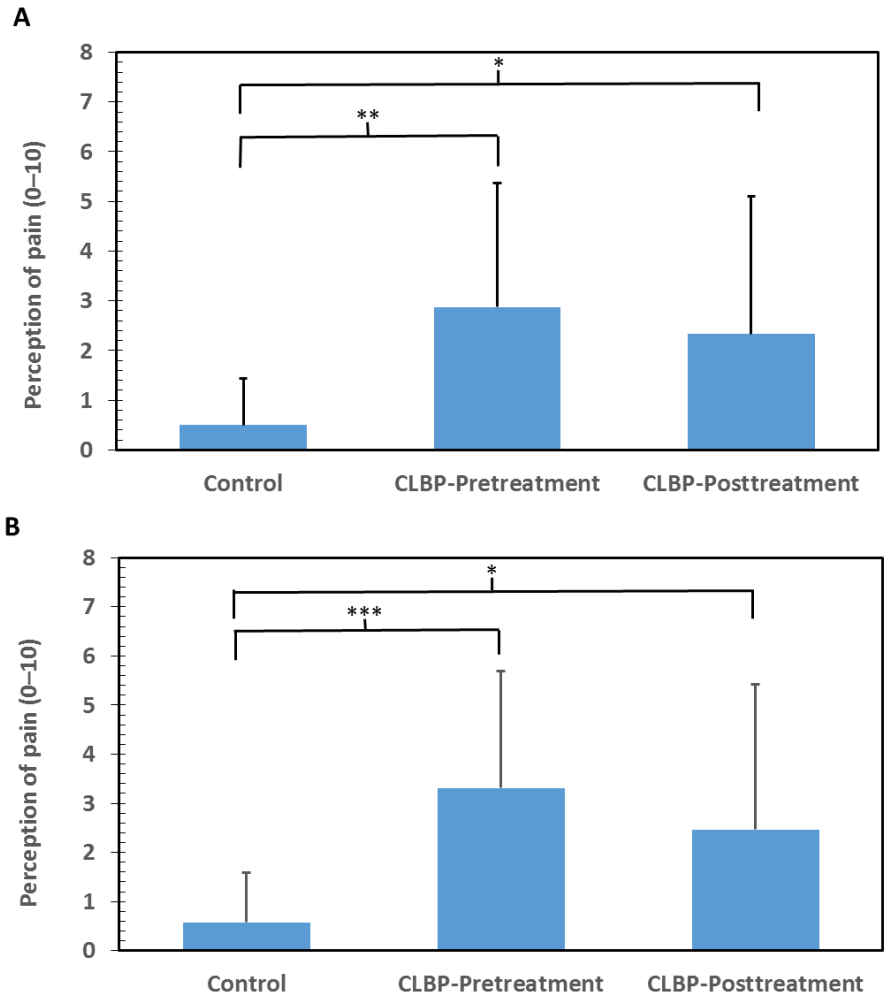

Figure 5.3 Comparison of pain perception ratings between controls and CLBP patients during (A) Right leg raising task, and (B) Left leg raising task. Pain perception rating levels of 0, 3, 7, and 10 corresponded to no pain, low pain, high pain, and extreme pain conditions, respectively. Asterisks '*' indicate significant (p<0.05), Asterisks '**' indicate significant (p<0.01), and Asterisks '***' indicate significant (p<0.001)

5.4.2 Hemodynamic Measures

5.4.2.1 HbO_2 changes induced by RLR and LLR tasks in control group

Figures 5.4A, and 5.5A show topographic images of cortical ΔHbO_2 responses (group-averaged β-maps) during RLR, and LLR task periods, respectively. Correspondingly, Figures 5.4D, and 5.5D show topographic *t*-maps [$p<0.01$, False Discovery Rate (FDR) corrected] to mark regions that have significant ΔHbO_2 changes from the baseline, induced by RLR and LLR tasks, respectively. According to the β-map of Fig. 5.4A, the primary motor and pre-motor cortices in left hemisphere was predominantly activated during RLR task period. Whereas, according to the β-map of Fig. 5.5A, the primary motor and premotor cortices in right hemisphere were activated during LLR task period.

According to the *t*-map of Fig. 5.4D, 4 out of total 133 channels measured from the cortical surface were significantly activated with increased ΔHbO_2 responses during RLR task. Out of these 4 activated channels, 1 channel was located on the left dorsolateral prefrontal cortex (DLPFC, BA 9 & 46), 2 channels were located on pre-motor and supplementary motor cortex (PSMC, BA 6), and 1 channel was located on left primary motor cortex (M1, BA 4). These activated regions are all marked or shown by Fig. 5.4D. From the *t*-map, it is clear that the activation was predominant in the left motor and pre-motor cortices of control group during RLR task.

According to the *t*-map of Fig. 5.5D, 10 out of total 133 channels measured from the cortical surface were significantly activated during LLR task. Out of these 10 activated channels, 1 channel was located on the left DLPFC, 2 channels were located on bilateral frontal eye fields (FEF, BA 8), 2 channels were located on right PSMC, 1 channel was located on left PSMC, 2 channels were located on right M1, 1 channel was located on

right primary somatosensoty cortex (S1, BAs 1, 2, & 3), and 1 channel was located on right supramarginal gyrus part of Wernicke's area (SG, BA 40) These activated regions are all marked or shown by Fig. 5.4D. From the *t*-map, it is clear that the activation was predominant in the right motor and premotor cortices of control group during LLR task.

5.4.2.2 HbO_2 changes induced by RLR and LLR tasks in CLBP group before treatment

For CLBP-pretreatment group, topographic images of cortical ΔHbO_2 responses (β-maps) during RLR, and LLR task periods, are shown in Figures 5.4B, & 5.5B, respectively. Correspondingly, Figures 5.4E and 5.5E show topographic *t*-maps ($p<0.01$, FDR corrected) to mark regions that have significant ΔHbO_2 changes from the baseline, induced by RLR and LLR tasks, respectively. According to the β-maps of Fig. 5.4B and 5.5B, several sub-regions of frontal cortex (such as frontopolar area, DLPFC, etc.) were predominantly activated during RLR, and LLR task periods, respectively.

According to the *t*-map of Fig. 5.4E, 39 out of total 133 channels measured from the cortical surface were significantly activated during RLR task. Out of these 39 activated channels, 4 channels were located on the left frontopolar area (FPA, BA 10), 3 channels were located on right FPA, 7 channels were located on the left DLPFC, 7 channels were located on the right DLPFC, 3 channels were located on left FEF, 2 channels were located on right FEF, 1 channel was located on left PSMC, 3 channels were located on right PSMC, 1 channel was located in left M1, 2 channels were located in right S1, 1 channel was located on left somatosensory association cortex (SAC, BA 7), 3 channels were located on right SAC, 1 channel was located on left SG, and 1 channel was located on left visual area 3 (V3, BA 19). These activated regions are all marked or shown by Fig.

5.4E. From the *t*-map, it is clear that the activation was predominant in the prefrontal cortex of the CLBP group during RLR task.

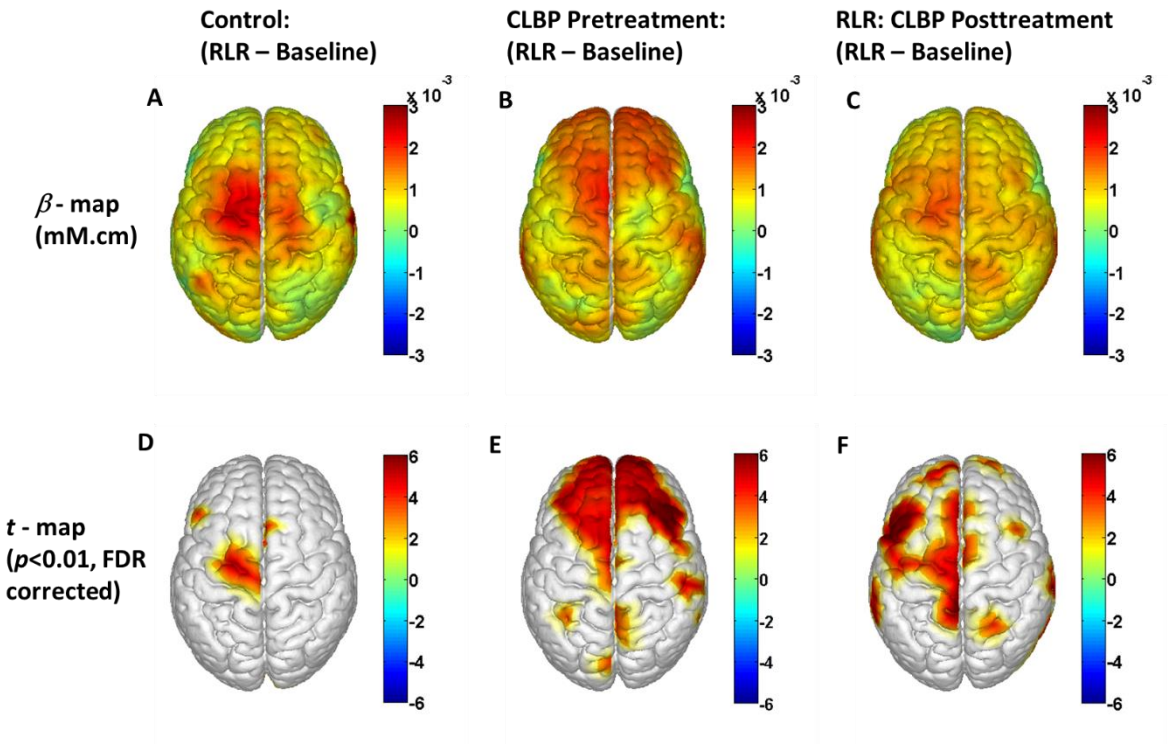

Figure 5.4. Topographic maps of the right-leg-raising (RLR) task-evoked cortical activations derived from changes in HbO2 from the control and CLBP group. A: Group-averaged cortical activation (β-map in mM.cm) evoked by RLR task in the control group; B: Group-averaged cortical activation (β-map) evoked by RLR task in CLBP group before treatment. C: Group-averaged cortical activation (β-map) evoked by RLR task in CLBP group after treatment. D: a t-statistical map (t-map) that shows significant activations and/or deactivations (one sample t-test, p<0.01; FDR corrected) on the brain template during RLR task in the control group. E: a t-map showing significant activations and/or deactivations evoked by RLR task in CLBP group before treatment. F: a t-map showing

significant activations and/or deactivations evoked by RLR task in CLBP group after treatment.

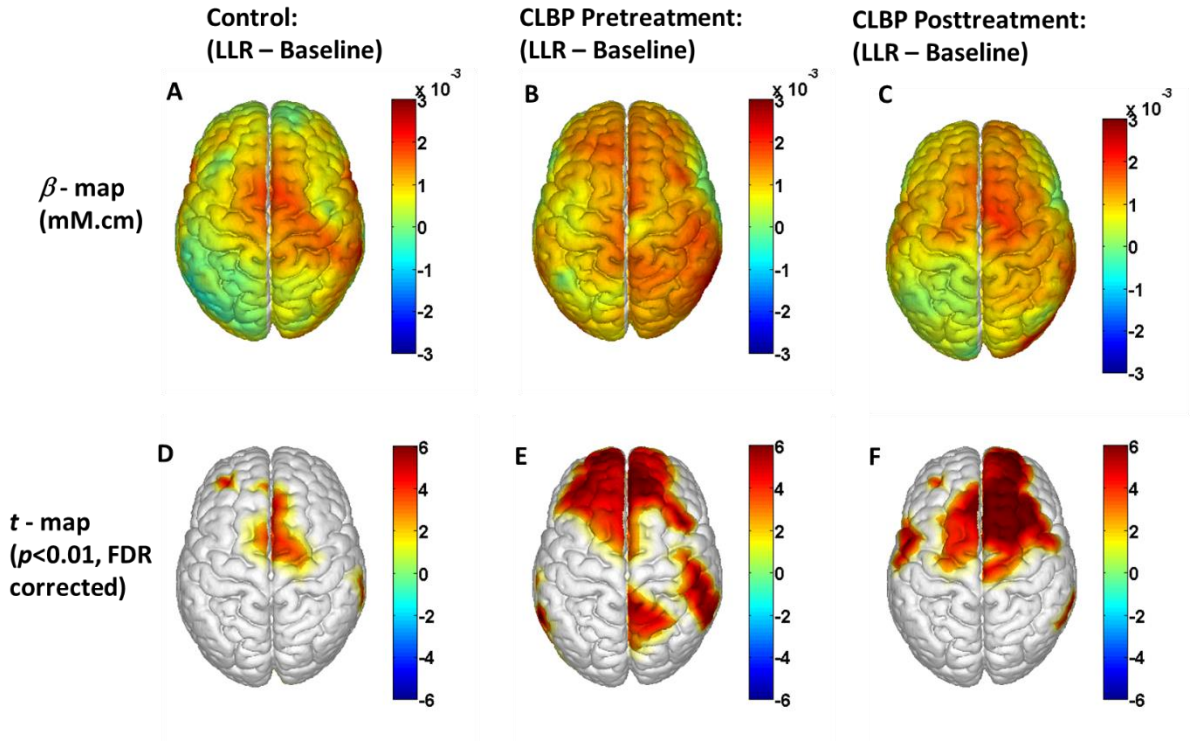

Figure 5.5. Topographic maps of the Left-leg-raising (LLR) task-evoked cortical activations derived from changes in HbO2 from the control and CLBP group. A: Group-averaged cortical activation (β-map in mM.cm) evoked by LLR task in the control group; B: Group-averaged cortical activation (β-map) evoked by LLR task in CLBP group before treatment. C: Group-averaged cortical activation (β-map) evoked by LLR task in CLBP group after treatment. D: A t-statistical map (t-map) that shows significant activations and/or deactivations (one sample t-test, $p<0.01$; FDR corrected) on the brain template during LLR task in the control group. E: A t-map showing significant activations and/or deactivations evoked by LLR task in CLBP group before treatment. F: A t-map showing

significant activations and/or deactivations evoked by LLR task in CLBP group after treatment.

According to the *t*-map of Fig. 5.5E, 46 out of total 133 channels measured from the cortical surface were significantly activated during LLR task. Out of these 46 activated channels, 4 channels were located on the left FPA, 3 channels were located on right FPA, 7 channels were located on the left DLPFC, 5 channels were located on the right DLPFC, 2 channels were located on left FEF, 2 channels were located on right FEF, 1 channel was located on left pars triangularis (PT, BA 45), 1 channel was located on left PSMC, 3 channels were located on right PSMC, 2 channels were located on right M1, 1 channels was located on left S1, 2 channels were located on right S1, 5 channels were located on right SAC, 1 channel was located on left SG, 4 channels were located on right SG, 1 channel was located on left fusiform gyrus (FG, BA 37), 1 channel was located on left Angular gyrus, part of Wernicke's area (AG, BA 39), and 1 channel was located on right AG. These activated regions are all marked or shown by Fig. 5.5E. From the *t*-map, it is clear that the activation was predominant in the prefrontal cortex of the CLBP group during LLR task as well.

5.4.2.3 HbO_2 changes induced by RLR and LLR tasks in CLBP group after treatment

For CLBP-posttreatment group, topographic images of cortical ΔHbO_2 responses (β-maps) during RLR, and LLR task periods, are shown in Figures 5.4C, & 5.5C, respectively. Correspondingly, Figures 5.4F, and 5.5F show topographic *t*-maps ($p<0.01$,

FDR corrected) to mark regions that have significant ΔHbO_2 changes from the baseline, induced by RLR and LLR tasks, respectively.

According to the *t*-map of Fig. 5.4F, 29 out of total 133 channels measured from the cortical surface were significantly activated during RLR task. Out of these 29 activated channels, 1 channel was located on the left FPA, 1 channel was located on right FPA, 4 channels were located on the left DLPFC, 1 channel was located on the right DLPFC, 2 channels were located on left FEF, 1 channel was located on right FEF, 1 channel was located on left PT, 1 channel was located on left pars opercularis (PO, BA 44), 3 channels were located on left PSMC, 2 channels were located on right PSMC, 2 channels were located on left M1, 1 channel was located on left S1, 2 channels were located on right S1, 1 channel was located on left SAC, 1 channel was located on right SAC , 1 channel was located on left superior temporal gyrus, (STG, BA 22), and 1 channel was located on right STG, 2 channels were located on left SG, and 1 channel was located on right FG. These activated regions are all marked or shown by Fig. 5.4E. From the *t*-map, it is clear that the activation was predominant in the left cortical hemisphere of CLBP group during RLR task.

According to the *t*-map of Fig. 5.5F, 28 out of total 133 channels measured from the cortical surface were significantly activated during LLR task. Out of these 28 activated channels, 2 channels were located on right FPA, 1 channel was located on the left DLPFC, 5 channels were located on the right DLPFC, 3 channels were located on left FEF, 3 channels were located on right FEF, 1 channel was located on left PO, 3 channels were located on left PSMC, 5 channels were located on right PSMC, 1 channel was located on right M1, 1 channels was located on left S1, 2 channels were located on right

SG, and 1 channel was located on right AG. These activated regions are all marked or shown by Fig. 5.5F. From the *t*-map, it is clear that the activation was predominant in the right cortical hemisphere of the CLBP group during LLR task as well.

5.4.2.4 HbO_2 changes induced by RLR and LLR tasks in CLBP-pretreatment versus control group

Figures 5.6A, and 5.7A show topographic images of cortical ΔHbO_2 differences (β-maps for CLBP-pretreatment minus control group contrast) induced by RLR, and LLR task periods, respectively. Correspondingly, Figures 5.6D, and 5.7D show topographic *t*-maps ($p<0.05$, FDR corrected) to mark regions that have significant ΔHbO_2 differences between CLBP-pretreatment and control group, induced by RLR and LLR tasks, respectively.

According to the *t*-map of Fig. 5.6D, 2 out of total 133 channels measured from the cortical surface showed significantly increased ΔHbO_2 responses in CLBP-pretreatment group as compared to that of the control group, during RLR task. Out of these 2 activated channels, 1 channel was located on left FPA, and 1 channel was located on the left DLPFC. These activated regions are all marked or shown by Fig. 5.6D. From the *t*-map, it is clear that the ΔHbO_2 responses in left prefrontal were dominant in CLBP-pretreatment group as compared to that of control group, during RLR task.

According to the *t*-map of Fig. 5.7D, 3 out of total 133 channels measured from the cortical surface showed significantly increased ΔHbO_2 responses in CLBP-pretreatment group as compared to that of control group, during LLR task. Out of these 3 activated channels, 1 channel was located on left FPA, 1 channel was located on the right DLPFC, and 1 channel was located on left AG. These activated regions are all marked or shown

by Fig. 5.7D. From the *t*-map, it is clear that the ΔHbO_2 responses in bilateral prefrontal cortex were dominant in CLBP-pretreatment group as compared to that of control group, during LLR task.

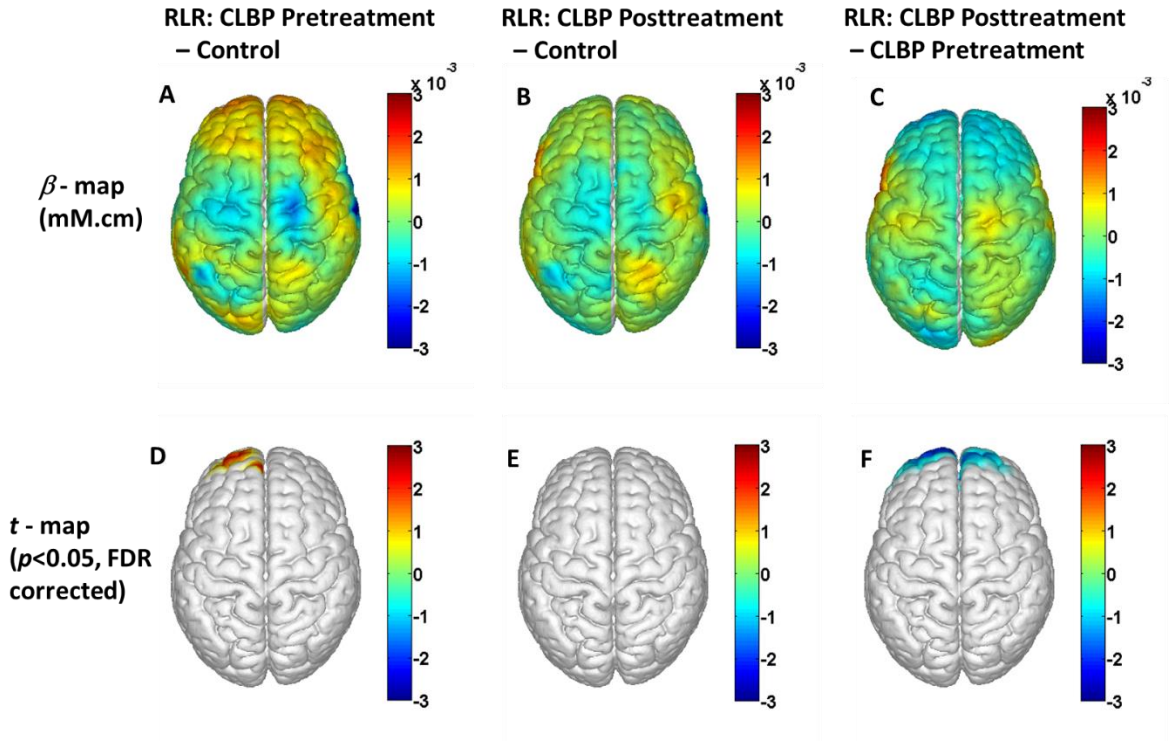

Figure 5.6. Topographic images of the cortical activations derived from HbO2, showing differences between the CLBP and control groups in response to right-leg-raising task. A: Group-averaged differences in activations or β-map (in mM.cm) between the CLBP group before treatment and control group during RLR task. B: Group-averaged differences in activations or β-map between the CLBP group after treatment and control group during RLR task. C: Group-averaged differences in activations or β-map between the CLBP group after treatment and CLBP group before treatment during RLR task. D: a t-map (p-value<0.05; FDR corrected) showing the regions of significantly different activations and deactivations between the CLBP group before treatment and control group during RLR task. E: a t-map showing the regions of significantly different activations and deactivations

between the CLBP group after treatment and control group during RLR task. F: a t-map showing the regions of significantly different activations and deactivations between the CLBP group after treatment and CLBP group before treatment during RLR task.

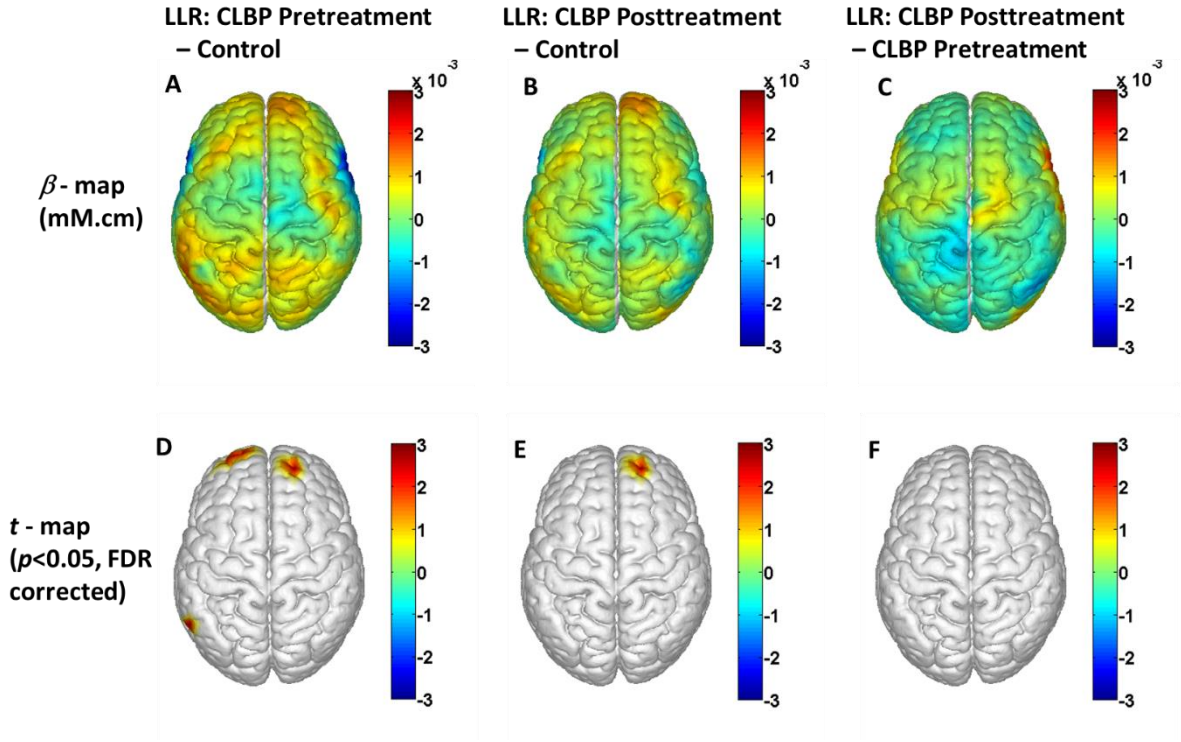

Figure 5.7. Topographic images of the cortical activations derived from HbO2, showing differences between the CLBP and control groups in response to left-leg-raising task. A: Group-averaged differences in activations or β-map (in mM.cm) between the CLBP group before treatment and control group during LLR task. B: Group-averaged differences in activations or β-map between the CLBP group after treatment and control group during LLR task. C: Group-averaged differences in activations or β-map between the CLBP group after treatment and CLBP group before treatment during LLR task. D: a t-map (p-value<0.05; FDR corrected) showing the regions of significantly different activations and deactivations between the CLBP group before treatment and control group during LLR task. E: a t-map showing the regions of significantly different activations and deactivations

between the CLBP group after treatment and control group during LLR task. F: a t-map showing the regions of significantly different activations and deactivations between the CLBP group after treatment and CLBP group before treatment during LLR task.

5.4.2.5 HbO_2 changes induced by RLR and LLR tasks in CLBP-posttreatment versus control group

Figures 5.6B, and 5.7B show topographic images of cortical ΔHbO_2 differences (β-maps for CLBP-posttreatment minus control group contrast) induced by RLR, and LLR task periods, respectively. Correspondingly, Figures 5.6E, and 5.7E show topographic *t*-maps ($p<0.05$, FDR corrected) to mark regions that have significant ΔHbO_2 differences between CLBP-posttreatment and control group, induced by RLR and LLR tasks, respectively.

According to the *t*-map of Fig. 5.6E, none of total 133 channels measured from the cortical surface showed significantly different ΔHbO_2 responses in CLBP-posttreatment group as compared to that of the control group, during RLR task. Whereas, according to the *t*-map of Fig. 5.7E, 1 out of total 133 channels measured from the cortical surface showed significantly increased ΔHbO_2 responses in CLBP-posttreatment group as compared to that of the control group, during LLR task. This activated channel was located on the right DLPFC.

5.4.2.6 HbO_2 changes induced by RLR and LLR tasks in CLBP-posttreatment versus CLBP-pretreatment group

Figures 5.6C, and 5.7C show topographic images of cortical ΔHbO_2 differences (β-maps for CLBP-posttreatment minus CLBP-pretreatment group contrast) induced by RLR, and LLR task periods, respectively. Correspondingly, Figures 5.6F, and 5.7F show topographic *t*-maps ($p<0.05$, FDR corrected) to mark regions that have significant ΔHbO_2 differences between CLBP-posttreatment and CLBP-pretreatment group, induced by RLR and LLR tasks, respectively.

According to the *t*-map of Fig. 5.6F, 6 out of total 133 channels measured from the cortical surface showed significantly decreased ΔHbO_2 responses in CLBP-posttreatment group as compared to that of CLBP-pretreatment group, during RLR task. Out of these 6 activated channels, 4 channels were located on left FPA, and 2 channels were located on the right FPA. These activated regions are all marked or shown by Fig. 5.6F. From the *t*-map, it is clear that the ΔHbO_2 responses in left frontopolar cortex were significantly reduced in CLBP-posttreatment group as compared to that of CLBP-pretreatment, during RLR task. However, according to the *t*-map of Fig. 5.7F, none out of total 133 channels measured from the cortical surface showed significantly different ΔHbO_2 responses in CLBP-posttreatment group as compared to that of CLBP-pretreatment group, during LLR task.

5.5 Discussion

The present study compared and contrasted cortical hemodynamic responses between the chronic low back pain patients and age- and gender- matched healthy controls, during the right leg raising and left leg raising tasks. Specifically, comparison of cortical ΔHbO_2 responses between (1) CLBP group before treatment and control group,

(2) CLBP group after treatment and control group, and (3) CLBP group after treatment and CLBP group before treatment, during leg raising tasks are reported. The observed behavioral and hemodynamic results and corresponding interpretations under the leg raising tasks are summarized below.

5.5.1 Experimental results/observations

Hemodynamic responses from control group: From Figure 5.4D, it is clear that left PSMC and left M1 regions were predominantly activated in the control group during RLR task as compared to that of baseline. From Figure 5.5D, it is clear that bilateral PSMC, right M1, and bilateral FEF regions were predominantly activated in the control group during LLR task as compared to that of baseline.

Hemodynamic responses from CLBP group: Relative to baseline, CLBP-pretreatment group exhibited significant hemodynamic activations in a number of cortical regions during both RLR as well as LLR tasks (see Figs. 5.4E & 5.5E). During RLR task, CLBP-pretreatment group significantly activated bilateral FPA, bilateral DLPFC, bilateral FEF, bilateral PSMC, left M1, right S1, bilateral SAC, left SG, and left V3 as compared to that of baseline (see Fig. 5.4E). Whereas during LLR task, CLBP-pretreatment group significantly activated bilateral FPA, bilateral DLPFC, bilateral FEF, left PT, bilateral PSMC, right M1, bilateral S1, right SAC, bilateral SG, left FG, and left AG as compared to that of baseline (see Fig. 5.5E).

Furthermore, CLBP group after treatment also presented significant hemodynamic activations in a number of cortical regions as compared to that of baseline, during leg raising tasks (see Figs. 5.4F & 5.5F). During RLR task, CLBP-posttreatment

group activated bilateral FPA, bilateral DLPFC, bilateral FEF, left PT, left PO, bilateral PSMC, left M1, bilateral S1, bilateral SAC, bilateral STG, left SG, and right AG (see Fig. 5.4F). Whereas, during LLR task, CLBP-posttreatment group activated right FPA, bilateral DLPFC, bilateral FEF, left PO, bilateral PSMC, right M1, left S1, right SG, and right AG (see Fig. 5.5F).

Differential hemodynamic responses between control and CLBP groups: According to pain perception results, it is clear that both RLR as well as LLR tasks induced significantly higher pain in CLBP patients as compared to that of the control group (see Figs. 5.3A & 5.3B). However, treatment did not induce any significant changes in pain perception ratings of CLBP group.

Relative to controls, CLBP-pretreatment group exhibited significantly increased ΔHbO_2 responses in left FPA and left DLPFC, during RLR task (see Fig. 5.6D). Whereas, during LLR task, CLBP-pretreatment group showed significantly increased ΔHbO_2 responses in left FPA, right DLPFC, and left AG relative to control group (see Fig. 5.7D). Overall, CLBP-pretreatment group presented predominant hemodynamic activations in the prefrontal cortex as compared to that of the control group, during both RLR as well as LLR tasks.

During RLR task, no significant difference in cortical ΔHbO_2 responses between CLBP-posttreatment group and control group was observed (see Fig. 5.6E). However, during LLR task, CLBP-posttreatment group exhibited significantly increased ΔHbO_2 responses in right DLPFC as compared to that of the control group (see Fig. 5.7E).

CLBP-posttreatment group exhibited significantly decreased ΔHbO_2 responses in bilateral FPA as compared to that of CLBP-pretreatment group during RLR task (see Fig.

5.6F). However, no significant difference in ΔHbO_2 responses between CLBP-posttreatment and CLBP-pretreatment groups during LLR task was shown (see Fig. 5.7F).

5.5.2 Interpretations

Interpretation of hemodynamic responses from control group: It is reasonable to attribute the significant activations in left PSMC and left M1 regions of the control group to inherent right leg movements associated with the RLR task. The hemodynamic activations in bilateral PSMC and right M1 regions of control group can be attributed to inherent left leg movements associated with the LLR task. Activations observed in bilateral FEF regions may be related to saccadic eye movements while following instructions on screen during leg raising task.

Interpretation of Hemodynamic responses from CLBP group: An fMRI-based pain study by Lloyd and colleagues reported significant hemodynamic activations (i.e., BOLD signal increase from baseline) in a number of cortical and sub-cortical regions corresponding to ‘pain matrix' during tactile stimulation (using constant current stimulator) of the lower back in chronic low back pain patients (Lloyd, Findlay, Roberts, & Nurmikko, 2008). Significant activated regions include, Ventrolateral prefrontal cortex (VLPFC, BA 44/45), Inferior parietal lobe (BA 40), DLPFC (BA 9/46), Superior temporal gyrus (STG), Intraparietal sulcus (BA 40/7), Supramarginal gyrus (SG, BA 40), Mid-insula, Putamen, Superior-medial frontal gyrus (BA 8/9), Secondary somatosensory cortex (S2, BA 42), Posterior insula, Anterior cingulate gyrus (BA 32), Primary somatosensory cortex (S1, BA 2) (Lloyd et al., 2008). Several other neuroimaging studies also demonstrated activations

in extensive network of pain-related brain regions with peripheral noxious input to CLBP patients (Giesecke et al., 2006; Giesecke et al., 2004; Kobayashi et al., 2009). In this present study, results also present similar activations in a number of cortical areas (such as BAs 2, 4, 6, 7, 8, 9, 10, 19, 40, 46) of CLBP patients before treatment during RLR task (see Fig. 5.4D). Also, I observed activations in a number of cortical areas (such as BAs 2, 4, 6, 8, 9, 10, 37, 39, 40, 45, 46) of CLBP patients before treatment during LLR task (see Fig. 5.5D). Also, the extent of prefrontal cortex (BAs 9, 10, & 46) activation in CLBP-posttreatment group was much less when compared to that of in CLBP-pretreatment group (compare Figs. 5.4E versus 5.4F, & Figs 5.5E versus 5.5F). Overall, CLBP-pretreatment group exhibited robust activations in several pain-related regions during both RLR and LLR tasks, especially widespread activations in bilateral FPA and DLPFC regions were noteworthy.

Interpretation of differential hemodynamic responses between control and CLBP groups: *A* recent structural and functional MRI study by Seminowicz and colleagues reported reduced cortical thickness in several cortical (left DLPFC, left S1) and subcortical regions (bilateral anterior insula/frontal operculum, left mid/posterior insula, left medial temporal lobe, and right anterior cingulate cortex) of CLBP patients before treatment relative to pain-free controls. Also, they demonstrated increased cortical thickness in left DLPFC of CLBP patients after treatment (spine surgery or facet joint injections) compared to that of CLBP patients before treatment. Furthermore, they reported increased hemodynamic activity in left DLPFC of CLBP patients before treatment as compared to that of controls while performing an attention-demanding cognitive task, but activity was reversed to normal following treatment (Seminowicz et al., 2011). Another structural MRI

study also reported increased gray matter in several cortical and subcortical structures (such as bilateral DLPFC, orbitofrontal cortex, sensorimotor cortices, etc.) of a mix of chronic pain patients following cognitive behavioral therapy (Seminowicz et al., 2013). Several other pain-related neuroimaging and repetitive transcranial magnetic stimulation studies have implicated the role of DLPFC in Placebo analgesia (Krummenacher, Candia, Folkers, Schedlowski, & Schonbachler, 2010; Wager et al., 2004), pain modulation (Brighina et al., 2004; Fierro et al., 2010; Krummenacher et al., 2010), and perceived control of pain (Pariente, White, Frackowiak, & Lewith, 2005; Wiech et al., 2006).

In the present study, results also present significantly increased ΔHbO_2 responses in prefrontal regions such as left FPA and left DLPFC of CLBP-pretreatment group relative to controls, during RLR task (see Fig. 5.6D). Although, CLBP-pretreatment group showed significantly increased ΔHbO_2 responses in right DLPFC, left FPA, and left AG relative to control group, during LLR task (see Fig. 5.7D). Also, no significant difference in cortical ΔHbO_2 responses between CLBP-posttreatment group and control group was observed, during RLR task (see Fig. 5.6E). Furthermore, during RLR task, I observed that CLBP group after treatment exhibited significantly decreased ΔHbO_2 responses in bilateral FPA relative to CLBP group before treatment (see Fig. 5.6F), although, no significant changes in pain perception ratings were reported. These observations suggest that abnormal prefrontal cortex function of CLBP patients were reversed to normal following treatment.

5.6 Conclusions

In this study, fNIRS was utilized to compare and contrast cortical hemodynamic responses from 16 elderly patients with CLBP and 15 age-/gender- matched healthy

controls while performing leg raising tasks. Leg raising tasks induced significant pain in CLBP patients before treatment as well as after the treatment as compared to that of healthy controls. Healthy controls showed hemodynamic activations in pre-motor and primary motor cortices during leg raising tasks. Whereas CLBP patients before treatment activated a number of pain-related cortical regions during both RLR as well as LLR tasks, especially widespread activations in the prefrontal cortex were noteworthy. Relative to controls, CLBP patients after treatment did not show any significant differences in cortical responses during RLR task. Furthermore, during RLR task, CLBP patients after treatment exhibited reduced prefrontal responses as compared to that of before treatment. These observations may suggest that abnormal prefrontal cortex function of CLBP patients were reversed to normal following treatment. The present study clearly demonstrates that fNIRS are a portable and complementary neuroimaging tool to study the neural correlates of pain induced by leg-raising-tasks in subjects with CLBP and monitoring treatment effects.

Chapter 6

Mapping Of ICA-Derived Resting-State Functional Networks In Chronic Low-Back Pain Patients: A Functional Near Infrared Spectroscopy Study

6.1 Abstract

Numerous structural and functional neuroimaging studies have revealed the abnormal cerebral structure and resting-state functional connectivity in Chronic Low Back Pain (CLBP) patients. In this study, we used Independent Component Analysis method on resting-state functional near-infrared spectroscopy (RS-fNIRS) signals to identify resting-state functional networks (RSFNs) among 12 elderly CLBP patients and 12 age-matched healthy controls. Furthermore, we compared and contrasted RSFNs between controls and CLBP patients. We identified four RSFNs consistently among the healthy controls and CLBP patients, namely, Default Mode Network (DMN), Somatomotor Network (SMN), Fronto-parietal Control Network (FPCN) and Visual Network (VN). The networks identified in this study were consistent with well- established RSFNs reported in previous neuroimaging studies. Also, we observed reduced DMN connectivity in CLBP patients relative to controls, specifically in right DMN constituents such as prefrontal cortex (BA 9) and Supramarginal Gyrus (BA 40) in the right cerebral hemisphere. The results suggest that the DMN connectivity in CLBP patients is compromised due to chronic pain. Overall, the feasibility of fNIRS for studying and mapping ICA-derived RSFNs in both healthy controls and CLBP patients is reported.

6.2 Introduction

Chronic low back pain is a main public health problem across the world, and it is one of the common reasons for physician visits in USA (L. G. Hart, Deyo, & Cherkin, 1995). The lifetime prevalence of non-specific low back pain (LBP) is as high as 84%, and the lifetime prevalence of CLBP is about 23%, with 11-12% of the population being disabled by LBP (van Dieen et al., 2012). Chronic back pain can significantly alter the normal brain function and lead to cognitive dysfunctions including depression, sleeping disturbances and decision-making ability (Apkarian et al., 2005; Apkarian, Sosa, Krauss, et al., 2004; Baliki et al., 2008).

In last decade, a number of neuroimaging studies using structural and functional magnetic resonance imaging (MRI) have demonstrated structural and functional brain abnormalities in CLBP patients (Kregel et al., 2015; Wand et al., 2011). Multiple structural MRI studies have revealed decreased Grey Matter in Dorsolateral Prefrontal Cortex (Apkarian, Sosa, Sonty, et al., 2004; Ivo et al., 2013; Schmidt-Wilcke et al., 2006; Seminowicz et al., 2011), Temporal Lobes (Baliki et al., 2011; Luchtmann et al., 2014; Schmidt-Wilcke et al., 2006; Seminowicz et al., 2011), Primary Somatosensory Cortex (Schmidt-Wilcke et al., 2006; Seminowicz et al., 2011), Insula (Baliki et al., 2011; Seminowicz et al., 2011), and several other cortical and sub-cortical regions of CLBP patients. Recent functional MRI studies using resting-state functional connectivity analysis, have reported disrupted Default Mode Network (DMN) connectivity in CLBP patients (Baliki et al., 2008; Kornelsen et al., 2013; Loggia et al., 2013; Tagliazucchi et al., 2010). Using fMRI, Baliki and colleagues reported reduced DMN connectivity in CLBP patients, specifically in the medial prefrontal cortex, posterior cingulate cortex and

amygdala (Baliki et al., 2008).In another resting-state fMRI study, Tagliazucchi and colleagues reported that abnormal connectivity in DMN structures such as angular gyrus, bilateral insular cortex, and orbital part of the middle frontal gyrus (Tagliazucchi et al., 2010). A recent MRI-based study demonstrated that both the functional and structural brain abnormalities (specifically the left DLPFC) in the chronic pain patients are reversible and thus treating chronic pain can restore normal brain (Seminowicz et al., 2011). Therefore, the development of assessment tools for monitoring CLBP is crucial to improving the understanding of neural correlates of CLBP and to monitor brain's functional changes resulting from physical or pharmacological treatment in CLBP condition.

In the past decade, functional near-infrared spectroscopy, a noninvasive, optical imaging modality, has been extensively used in the field of neuroimaging for studying brain function. It is portable, easy-to-use, and cost-effective as compared other functional imaging modalities such as fMRI and Positron Emission Tomography (PET). This complementary brain imaging modality may have the ability to identify abnormalities in CLBP patients so that it could facilitate better understanding of pain processing in the cortical regions, and monitoring therapeutic effects in CLBP patients. Resent Resting-state fNIRS (RS-fNIRS) studies were able to identify resting state functional networks such as Sensorimotor Network and Visual Network using independent component analysis (Zhang, Duan, et al., 2011; Zhang, Zhang, et al., 2011; Zhang et al., 2010); ICA is a data-driven analysis method that can isolate independent brain networks that have temporally correlated hemodynamic activity. However, to date, none of the fNIRS-based studies have identified whole-cortex resting state functional networks in both healthy as

well as in CLBP patients. In this study, fNIRS was used to identify whole-cortex RSFNs in both Healthy and CLBP participants based on independent component analysis method. Furthermore, we compared and contrasted the ICA-derived RSFNs between healthy and CLBP participants. The goal of the study was to illustrate that (1) fNIRS can reveal RSFNs in both healthy and CLBP participants and (2) to detect if there exist any abnormalities in RSFNs (Objective biomarkers) of CLBP patients so that fNIRS could be used as portable and complementary neuroimaging tool to monitor and guide treatments for patients with CLBP.

6.3 Material and Methods

6.3.1 Participants

A total of 12 elderly participants diagnosed with CLBP (four males, eight females, mean ± SD age = 72.9 ± 8.8 years) and a total of 12 healthy participants (five males, seven females, mean ± SD age =73.3 ± 8.2 years) age-matched with CLBP participants were recruited to study ICA-derived resting state cortical networks using fNIRS. The experimental methods in this study were carried out according to approved guidelines by the Institutional Review Board of the University of Texas at Arlington. Written informed consent was obtained from each participant before the fNIRS measurements were performed.

6.3.2 Instruments

In this study, we used a continuous wave, multichannel, fNIRS system (LABNIRS, Shimadzu Corp., Kyoto, Japan) which consists of near infrared light emitting semiconductor lasers (at 780 ± 5 nm, 805 ± 5 nm, and 830 ± 5 nm wavelengths) and

photomultiplier tube detectors, to record cortical hemodynamic activity in CLBP and healthy participants [see Fig. 6.1(A)]. I used an fNIRS head probe which could hold 40 source optodes and 40 detector optodes to probe the whole cerebral cortex while the participants were following experimental paradigm [see Fig. 6.1(B)]. Each source optode connects to three near infrared light emitting lasers with three different wavelengths. The fNIRS probe geometry is shown in Figure 6.1C.

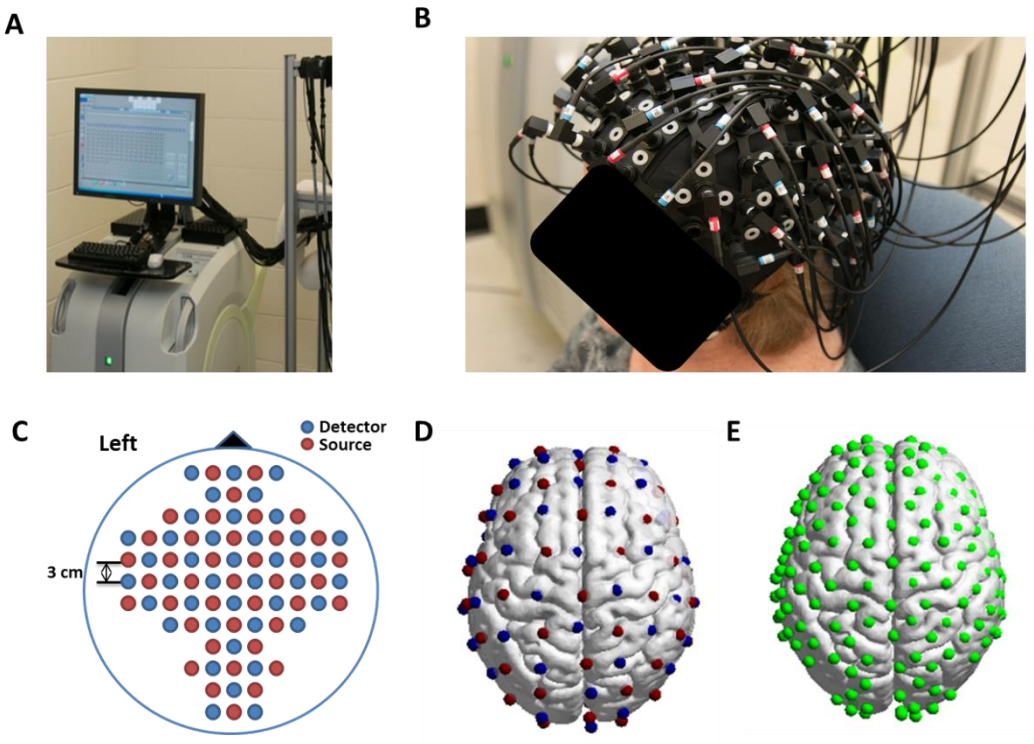

Figure 6.1 (A) LABNIRS, Multichannel fNIRS system. (B) Placement of optical head probe on a subject's head with the geometry shown in Fig. 6.1(C). (C) Probe geometry: Red circles represent light sources, and blue circles represent light detectors. The word "left" marks each subject's left side. (D) Co-registration of the light sources and detectors on a standard human brain template. (E) Co-registration of the channels (source-detector pairs) on a standard human brain template. Channels are marked by green circles.

6.3.3 Experimental Paradigm

All the participants were asked to sit comfortably in a chair and rest for 8 minutes with eyes closed while scanned by multichannel fNIRS. The subjects were instructed to relax their mind and avoid head movements during the resting-state fNIRS session. An experimenter observed the fNIRS sessions to confirm that the participants followed the paradigm correctly.

6.3.4 Data Acquisition

For fNIRS data acquisition, an optical head probe holding 40 sources and 40 detectors was placed bilaterally and symmetrically over each participant's cerebral cortex [see Fig. 6.1(B)]. The nearest distance between source and detector was set as 3 cm. Using this probe geometry, I obtained raw optical intensities from 133 source-detector pairs (i.e., channels) when only the first nearest neighbors with 3 cm separations were used. The fNIRS data were acquired at a sampling rate of 8.13 Hz.

6.3.5 Optode co-registration

A co-registration procedure was followed using 3D digitizer measurements obtained from four randomly-selected participants to estimate the cortical regions probed by the fNIRS head-probe (Singh et al., 2005). After placing the fNIRS probe over each subject's cerebral cortex [see Fig. 6.1(B)], positions of four reference cranial landmarks, (i.e., the nasion, left and right pre-auricular points, and vertex), light sources and detectors were measured using a motion tracking system (FASTRAK, Polhemus, VT, USA). The positions of cranial landmarks served as reference positions while converting the real-world stereotaxic coordinates of the source and detector optodes to the Montreal

Neurological Institute (MNI) coordinates which are used in a standard brain MRI atlas, based on the affine transformation (Tian et al., 2012). Then, each of the Brodmann Areas (BA) probed by the fNIRS optode array were identified using NIRS-SPM software package (Ye et al., 2009). The fNIRS head-probe used in this study examined almost all superficial layers of cortical Brodmann Areas (BA). The co-registered positions (averaged over four participants) of optodes and source-detector pairs (calculated as the midpoint between a source and a detector) on the standard human brain atlas are shown in Figure 6.1D and Figure 6.1E, respectively.

6.3.6 Data Screening and Pre-processing

The temporal profiles of light intensities obtained after fNIRS measurements were screened and pre-processed using an LABNIRS data analysis software. First, the raw light intensity signals were visually inspected to exclude data from source-detector pairs which with motion artifacts. Then, the resultant signals free from motion artifacts were low-pass filtered at a cut-off frequency of 0.1 Hz to remove systemic or physiological noise (such as cardiac and respiratory oscillations) and electronic noise, and then high-pass filtered at a cut-off frequency of 0.01 Hz to exclude any possible baseline drift. Using the modified Beer-Lambert Law (Cope et al., 1988), changes of oxygenated and deoxygenated hemoglobin concentrations (i.e., ΔHbO_2 and ΔHb, respectively) relative to the baseline were quantified.

6.3.7 Global Signal Regression

A global signal regression (GSR) method was applied to remove the effect of global systemic noises on the measured hemoglobin concentration signals. I followed the

GSR method described in the previous fMRI (Buckner et al., 2008; Murphy et al., 2009) and fNIRS (Mesquita et al., 2010) studies. Regression of the global signal can be achieved by solving equation (6.1), where $s_i(t)$ is a time series of the i^{th} channel's hemoglobin measurement (ΔHbO_2 or ΔHb). The global signal $g(t)$ is a column vector calculated by averaging the time series of hemoglobin concentrations obtained from all measurement channels over the whole cortex of each participant (See equation 6.2); the global signal calculated is used as a global noise predictor in a general linear model. N is a total number of measured channels, β_i is the regression coefficient, $x_i(t)$ is desired noise free hemoglobin concentration time series obtained after global signal regression.

$$s_i(t) = g(t)\beta_i + x_i(t) \quad (6.1)$$

$$g(t) = \frac{1}{n}\sum_{i=1}^{n} s_i(t) \quad (6.2)$$

6.3.8 Independent component analysis theory

Independent component analysis is a data-driven statistical technique used to estimate the hidden factors (sources) from a set of measurements such that the sources are maximally independent. It can be can explained by a classic "cocktail party" problem. For example, assume that several microphones in a cocktail party simultaneously record voices from multiple people (sources). The recorded signals are the mixture of several different voices. Given such mixed recordings, ICA can recover (estimate) the original voices under the assumption that the voices from different people are independent of each other. ICA assumes that the source signals are statistically independent and non-gaussian, with an unknown, but linear mixing process.

In the case of fNIRS, signals $x(t)=[x_1(t), x_2(t), x_3(t), \ldots\ldots x_N(t)]^T$ recorded from *N* number of channels with *t* time samples can regarded as mixture of voices recorded by *N* microphones, and the *N* 'true' sources $s(t)=[s_1(t), s_2(t), s_3(t), \ldots\ldots s_N(t)]^T$ can be regarded as the voice signals from *N* number of people. The fNIRS measurements x(*t*) can thus be expressed as matrix multiplication of mixing matrix *A* and 'true' sources *s(t)* (Equation 6.3). The goal of ICA is to estimate the unmixing matrix *W* such that the estimate of 'true' source signals $\hat{s}(t)$ can be obtained by matrix multiplication of unmixing matrix *W* and recorded fNIRS signals *x(t)* (Equation 6.4). An estimate of mixing matrix $\hat{A}$ can be obtained by calculating pseudoinverse of unmixing matrix *W* (Equation 6.5). The estimated mixing matrix $\hat{A}$ represents spatially independent components (Includes RSFNs and noise components) in x(*t*), and $\hat{s}(t)$ represents temporal activities associated with those spatial components.

$$x(t) = As(t) \tag{6.3}$$

$$\hat{s}(t) = Wx(t) \tag{6.4}$$

$$\hat{A} = W^{-} \tag{6.5}$$

6.3.9 ICA-derived Resting state functional networks

In this study, I utilized Temporal-ICA group analysis method which has been widely used in previous fMRI (Calhoun, Adali, Pearlson, & Pekar, 2001; Calhoun, Liu, & Adali, 2009; Guo & Pagnoni, 2008; Schmithorst & Holland, 2004), RS-fNIRS (Zhang, Duan, et al., 2011; Zhang, Zhang, et al., 2011; Zhang et al., 2010) and task-based fNIRS studies (Markham, White, Zeff, & Culver, 2009; Medvedev, Kainerstorfer, Borisov, Barbour, &

VanMeter, 2008; Morren et al., 2004). I chose temporal ICA method since it is more suitable for analyzing fNIRS data which has a small number of measurement channels (e.g., 133 channels) but relatively high temporal sampling rate (8 minutes recording with 8.13 Hz sampling rate). The advantage of Temporal ICA approach is that the independent components obtained after performing single ICA on the temporally concatenated data, can be further divided into subject-specific parts. Thus the comparison of group differences is straightforward.

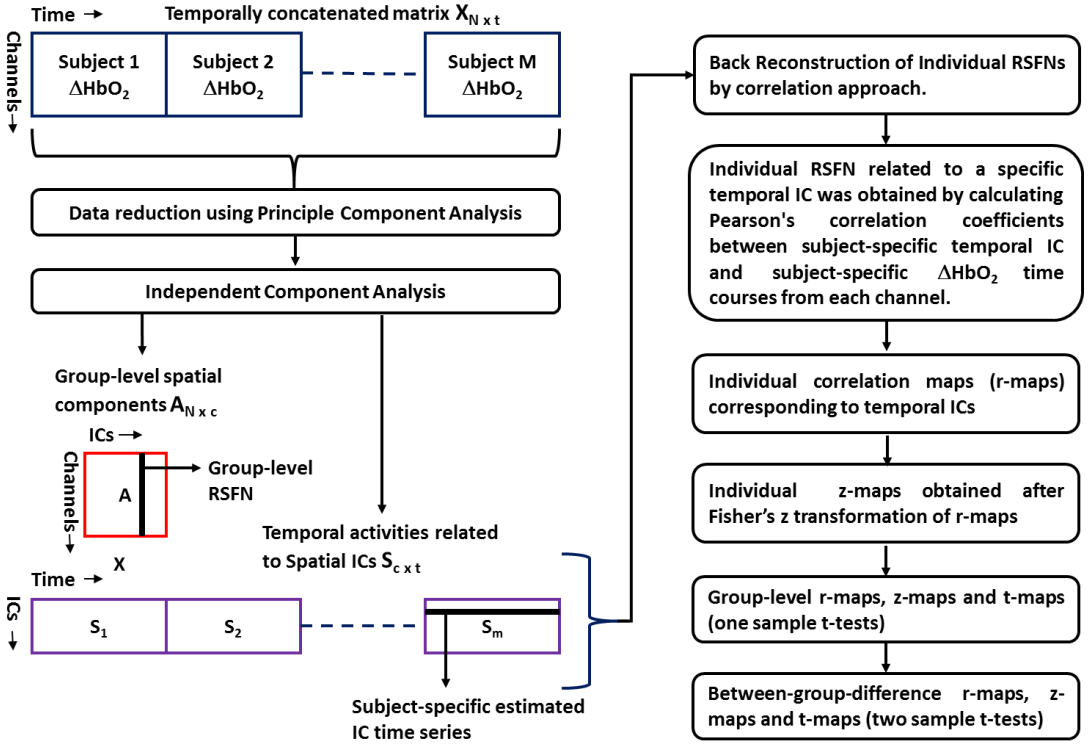

Figure 6.2: Schematic representation of temporal ICA method used in this study

For ICA decomposition of fNIRS data, I used an MATLAB-based software package with a Graphical user interface called FastICA v2.5 (http://research.ics.aalto.fi/ica/fastica/). FastICA implements a fixed-point algorithm for ICA decomposition (Hyvarinen, 1999). In this study, group-level temporal ICA

decomposition was performed on ΔHbO_2 signals with following steps (See Fig. 6.2 for Schematic representation of group-level temporal ICA method implemented in this study).

Step 1: Initially, resting-state ΔHbO_2 signals obtained from both CLBP and healthy participants' were temporally concatenated to form group matrix $X_{N\,x\,t}$, where N is number of measurement channels and t is number of time points after temporal concatenation.

Step 2: Principle component analysis (PCA) was performed to reduce the dimentionality of group matrix to $X_{c\,x\,t}$, where c is number of retained components after PCA reduction. By selecting first 40 principle components (PCs), I could retain 83% of data variance. I used a PCA algorithm which is available in FastICA v2.5 toolbox.

Step3: ICA was performed on PCA-reduced group matrix $X_{c\,x\,t}$ to generate group-level estimated spatial component matrix $A_{N\,x\,c}$, and estimated temporal IC matrix $S_{c\,x\,t}$, where c is number of ICs. The FastICA algorithm parameters were set as, approach = "deflation", Number of ICs = 40, nonlinearity = "pow3", Stabilization = "on", epsilon (stopping criterion) = 0.0001, Maximum number of iterations = 1000, Initial state = "random".

Step 4: Back reconstruction of individual resting-state functional networks: The group-level temporal IC matrix $S_{c\,x\,t}$ was partitioned into subject-specific matrices $S1_{c\,x\,t1}$, $S2_{c\,x\,t2}$, ….. $Sm_{c\,x\,tn}$, where t1, t2 ….tn are a subject-specific number of time samples, and m is number of participants. Then, I obtained subject-specific spatial components related to i^{th} temporal IC by calculating Pearson's correlation coefficients between subject-specific c^{th} temporal IC and subject-specific ΔHbO_2 time courses from each channel. Such spatial components were considered as subject-specific correlation vector (expressed by r-map) corresponding to c^{th} temporal IC. Similarly, I obtained 40 subject-

specific correlation vectors from each of control and CLBP participants. Correlation coefficients in spatial component matrix represent contribution strength of temporal ICs in each measured channel (ΔHbO_2 time series). By visual inspection, some of spatial components were considered to be RSFNs based on the criteria that the activity should be bilateral and symmetrical in cerebral cortex.

Step 5: The individual correlation vectors (r-maps) from both control as well as CLPB participants were normalized using Fisher's z-transformation (equation 6.6). Similarly, I obtained individual z-maps for all the participants.

$$z = \frac{1}{2}\, ln\left(\frac{1+r}{1-r}\right) \quad (6.6)$$

Step 6: Radom effects analysis: For group-level RSFNs, r-maps, and z-maps were averaged over each group of participants. Random-effect analysis was performed on z-maps to generate statistically meaningful RSFNs at the group level. For each of two measurement groups, it was accomplished by conducting the two-tailed one-sample t-test on z values obtained from all subjects at each channel. In this way, a group-level t-statistic (expressed by t-values) was obtained to show significantly correlated brain regions related to specific network IC time-series. Both t-statistic values and p-values were derived from the t-tests for each channel and used to generate t-maps in topographic images. For between-group differences, two-sample t-tests were used on z-maps.

Topographic images of RSFNs were generated using EasyTopo, an optical topography toolbox (Tian et al., 2012). It is used to overlay 2D images of correlation coefficients over a standard human brain MRI atlas after 2D angular interpolation of the channel-wise correlation coefficients in a spherical-coordinate system. The channel-wise

r-values, z-values, and t-values from subsequent statistical comparisons were used to generate topographic r-maps, z-maps, and t-maps.

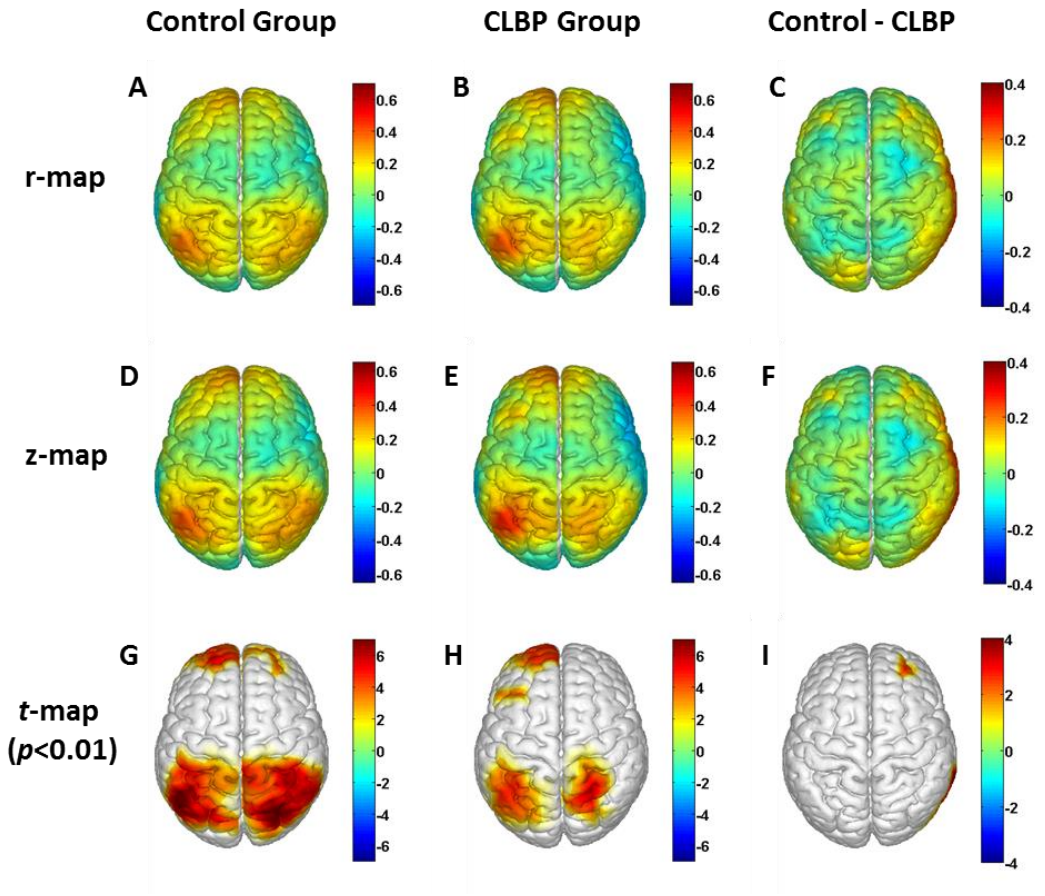

Figure 6.3: (A), (D), and (G): Topographic images of ICA-derived group-averaged r-map, z-map (Fisher's z-transformation of r-map), and t-map (two-tailed, one sample t-test, p<0.01), corresponding to Default Mode Network (DMN) component in control group, respectively. (B), (E), and (H): Topographic images of ICA-derived group-averaged r-map, z-map, and t-map (two-tailed, one sample t-test, p<0.01), corresponding to DMN component in CLBP group, respectively. (C), (F), and (I): Topographic images of between-group differences (Control *minus* CLBP contrast) r-map, z-map, and t-map (two-tailed, two sample t-test, p<0.01), corresponding to DMN component, respectively.

6.4 Results

In this study, by visual inspection of group-level ICA-derived spatial component maps , I identified four meaningful resting-state functional networks in control as well as in CLBP groups. The group-level spatial component maps corresponding to each temporal network component are described below.

6.4.1 ICA-derived resting-state functional networks in control group

6.4.1.1 Default Mode Network in control group

The group-averaged spatial component maps corresponding to Default Mode Network (DMN) temporal component in the control group are shown in Figure 6.3. Figure 6.3A shows a topographic image of group-averaged r-map corresponding to DMN network component in the control group. Figure 6.3D shows a topographic image of group-averaged z-map (Fisher's z-transformation of r-maps) corresponding to DMN network component in the control group. Correspondingly, Figure 6.3G shows topographic t-map ($p<0.01$) to mark regions that have significant correlation between DMN temporal component and ΔHbO_2 time series from each channel.

According to the *t*-map of Figure 6.3G, 41 out of total 133 channels measured from the cortical surface were significantly correlated to temporal component of DMN network. Out of these 41 significantly correlated channels, 5 channels were located on the left Frontopolar Area (FPA, BA 10), 2 channels were located on right FPA, 2 channels were located on left Dorsolateral Prefrontal Cortex (DLPFC, BA 9 & 46), 1 channel was located on right DLPFC, 1 channel was located on left Primary Somatosensory Cortex (S1, BAs 1, 2 & 3), 1 channel was located on right S1, 1 channel was located on left Primary Motor

Cortex (M1, BA 4), 2 channels was located on right M1, 2 channels were located on left Supramarginal Gyrus part of Wernicke's area (SG, BA 40), 4 channels were located on right SG, 5 channels were located on left Somatosensory Association Cortex (SAC, BA 7), 8 channels were located on right SAC, 2 channels were located on left Angular Gyrus part of Wernicke's area (AG, BA 39), 2 channels were located on right AG, 1 channel was located on left Visual Association Cortex 3 (V3, BA 19), and 2 channels were located on right V3

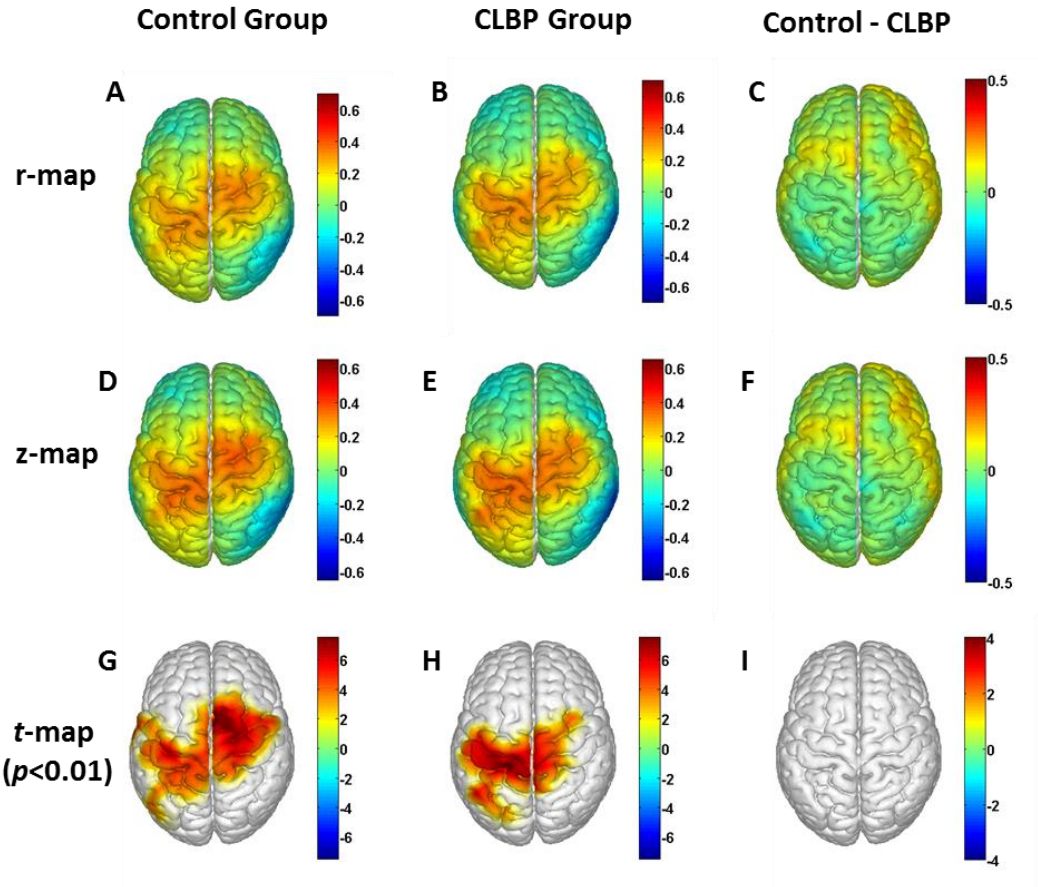

Figure 6.4: (A), (D), and (G): Topographic images of ICA-derived group-averaged r-map, z-map (Fisher's z-transformation of r-map), and t-map (two-tailed, one sample t-test, p<0.01), corresponding to Somatomotor Network (SMN) component in the control group, respectively. (B), (E), and (H): Topographic images of ICA-derived group-averaged r-

map, z-map, and t-map (two-tailed, one sample t-test, $p<0.01$), corresponding to SMN component in CLBP group, respectively. (C), (F), and (I): Topographic images of between-group differences (Control *minus* CLBP contrast) r-map, z-map, and t-map (two-tailed, two sample t-test, $p<0.01$), corresponding to SMN component, respectively.

6.4.1.2 Somatomotor Network in control group

The group-averaged spatial component maps corresponding to Somatomotor Network (SMN) temporal component in the control group are shown in Figure 6.4. Figures 6.4A and 6.4D shows topographic images of group-averaged r-map and z-map corresponding to SMN network component in the control group. Correspondingly, Figure 6.4G shows topographic t-map ($p<0.01$) to mark regions that have significant correlation between SMN temporal component and ΔHbO_2 time series from each channel.

According to the *t*-map of Figure 6.4G, 29 out of total 133 channels measured from the cortical surface were significantly correlated to temporal component of DMN network. Out of these 29 significantly correlated channels, 4 channels were located on left Pre-Motor and Supplementary Motor Cortex (PSMC, BA 6), 6 channels were located on right PSMC, 4 channels were located on left M1, 5 channels were located on right M1, 2 channels were located on left S1, 3 channels were located on left SAC, 1 channel was located on right SAC, 1 channel was located on left AG, 1 channel was located on left SG, 1 channel was located on left Subcentral Area (SA, BA 43), and 1 channel was located in right Frontal Eye Fields (FEF, BA 8).

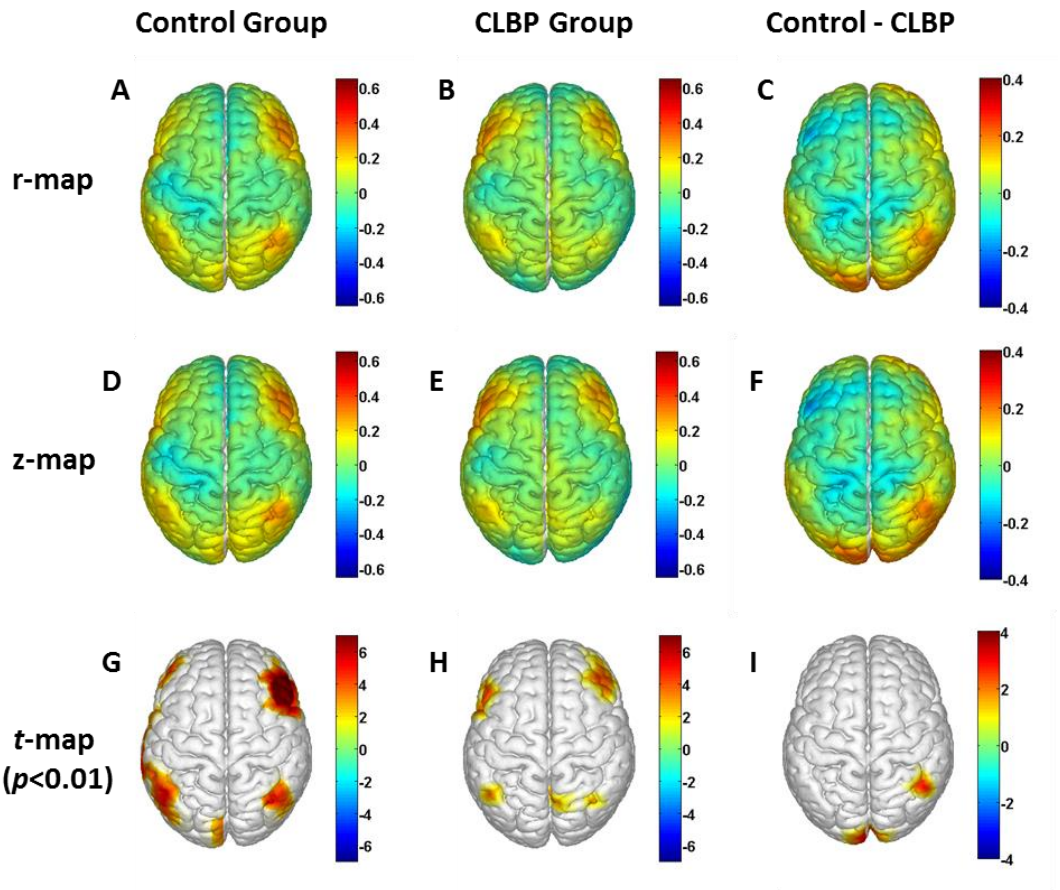

Figure 6.5: (A), (D), and (G): Topographic images of ICA-derived group-averaged r-map, z-map (Fisher's z-transformation of r-map), and t-map (two-tailed, one sample t-test, p<0.01), corresponding to Fronto-parietal Control Network (FPCN) component in control group, respectively. (B), (E), and (H): Topographic images of ICA-derived group-averaged r-map, z-map, and t-map (two-tailed, one sample t-test, p<0.01), corresponding to FPCN component in CLBP group, respectively. (C), (F), and (I): Topographic images of between-group differences (Control *minus* CLBP contrast) r-map, z-map, and t-map (two-tailed, two sample t-test, p<0.01), corresponding to FPCN component, respectively.

6.4.1.3 Fronto-parietal Control Network in control group

The group-averaged spatial component maps corresponding to Fronto-parietal Control Network (FPCN) temporal component in the control group are shown in Figure

6.5. Figures 6.5A and 6.5D shows topographic images of group-averaged r-map and z-map corresponding to FPCN network component in the control group, respectively. Correspondingly, Figure 6.5G shows topographic t-map ($p<0.01$) to mark regions that have significant correlation between FPCN temporal component and ΔHbO_2 time series from each channel.

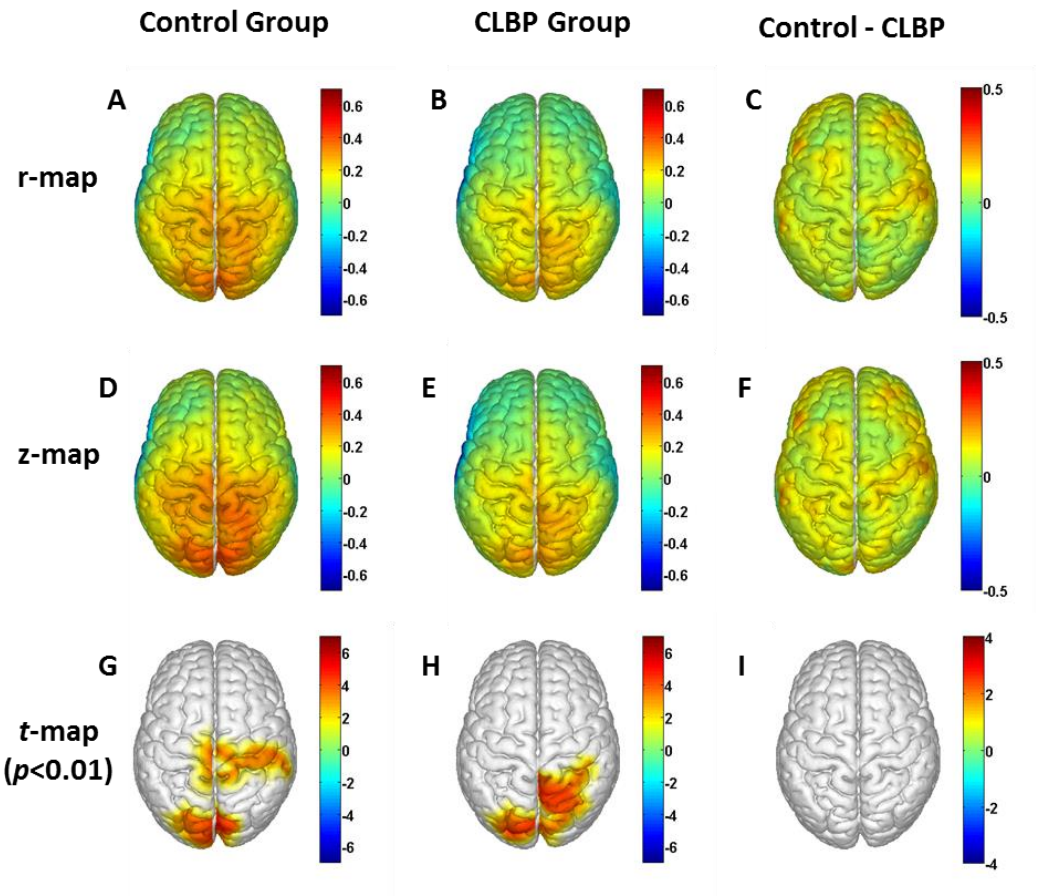

Figure 6.6: (A), (D), and (G): Topographic images of ICA-derived group-averaged r-map, z-map (Fisher's z-transformation of r-map), and t-map (two-tailed, one sample t-test, $p<0.01$), corresponding to Visual Network (VN) component in the control group, respectively. (B), (E), and (H): Topographic images of ICA-derived group-averaged r-map, z-map, and t-map (two-tailed, one sample t-test, $p<0.01$), corresponding to VN component in CLBP group, respectively. (C), (F), and (I): Topographic images of

between-group differences (Control *minus* CLBP contrast) r-map, z-map, and t-map (two-tailed, two sample t-test, $p<0.01$), corresponding to VN component, respectively.

According to the *t*-map of Figure 6.5G, 24 out of total 133 channels measured from the cortical surface were significantly correlated to temporal component of FPCN. Out of these 24 significantly correlated channels, 1 channel was located on left DLPFC, 4 channels were located on right DLPFC, 1 channel was located on left Pars Triangularis Broca's area (PT, BA 45), 2 channels were located on right PT, 1 channel was located on left Pars Pars Opercularis Broca's area (PO, BA 44), 1 channel was located on right PO, 1 channel was located on left PSMC, 3 channels were located on left Superior Temporal Gyrus (STG, BA 22), 3 channels were located on left SG, 1 channel was located on right SG, 2 channels were located in left AG, 1 channel was located in right AG, 1 channel was located on right SAC, 1 channel was lcoated on left V3, and 1 channel was lcoated in left Primary Visual Cortex (V1, BA 17).

6.4.1.4 Visual Network in control group

The group-averaged spatial component maps corresponding to Visual Network (VN) temporal component in the control group are shown in Figure 6.6. Figures 6.6A and 6D shows topographic images of group-averaged r-map and z-map corresponding to VN network component in the control group, respectively. Correspondingly, Figure 6.6G shows topographic t-map ($p<0.01$) to mark regions that have significant correlation between VN temporal component and ΔHbO_2 time series from each channel.

According to the *t*-map of Figure 6.6G, 18 out of total 133 channels measured from the cortical surface were significantly correlated to temporal component of FPCN. Out of these 18 significantly correlated channels, 1 channel was located in left M1, 3 channels were located on right M1, 2 channels were located on right S1, 1 channel was located on right SG, 2 channels were located in left SAC, 1 channel was located in left V3, 1 channel was located in right V3, 1 channel was located on left Visual Association Cortex 2 (V2, BA 18), 1 channel was located on right V2, 1 channel was located in left V1, and 2 channels were located in right V1.

6.4.2 ICA-derived resting-state functional networks in CLBP group

6.4.2.1 Default Mode Network in CLBP group

Figures 6.3B and 6.3E shows a topographic images of group-averaged r-map and z-map corresponding to default mode network component in CLBP group, respectively. Correspondingly, Figure 6.3H shows topographic t-map ($p<0.01$) to mark regions that have significant correlation between DMN temporal component and ΔHbO_2 time series from each channel.

According to the *t*-map of Figure 6.3H, 22 out of total 133 channels measured from the cortical surface were significantly correlated to temporal component of DMN. Out of these 22 significantly correlated channels, 5 channels were located on the left FPA, 3 channels were located on left DLPFC, 1 channel was located on left PT, 1 channel was located on left S1, 1 channel was located on right M1, 2 channels were located on left SG, 4 channels were located on left SAC, 4 channels were located on right SAC, and 1 channel was located on left AG

6.4.2.2 Somatomotor Network in CLBP group

Figures 6.4B and 6.4E shows topographic image of group-averaged r-map and z-map corresponding to Somatomotor Network component in CLBP group, respectively. Correspondingly, Figure 6.4H shows topographic t-map ($p<0.01$) to mark regions that have significant correlation between SMN temporal component and ΔHbO_2 time series from each channel.

According to the *t*-map of Figure 6.4H, 19 out of total 133 channels measured from the cortical surface were significantly correlated to temporal component of SMN. Out of these 19 significantly correlated channels, 4 channels were located on right PSMC, 4 channels were located on left M1, 3 channels were located on right M1, 1 channel was located in left S1, 4 channels were located in left SAC, 2 channels were located in right SAC, and 1 channel was located in left SG.

6.4.2.3 Fronto-parietal Control Network in CLBP group

Figures 6.5B and 6.5E shows topographic image of group-averaged r-map and z-map corresponding to Fronto-parietal Control Network component in CLBP group, respectively. Correspondingly, Figure 6.5H shows topographic t-map ($p<0.01$) to mark regions that have significant correlation between FPCN temporal component and ΔHbO_2 time series from each channel.

According to the *t*-map of Figure 6.5H, 10 out of total 133 channels measured from the cortical surface were significantly correlated to temporal component of FPCN. Out of these ten significantly correlated channels, 3 channels were located on right DLPFC, 2 channels were located on left PT, 1 channel was located on right PT, 1 channel was

located on left PO, 1 channel was located on left SG, and 2 channels were located on right SAC.

6.4.2.4 Visual Network in CLBP group

Figures 6.6B and 6.6E shows topographic imagess of group-averaged r-map and z-map corresponding to Visual Network component in CLBP group, respectively. Correspondingly, Figure 6.6H shows topographic t-map ($p<0.01$) to mark regions that have significant correlation between VN temporal component and ΔHbO_2 time series from each channel.

According to the *t*-map of Figure 6.6H, 14 out of total 133 channels measured from the cortical surface were significantly correlated to temporal component of VN. Out of these 14 significantly correlated channels, 1 channel was located on right S1, 1 channel was located in left SAC, 6 channels were located in right SAC, 1 channel was located in left V3, 1 channel was located in right V3, 1 channel was located in left V2, 1 channel was located in right V2, 1 channel was located in left V1, and 1 channel was located in right V1.

6.4.3 Comparison of RSFNs between Control and CLBP group

6.4.3.1 Default Mode Network differences between control group and CLBP group

Figures 6.3C and 6.3F show topographic images of differential r-map and z-map for control group minus CLBP group contrast corresponding to DMN component, respectively. Correspondingly, Figure 6.3I show topographic *t*-maps ($p<0.01$) to mark regions that have significant correlation differences between control group and CLBP

group, related to DMN component. According to the *t*-map of Fig. 6.3I, 4 out of total 133 channels measured from the cortical surface showed significantly increased correlation in Control group as compared to that of the CLBP group, corresponding to DMN component. Out of these 4 channels which showed significant differences in correlation, 1 channel was located in right DLPFC, 1 channel was located in right SG, I channel was located in right Middle Temporal Gyrus (MTG, BA 21), and 1 channel was located in right Fusiform Gyrus (FG, BA 37).

6.4.3.2 Somatomotor Network differences between control group and CLBP group

Figures 6.4C and 6.4F shows topographic images of differential r-map and z-map for control group minus CLBP group contrast corresponding to SMN component, respectively. Correspondingly, Figure 6.4I shows topographic *t*-maps ($p<0.01$) to mark regions that have significant correlation differences between control group and CLBP group, related to SMN component. According to the *t*-map of Fig. 6.4I, none of total 133 channels measured from the cortical surface showed significant differences in correlation corresponding to SMN component, between Control group and CLBP group,

6.4.3.3 Fronto-parietal Control Network differences between control group and CLBP group

Figures 6.5C and 6.5F show topographic images of differential r-map and z-map for control group minus CLBP group contrast corresponding to FPCN component, respectively. Correspondingly, Figure 6.5I shows topographic *t*-maps ($p<0.01$) to mark regions that have significant correlation differences between control group and CLBP

group, related to FPCN component. According to the *t*-map of Fig. 6.3I, 4 out of total 133 channels measured from the cortical surface showed significantly increased correlation in Control group as compared to that of the CLBP group, corresponding to FPCN component. Out of these 4 channels which showed significant differences in correlation, 1 channel was located on right SG, 2 channels were located on left V1, and 1 channel was located in right V1.

6.4.3.4 Visual Network differences between control group and CLBP group

Figures 6.6C and 6.6F show topographic images of differential r-map and z-map for control group minus CLBP group contrast corresponding to VN component, respectively. Correspondingly, Figure 6.6I shows topographic *t*-maps ($p<0.01$) to mark regions that have significant correlation differences between control group and CLBP group, related to VN component. According to the *t*-map of Fig. 6.6I, none of total 133 channels measured from the cortical surface showed significant differences in correlation corresponding to VN component, between Control group and CLBP group.

6.5 Discussion

The present study identified four ICA-derived resting-state functional networks in both controls as well CLBP patients using fNIRS. Furthermore, I compared and contrasted the RSFNs between healthy (elderly) controls and CLBP patients. The observed RSFNs and corresponding interpretations are summarized below.

6.5.1 Default Mode Network in Healthy and CLBP groups

DMN is a set of cortical and sub-cortical regions known to be more active during resting state as compared to that of during task performance (Buckner et al., 2008; Raichle et al., 2001; Shulman et al., 1997). DMN is associated with self-referential processing. Core regions associated with brain's DMN are bilateral Prefrontal cortex (PFC, BAs 9, 10), Anterior Cingulate Cortex (ACC, BAs 24, 32), Posterior cingulate cortex/retrosplenial cortex (PCC/RSP, BAs 29/30, 23/31), bilateral Inferior parietal lobule (IPL, BAs 39 & 40), and Lateral temporal cortex (LTC, BA 21) (Buckner et al., 2008). In this study, in the control group, I also observed significant correlations between DMN temporal component and several DMN constituents, such as bilateral prefrontal regions (BAs 9, 10), bilateral AG (BA 39), bilateral SG (BA 40) [see Fig. 6.3G]. Apart from significant correlations in DMN related regions, I observed significant correlations between DMN temporal component and several non-DMN regions, such as in bilateral S1, bilateral M1, bilateral SAC, and bilateral V3 of the control group. Whereas, in CLBP group, Significant correlations between the DMN-temporal component and DMN constituents were not bilateral. DMN regions which showed significant correlations with DMN temporal component were left FPA (BA 10), left DLPFC (BA 9), left SG (BA 40) and Left AG (BA 39) [see Fig. 6.3H]. Non-DMN regions which showed significant correlations with DMN temporal component were left PT, left S1, right M1, and bilateral SAC.

Numerous studies have demonstrated that the presence of chronic pain alters the functional connectivity among different brain regions. Recent fMRI studies have shown alterations in DMN connectivity in patients with chronic back pain (Baliki et al., 2008), neuropathic pain (Cauda et al., 2009), fibromyalgia (Napadow et al., 2010). Also, a recent RS-fMRI study also reported abnormal functional connectivity within DMN regions of

patients suffering from chronic back pain, complex regional pain syndrome, and knee osteoarthritis (Baliki, Mansour, Baria, & Apkarian, 2014). A recent structural MRI study reported that fibromyalgia patients' patients had significantly reduced total gray matter volume and 3.3 times greater age-associated decrease in gray matter volume as compared to that of the healthy controls (Kuchinad et al., 2007). Furthermore, reduction in gray matter density in the prefrontal cortex and thalamus of patients with chronic back pain is reported (Apkarian, Sosa, Sonty, et al., 2004). In this study, I observed that several DMN constituents in right cerebral hemisphere showed significantly increased correlations with DMN temporal component of the control group as compared to that of the CLBP group. Cortical regions which showed significant differences were right DLPFC (BA 9), right SG (BA 40) and MTG (BA 21) [see Fig. 6.3I]. Overall, I identified Default Mode Network in both healthy controls and CLBP patients, and the results suggest that resting state functional connectivity within DMN regions is compromised due to Chronic low back pain condition, specifically in right DMN regions.

6.5.2 Somatomotor Network in Healthy and CLBP groups

The Somatomotor Network includes the Precentral-gyrus/Primary Motor Cortex (BA 4), postcentral-gyrus/Primary Somatosensory Cortex (BAs 1, 2 & 3), and medial frontal gyri (BA 8 & 9), and supplementary motor area (BA 6) (Biswal, Yetkin, Haughton, & Hyde, 1995). In this study, in the control group, I also observed significant correlations between SMN temporal-component and several SMN constituents, such as bilateral PSMC (BA 6), bilateral M1 (BA 4), left S1 (BAs 1, 2 & 3), and right FEF (BA 8) regions [see Fig. 6.4G]. Apart from significant correlations in SMN related regions, I observed

significant correlations between SMN temporal component and several minor regions of non-SMN regions, such as in bilateral SAC, left SG, left AG, and left Subcentral Area. Whereas, in CLBP group, SMN regions which showed significant correlations with SMN temporal component were right PSMC (BA 6), bilateral M1 (BA 4), left S1 [see Fig. 6.4H]. Non-SMN regions which showed significant correlations with SMN temporal component were bilateral SAC and left SG. Between-groups comparison did not show any significant differences in SMN between control and CLBP groups [see Fig. 6.4I]. Overall I identified Somatomotor Network in both healthy controls and CLBP patients.

6.5.3 Fronto-parietal Control Network in Healthy and CLBP groups

Fronto-parietal Control Network mainly includes the lateral prefrontal cortex (lateral parts of BAs 9, 10, 44, 45, 46), ACC, and inferior parietal Lobule (BAs 39 & 40); it is suggested to be involved in cognitive control and decision-making processes (Vincent, Kahn, Snyder, Raichle, & Buckner, 2008). In this study, in the control group, I also observed significant correlations between FPCN temporal component and several FPCN constituents, such as in bilateral lateral prefrontal regions (BAs 9, 44, 45, & 46), bilateral AG (BA 39), and bilateral SG (BA 40) [see Fig. 6.5G]. Apart from significant correlations in FPCN related regions, I observed significant correlations between FPCN temporal component and several non- FPCN regions, such as in left PSMC, left STG, right SAC, left V1 and left V3 of the control group. Whereas, in CLBP group, the number of channels with significant correlations between the FPCN-temporal component and FPCN constituents were very less as compared to that of the control group. FPCN regions which showed significant correlations with FPCN temporal component were right DLPFC (BAs

9 & 46), left SG (BA 40), bilateral PT (BA 45), and left PO (BA 44 [see Fig. 6.5H]). Non-FPCN region which showed significant correlations with FPCN temporal component is right SAC.

In between-group differences, I observed that right SG and bilateral V1 regions showed significantly increased correlations with FPCN temporal component of the control group as compared to that of the CLBP group [see Fig. 6.5I]. However, only one channel is right SG showed a significant difference. Overall I identified fronto-parietal control network in both healthy controls and CLBP patients. Furthermore, I observed abnormal FPCN in CLBP patients which may indicate abnormal cognitive control or decision-making abilities in CLBP patients.

6.5.4 Visual Network in Healthy and CLBP groups

Visual Network mainly includes most of occipital cortex (such as Primary Visual Cortex BA 17; Visual association area 2; BA 18, and Visual association area 3; BA 19) (Beckmann, DeLuca, Devlin, & Smith, 2005; Power et al., 2011; Smith et al., 2009; Yeo et al., 2011). In this study, in the control group, I also observed significant correlations between VN temporal component and several VN constituents, such as bilateral V1 (BA 17), bilateral V2 (BA 18), and bilateral V3 regions [see Fig. 6.6G]. Apart from significant correlations in VN related regions, I observed significant correlations between VN temporal component and several regions of non-VN regions, such as in bilateral SAC, right M1, right S1, and right SG. The CLBP group also showed significant correlations between VN temporal component and VN network constituents, such as bilateral V1, bilateral V2, and bilateral V3 regions [see Fig. 6.6H]. Non-VN regions which showed

significant correlations with VN temporal component were bilateral SAC and right S1. Between-groups comparison did not show any significant differences in VN between control and CLBP groups [see Fig. 6.6I]. Overall, I identified Visual Network in both healthy controls and CLBP patients.

6.6 Limitations

Major technical limitation in this study is that I could not identify subcortical/deeper network constituents since fNIRS can probe only superficial layers of cerebral cortex. Also, there is a possibility that measured fNIRS may include contamination from extra-cranial vasculature, even after global noise regression. Extracranial vasculature noise in measured fNIRS signals can be further minimized by using additional recordings of short source-detector separations (0.8 - 1 cm) as noise regressors (Tian et al., 2011).

6.7 Conclusions

In this study, RS-fNIRS was utilized to compare and contrast ICA-derived RSFNs between 12 elderly patients with CLBP and 12 age-matched healthy controls. I identified four consistent RSFNs (Default Mode Network, Somatomotor Network, Fronto-parietal Control Network, and Visual Network) among the healthy controls and CLBP patients. Also, CLBP group exhibited abnormal DMN connectivity, specifically in the right prefrontal cortex (BA 9) and right Supramarginal Gyrus (BA 40). The present study clearly demonstrates that fNIRS are a portable and complementary neuroimaging tool to study ICA-derived RSFNs in healthy and CLBP participants, and to reveal abnormal DMN connectivity in CLBP patients.

Chapter 7

Conclusions

In Chapter 2, fNIRS was used to study neural correlats of selective attention processes among 15 veterans with PTSD and 13 age-/gender- matched healthy controls. After learning and implementing the general linear model, I was able to obtain multi-channel fNIRS-based topography and identify/map Stroop-evoked prefrontal activtations in both subject groups. While performing the color-word Stroop task (Incongruent Stroop task), healthy controls showed hemodynamic activations in lateral prefrontal cortex regions, especially in left DLPFC and left Pars opercularis, whereas veterans with PTSD failed to activate those cortical regions during the same Stroop task. Also, significant negative correlation was observed between task reaction times and HbO2 responses from left DLPFC during color-word matching task. These observations implicate difficulty experienced by the PTSD subjects in coping up with Stroop interference. Overall, I demonstrated that fNIRS is a portable and complementary neuroimaging tool to study the neural correlates of selective attention and interference in subjects with PTSD. This work was published in Scientific Reports Journal (Yennu et al., 2016).

In Chapters 3, fNIRS experiments were performed on 9 healthy volunteers to explore hemodynamic responses in the frontal cortex to low pain thermal stimulation (LPS) and high pain thermal stimulation (HPS) over the right TMJ region. By analyzing the temporal profiles of ΔHbO2 using cluster-based statistical tests, several regions of interest in the PFC, such as the DLPFC and the aPFC, were identified, where significant differences between ΔHbO2 responses to LPS and HPS were shown. Also, these two levels of pain were classified using a neural network-based classification algorithm. With

leave-one-out cross-validation, these two levels of pain were identified with 99% mean accuracy to high pain. Furthermore, the “internal mentation hypothesis” and the default-mode network were introduced to explain the temporal characteristics of HbO2 responses to HPS and LPS. This work was published in Journal of Applied Biobehavioral Research Journal (Yennu et al., 2013).

In Chapter 4, fNIRS experiments were performed on three separate groups of healthy participants, to test the robustness of temporal and spatial characteristics of prefrontal hemodynamics in response to noxious thermal stimulation over three body sites, namely, the right forearm, right temporomandibular joint, and left forearm, separately. During HPS, changes of HbO2 in the prefrontal cortex, especially in the DLPFC, were significantly increased, with similar temporal patterns and spatial localizations. In contrast, LPS did not result in any significant changes in HbO2 in the prefrontal regions in any of the three groups. These observations were highly consistent with previous reports by other acute pain-related studies. In addition, I introduced and optimally selected a variable recovery regressor to account for a peculiar global trend of HbO2 deactivation in the prefrontal cortex during the post-HPS period. This post-stimulation recovery regressor allowed me to identify and map deactivation regions in the prefrontal cortex, which may be attributed to global vasoconstriction due to induction of acute noxious pain. Overall, the temporal and spatial hemodynamic activities in the prefrontal cortex in response to acute thermal stimulation were consistent and robust regardless of the stimulation sites. Therefore, multi-channel fNIRS can be used to reveal neural correlated of acute pain, and may have great potential for future clinical

applications. This work was published in A manuscript for this work was recently submitted to Neurophotonics Journal for publication.

In Chapter 5, fNIRS was used to compare and contrast cortical hemodynamic responses from 16 elderly patients with Chronic Low Back Pain (CLBP) and 15 age-/gender- matched healthy controls while performing leg raising tasks. Leg raising tasks induced significant pain in CLBP patients before treatment as well as after the treatment as compared to that of healthy controls. During the right-leg-raising (RLR) as well as the left-leg-raising (LLR) tasks, healthy controls showed significant HbO2 activations in pre-motor and primary motor cortices. Whereas, CLBP patients before treatment activated several pain-related cortical regions during leg raising tasks, especially activations in the prefrontal cortex were predominant. Relative to controls, CLBP patients after treatment did not show any significant differences in cortical responses during RLR task. Also, during RLR task, CLBP patients after treatment exhibited reduced prefrontal responses as compared to that of before treatment. These observations may suggest that abnormal prefrontal cortex function of CLBP patients was reversed following treatment. Overall, I demonstrated that fNIRS can be used as a portable and complementary neuroimaging tool to study the neural correlates of pain induced by leg-raising-tasks in subjects with CLBP, and to monitor treatment effects as well.

In Chapter 6, resting-state fNIRS was used to compare and contrast independent-component-analysis (ICA) derived resting-state functional networks (RSFNs) from 12 elderly patients with CLBP and 12 age-matched healthy controls. I identified four consistent RSFNs, namely, (1) Default Mode Network (DMN), (2) Somatomotor Network, (3) Fronto-parietal Control Network, and (4) Visual Network, among the healthy controls

and CLBP patients. Furthermore, CLBP group exhibited abnormal DMN connectivity, specifically in the right prefrontal cortex (BA 9) and right Supramarginal Gyrus (BA 40). Overall, I demonstrated feasibilty of fNIRS to study ICA-derived RSFNs in healthy and CLBP participants, and to reveal abnormal DMN connectivity in CLBP patients.

All in all, my doctoral research has concluded three major findings:

(1) noxious and innocuous thermal pain can be objectively measured and discriminated by fNIRS taken in the frontal cortical regions of healthy subjects;

(2) fNIRS can serve as an effective brain imaging modality to map pain-induced hemodynamic activities and resting-state brain functional connectivity in all cortical regions of both normal subjects and subjects with CLBP, as well as to identify any characteristic distinctions in hemodynamic signals between normal subjects and subjects with CLBP.

(3) fNIRS offers a non-invasive means to reveal potential restoration of normal brain functions in CLBP subjects after exercise treatments.

Appendix A

Matlab Code for Word-Matching Stroop Task

```
function varargout = stroop1new(varargin)
% STROOP1NEW M-file for stroop1new.fig
%      STROOP1NEW, by itself, creates a new STROOP1NEW or raises the existing
%      singleton*.
%
%      H = STROOP1NEW returns the handle to a new STROOP1NEW or the handle to
%      the existing singleton*.
%
%      STROOP1NEW('CALLBACK',hObject,eventData,handles,...) calls the local
%      function named CALLBACK in STROOP1NEW.M with the given input arguments.
%
%      STROOP1NEW('Property','Value',...) creates a new STROOP1NEW or raises the
%      existing singleton*.  Starting from the left, property value pairs are
%      applied to the GUI before stroop1new_OpeningFcn gets called.  An
%      unrecognized property name or invalid value makes property application
%      stop.  All inputs are passed to stroop1new_OpeningFcn via varargin.
%
%      *See GUI Options on GUIDE's Tools menu.  Choose "GUI allows only one
%      instance to run (singleton)".
%
% See also: GUIDE, GUIDATA, GUIHANDLES

% Edit the above text to modify the response to help stroop1new

% Last Modified by GUIDE v2.5 29-Aug-2011 16:35:15

% Begin initialization code - DO NOT EDIT
gui_Singleton = 1;
gui_State = struct('gui_Name',       mfilename, ...
                   'gui_Singleton',  gui_Singleton, ...
                   'gui_OpeningFcn', @stroop1new_OpeningFcn, ...
                   'gui_OutputFcn',  @stroop1new_OutputFcn, ...
                   'gui_LayoutFcn',  [] , ...
                   'gui_Callback',   []);
if nargin && ischar(varargin{1})
    gui_State.gui_Callback = str2func(varargin{1});
end

if nargout
    [varargout{1:nargout}] = gui_mainfcn(gui_State, varargin{:});
else
    gui_mainfcn(gui_State, varargin{:});
end
% End initialization code - DO NOT EDIT
```

```
% --- Executes just before stroop1new is made visible.
function stroop1new_OpeningFcn(hObject, eventdata, handles, varargin)
% This function has no output args, see OutputFcn.
% hObject    handle to figure
% eventdata  reserved - to be defined in a future version of MATLAB
% handles    structure with handles and user data (see GUIDATA)
% varargin   command line arguments to stroop1new (see VARARGIN)

% Choose default command line output for stroop1new
handles.output = hObject;

% Update handles structure
guidata(hObject, handles);

% UIWAIT makes stroop1new wait for user response (see UIRESUME)
% uiwait(handles.figure1);


% --- Outputs from this function are returned to the command line.
function varargout = stroop1new_OutputFcn(hObject, eventdata, handles)
% varargout  cell array for returning output args (see VARARGOUT);
% hObject    handle to figure
% eventdata  reserved - to be defined in a future version of MATLAB
% handles    structure with handles and user data (see GUIDATA)

% Get default command line output from handles structure
handles = guihandles(hObject);
handles.correct=0;
set(handles.pushbutton1,'visible','off');
set(handles.pushbutton2,'visible','off');
set(handles.text2,'visible','off');
guidata(hObject,handles)
tic
pause(30)
for n=1:1:8
    handles.stimulus(n)=toc;
    set(handles.pushbutton1,'visible','on');
set(handles.pushbutton2,'visible','on');
set(handles.text2,'visible','on');
guidata(hObject,handles)
for i=1:1:5
c_word = {'YELLOW','RED', 'GREEN' ,'BLUE' ,'BLACK'};
% c = {'y','r','g','b','k'};
c=[1 2 3 4 5];
```

```
rc = randperm(5);
yc=c(5);
switch yc
   case 1
      flag=[1 1 0];
   case 2
      flag=[1 0 0];
   case 3
      flag=[0 1 0];
   case 4
      flag=[0 0 1];
   case 5
      flag=[0 0 0];
end
set(handles.text2,'string',c_word(rc(1)))
set(handles.text2,'ForegroundColor',flag)
handles.x=ceil(2*rand(1,1))
guidata(hObject,handles)
switch handles.x
   case 1
set(handles.pushbutton1,'string',c_word(rc(1)));
set(handles.pushbutton2,'string',c_word(rc(2)));

   case 2
set(handles.pushbutton1,'string',c_word(rc(2)));
set(handles.pushbutton2,'string',c_word(rc(1)));
end
uiwait(gcf)
handles.blockcor(i)=getappdata(0,'UserData');
guidata(hObject,handles)
end
handles.responce(n)=sum(handles.blockcor)
handles.blockcor=0;
handles.react(n)=toc-handles.stimulus(n)

set(handles.pushbutton1,'visible','off');
set(handles.pushbutton2,'visible','off');
set(handles.text2,'visible','off');
pause(15)
guidata(hObject,handles)
end
pause(30)

save('output_strp1.mat','handles');
guidata(hObject,handles)
close all
```

```
% --- Executes on button press in pushbutton1.
function pushbutton1_Callback(hObject, eventdata, handles)
handles = guidata(gcbo);
if handles.x==1
handles.correct=handles.correct+1;
setappdata(0,'UserData',handles.correct);
else
    setappdata(0,'UserData',handles.correct)
end
guidata(hObject,handles);
uiresume
guidata(hObject,handles);


% hObject    handle to pushbutton1 (see GCBO)
% eventdata  reserved - to be defined in a future version of MATLAB
% handles    structure with handles and user data (see GUIDATA)


% --- Executes on button press in pushbutton2.
function pushbutton2_Callback(hObject, eventdata, handles)
handles = guidata(gcbo);
if handles.x==2
handles.correct=handles.correct+1;
setappdata(0,'UserData',handles.correct);
else
    setappdata(0,'UserData',handles.correct)
end
guidata(hObject,handles);
uiresume
guidata(hObject,handles);
% hObject    handle to pushbutton2 (see GCBO)
% eventdata  reserved - to be defined in a future version of MATLAB
% handles    structure with handles and user data (see GUIDATA)


% --- Executes on key press with focus on figure1 and none of its controls.
function figure1_KeyPressFcn(hObject, eventdata, handles)
switch eventdata.Key
case 'leftarrow'
%
 pushbutton1_Callback(hObject, eventdata, handles);
case 'rightarrow'
%
```

```
pushbutton2_Callback(hObject, eventdata, handles);
end
% hObject    handle to figure1 (see GCBO)
% eventdata  structure with the following fields (see FIGURE)
%   Key: name of the key that was pressed, in lower case
%   Character: character interpretation of the key(s) that was pressed
%   Modifier: name(s) of the modifier key(s) (i.e., control, shift) pressed
% handles    structure with handles and user data (see GUIDATA)


% --- Executes on key release with focus on figure1 and none of its controls.
function figure1_KeyReleaseFcn(hObject, eventdata, handles)
% hObject    handle to figure1 (see GCBO)
% eventdata  structure with the following fields (see FIGURE)
%   Key: name of the key that was released, in lower case
%   Character: character interpretation of the key(s) that was released
%   Modifier: name(s) of the modifier key(s) (i.e., control, shift) released
% handles    structure with handles and user data (see GUIDATA)


% --- Executes during object creation, after setting all properties.
function pushbutton1_CreateFcn(hObject, eventdata, handles)
% hObject    handle to pushbutton1 (see GCBO)
% eventdata  reserved - to be defined in a future version of MATLAB
% handles    empty - handles not created until after all CreateFcns called


% --- Executes during object deletion, before destroying properties.
function pushbutton1_DeleteFcn(hObject, eventdata, handles)
% hObject    handle to pushbutton1 (see GCBO)
% eventdata  reserved - to be defined in a future version of MATLAB
% handles    structure with handles and user data (see GUIDATA)


% --- If Enable == 'on', executes on mouse press in 5 pixel border.
% --- Otherwise, executes on mouse press in 5 pixel border or over pushbutton1.
function pushbutton1_ButtonDownFcn(hObject, eventdata, handles)
% hObject    handle to pushbutton1 (see GCBO)
% eventdata  reserved - to be defined in a future version of MATLAB
% handles    structure with handles and user data (see GUIDATA)


% --- If Enable == 'on', executes on mouse press in 5 pixel border.
% --- Otherwise, executes on mouse press in 5 pixel border or over pushbutton2.
function pushbutton2_ButtonDownFcn(hObject, eventdata, handles)
% hObject    handle to pushbutton2 (see GCBO)
```

```
% eventdata  reserved - to be defined in a future version of MATLAB
% handles    structure with handles and user data (see GUIDATA)


% --- Executes during object creation, after setting all properties.
function pushbutton2_CreateFcn(hObject, eventdata, handles)
% hObject    handle to pushbutton2 (see GCBO)
% eventdata  reserved - to be defined in a future version of MATLAB
% handles    empty - handles not created until after all CreateFcns called


% --- Executes during object deletion, before destroying properties.
function pushbutton2_DeleteFcn(hObject, eventdata, handles)
% hObject    handle to pushbutton2 (see GCBO)
% eventdata  reserved - to be defined in a future version of MATLAB
% handles    structure with handles and user data (see GUIDATA)
```

Appendix B

Matlab Code for Color-Word Stroop Task

```
function varargout = stroop2new(varargin)
% STROOP2NEW M-file for stroop2new.fig
%      STROOP2NEW, by itself, creates a new STROOP2NEW or raises the existing
%      singleton*.
%
%      H = STROOP2NEW returns the handle to a new STROOP2NEW or the handle to
%      the existing singleton*.
%
%      STROOP2NEW('CALLBACK',hObject,eventData,handles,...) calls the local
%      function named CALLBACK in STROOP2NEW.M with the given input arguments.
%
%      STROOP2NEW('Property','Value',...) creates a new STROOP2NEW or raises the
%      existing singleton*.  Starting from the left, property value pairs are
%      applied to the GUI before stroop2new_OpeningFcn gets called.  An
%      unrecognized property name or invalid value makes property application
%      stop.  All inputs are passed to stroop2new_OpeningFcn via varargin.
%
%      *See GUI Options on GUIDE's Tools menu.  Choose "GUI allows only one
%      instance to run (singleton)".
%
% See also: GUIDE, GUIDATA, GUIHANDLES

% Edit the above text to modify the response to help stroop2new

% Last Modified by GUIDE v2.5 04-Aug-2011 05:12:47

% Begin initialization code - DO NOT EDIT
gui_Singleton = 1;
gui_State = struct('gui_Name',       mfilename, ...
                   'gui_Singleton',  gui_Singleton, ...
                   'gui_OpeningFcn', @stroop2new_OpeningFcn, ...
                   'gui_OutputFcn',  @stroop2new_OutputFcn, ...
                   'gui_LayoutFcn',  [] , ...
                   'gui_Callback',   []);
if nargin && ischar(varargin{1})
    gui_State.gui_Callback = str2func(varargin{1});
end

if nargout
    [varargout{1:nargout}] = gui_mainfcn(gui_State, varargin{:});
else
    gui_mainfcn(gui_State, varargin{:});
end
% End initialization code - DO NOT EDIT
```

```
% --- Executes just before stroop2new is made visible.
function stroop2new_OpeningFcn(hObject, eventdata, handles, varargin)
% This function has no output args, see OutputFcn.
% hObject    handle to figure
% eventdata  reserved - to be defined in a future version of MATLAB
% handles    structure with handles and user data (see GUIDATA)
% varargin   command line arguments to stroop2new (see VARARGIN)

% Choose default command line output for stroop2new
handles.output = hObject;

% Update handles structure
guidata(hObject, handles);

% UIWAIT makes stroop2new wait for user response (see UIRESUME)
% uiwait(handles.figure1);


% --- Outputs from this function are returned to the command line.
function varargout = stroop2new_OutputFcn(hObject, eventdata, handles)
% varargout  cell array for returning output args (see VARARGOUT);
% hObject    handle to figure
% eventdata  reserved - to be defined in a future version of MATLAB
% handles    structure with handles and user data (see GUIDATA)

% Get default command line output from handles structure
handles = guihandles(hObject);
handles.correct=0;
set(handles.pushbutton1,'visible','off');
set(handles.pushbutton2,'visible','off');
set(handles.text2,'visible','off');
guidata(hObject,handles)
tic
pause(30)
for n=1:1:8
    handles.stimulus(n)=toc;
    set(handles.pushbutton1,'visible','on');
set(handles.pushbutton2,'visible','on');
set(handles.text2,'visible','on');
guidata(hObject,handles)
for i=1:1:5
c_word = {'YELLOW','RED', 'GREEN' ,'BLUE' ,'BLACK'};
% c = {'y','r','g','b','k'};
c=[1 2 3 4 5];
```

```
rc = randperm(5);
yc=c(rc(2));
switch yc
   case 1
      flag=[1 1 0];
   case 2
      flag=[1 0 0];
   case 3
      flag=[0 1 0];
   case 4
      flag=[0 0 1];
   case 5
      flag=[0 0 0];
end
set(handles.text2,'string',c_word(rc(1)))
set(handles.text2,'ForegroundColor',flag)
handles.x=ceil(2*rand(1,1))
guidata(hObject,handles)
switch handles.x
   case 1
set(handles.pushbutton1,'string',c_word(rc(2)));
set(handles.pushbutton2,'string',c_word(rc(1)));

   case 2
set(handles.pushbutton1,'string',c_word(rc(1)));
set(handles.pushbutton2,'string',c_word(rc(2)));
end
uiwait(gcf)
handles.blockcor(i)=getappdata(0,'UserData');
guidata(hObject,handles)
end
handles.responce(n)=sum(handles.blockcor)
handles.blockcor=0;
handles.react(n)=toc-handles.stimulus(n)

set(handles.pushbutton1,'visible','off');
set(handles.pushbutton2,'visible','off');
set(handles.text2,'visible','off');
pause(15)
guidata(hObject,handles)
end
pause(30)

save('output_strp2.mat','handles');
guidata(hObject,handles)
close all
```

```
% --- Executes on button press in pushbutton1.
function pushbutton1_Callback(hObject, eventdata, handles)
handles = guidata(gcbo);
if handles.x==1
handles.correct=handles.correct+1;
setappdata(0,'UserData',handles.correct);
else
    setappdata(0,'UserData',handles.correct)
end
guidata(hObject,handles);
uiresume
guidata(hObject,handles);


% hObject    handle to pushbutton1 (see GCBO)
% eventdata  reserved - to be defined in a future version of MATLAB
% handles    structure with handles and user data (see GUIDATA)


% --- Executes on button press in pushbutton2.
function pushbutton2_Callback(hObject, eventdata, handles)
handles = guidata(gcbo);
if handles.x==2
handles.correct=handles.correct+1;
setappdata(0,'UserData',handles.correct);
else
    setappdata(0,'UserData',handles.correct)
end
guidata(hObject,handles);
uiresume
guidata(hObject,handles);
% hObject    handle to pushbutton2 (see GCBO)
% eventdata  reserved - to be defined in a future version of MATLAB
% handles    structure with handles and user data (see GUIDATA)


% --- Executes on key press with focus on figure1 and none of its controls.
function figure1_KeyPressFcn(hObject, eventdata, handles)
switch eventdata.Key
case 'leftarrow'
%
 pushbutton1_Callback(hObject, eventdata, handles);
case 'rightarrow'
%
```

```
pushbutton2_Callback(hObject, eventdata, handles);
end
% hObject    handle to figure1 (see GCBO)
% eventdata  structure with the following fields (see FIGURE)
%   Key: name of the key that was pressed, in lower case
%   Character: character interpretation of the key(s) that was pressed
%   Modifier: name(s) of the modifier key(s) (i.e., control, shift) pressed
% handles    structure with handles and user data (see GUIDATA)


% --- Executes on key release with focus on figure1 and none of its controls.
function figure1_KeyReleaseFcn(hObject, eventdata, handles)
% hObject    handle to figure1 (see GCBO)
% eventdata  structure with the following fields (see FIGURE)
%   Key: name of the key that was released, in lower case
%   Character: character interpretation of the key(s) that was released
%   Modifier: name(s) of the modifier key(s) (i.e., control, shift) released
% handles    structure with handles and user data (see GUIDATA)


% --- Executes during object creation, after setting all properties.
function pushbutton1_CreateFcn(hObject, eventdata, handles)
% hObject    handle to pushbutton1 (see GCBO)
% eventdata  reserved - to be defined in a future version of MATLAB
% handles    empty - handles not created until after all CreateFcns called


% --- Executes during object deletion, before destroying properties.
function pushbutton1_DeleteFcn(hObject, eventdata, handles)
% hObject    handle to pushbutton1 (see GCBO)
% eventdata  reserved - to be defined in a future version of MATLAB
% handles    structure with handles and user data (see GUIDATA)


% --- If Enable == 'on', executes on mouse press in 5 pixel border.
% --- Otherwise, executes on mouse press in 5 pixel border or over pushbutton1.
function pushbutton1_ButtonDownFcn(hObject, eventdata, handles)
% hObject    handle to pushbutton1 (see GCBO)
% eventdata  reserved - to be defined in a future version of MATLAB
% handles    structure with handles and user data (see GUIDATA)


% --- If Enable == 'on', executes on mouse press in 5 pixel border.
% --- Otherwise, executes on mouse press in 5 pixel border or over pushbutton2.
function pushbutton2_ButtonDownFcn(hObject, eventdata, handles)
% hObject    handle to pushbutton2 (see GCBO)
```

```
% eventdata  reserved - to be defined in a future version of MATLAB
% handles    structure with handles and user data (see GUIDATA)


% --- Executes during object creation, after setting all properties.
function pushbutton2_CreateFcn(hObject, eventdata, handles)
% hObject    handle to pushbutton2 (see GCBO)
% eventdata  reserved - to be defined in a future version of MATLAB
% handles    empty - handles not created until after all CreateFcns called


% --- Executes during object deletion, before destroying properties.
function pushbutton2_DeleteFcn(hObject, eventdata, handles)
% hObject    handle to pushbutton2 (see GCBO)
% eventdata  reserved - to be defined in a future version of MATLAB
% handles    structure with handles and user data (see GUIDATA)
```

Appendix C

Matlab code for Global Signal Regression

```
x1=load('D:\chronic pain subjects hb data\hb data for pain subjects mat
files\subject1_rightleg.mat');
x2=load('D:\chronic pain subjects hb data\hb data for pain subjects mat
files\subject2_rightleg.mat');
x3=load('D:\chronic pain subjects hb data\hb data for pain subjects mat
files\subject3_rightleg.mat');
x4=load('D:\chronic pain subjects hb data\hb data for pain subjects mat
files\subject4_rightleg.mat');
x5=load('D:\chronic pain subjects hb data\hb data for pain subjects mat
files\subject5_rightleg.mat');
x6=load('D:\chronic pain subjects hb data\hb data for pain subjects mat
files\subject6_rightleg.mat');
x7=load('D:\chronic pain subjects hb data\hb data for pain subjects mat
files\subject7_rightleg.mat');
x8=load('D:\chronic pain subjects hb data\hb data for pain subjects mat
files\subject8_rightleg.mat');
x9=load('D:\chronic pain subjects hb data\hb data for pain subjects mat
files\subject9_rightleg.mat');
x10=load('D:\chronic pain subjects hb data\hb data for pain subjects mat
files\subject10_rightleg.mat');
x11=load('D:\chronic pain subjects hb data\hb data for pain subjects mat
files\subject11_rightleg.mat');
x12=load('D:\chronic pain subjects hb data\hb data for pain subjects mat
files\subject12_rightleg.mat');
x13=load('D:\chronic pain subjects hb data\hb data for pain subjects mat
files\subject13_rightleg.mat');
x14=load('D:\chronic pain subjects hb data\hb data for pain subjects mat
files\subject14_rightleg.mat');
x15=load('D:\chronic pain subjects hb data\hb data for pain subjects mat
files\subject15_rightleg.mat');
x16=load('D:\chronic pain subjects hb data\hb data for pain subjects mat
files\subject16_rightleg.mat');

y1=load('D:\chronic pain subjects hb data\hb data for pain subjects mat
files\subject1_leftleg.mat');
y2=load('D:\chronic pain subjects hb data\hb data for pain subjects mat
files\subject2_leftleg.mat');
y3=load('D:\chronic pain subjects hb data\hb data for pain subjects mat
files\subject3_leftleg.mat');
y4=load('D:\chronic pain subjects hb data\hb data for pain subjects mat
files\subject4_leftleg.mat');
y5=load('D:\chronic pain subjects hb data\hb data for pain subjects mat
files\subject5_leftleg.mat');
```

```
y6=load('D:\chronic pain subjects hb data\hb data for pain subjects mat
files\subject6_leftleg.mat');
y7=load('D:\chronic pain subjects hb data\hb data for pain subjects mat
files\subject7_leftleg.mat');
y8=load('D:\chronic pain subjects hb data\hb data for pain subjects mat
files\subject8_leftleg.mat');
y9=load('D:\chronic pain subjects hb data\hb data for pain subjects mat
files\subject9_leftleg.mat');
y10=load('D:\chronic pain subjects hb data\hb data for pain subjects mat
files\subject10_leftleg.mat');
y11=load('D:\chronic pain subjects hb data\hb data for pain subjects mat
files\subject11_leftleg.mat');
y12=load('D:\chronic pain subjects hb data\hb data for pain subjects mat
files\subject12_leftleg.mat');
y13=load('D:\chronic pain subjects hb data\hb data for pain subjects mat
files\subject13_leftleg.mat');
y14=load('D:\chronic pain subjects hb data\hb data for pain subjects mat
files\subject14_leftleg.mat');
y15=load('D:\chronic pain subjects hb data\hb data for pain subjects mat
files\subject15_leftleg.mat');
y16=load('D:\chronic pain subjects hb data\hb data for pain subjects mat
files\subject16_leftleg.mat');

for i=1:133 %% global signal regression
    stats=regstats(x1.HbO(:,i),mean(x1.HbO(:,:),2));
    x1_new.HbO(:,i)=stats.r;
    stats=regstats(x8.HbO(:,i),mean(x8.HbO(:,:),2));
    x8_new.HbO(:,i)=stats.r;
    stats=regstats(x2.HbO(:,i),mean(x2.HbO(:,:),2));
    x2_new.HbO(:,i)=stats.r;
    stats=regstats(x3.HbO(:,i),mean(x3.HbO(:,:),2));
    x3_new.HbO(:,i)=stats.r;
    stats=regstats(x4.HbO(:,i),mean(x4.HbO(:,:),2));
    x4_new.HbO(:,i)=stats.r;
    stats=regstats(x5.HbO(:,i),mean(x5.HbO(:,:),2));
    x5_new.HbO(:,i)=stats.r;
    stats=regstats(x6.HbO(:,i),mean(x6.HbO(:,:),2));
    x6_new.HbO(:,i)=stats.r;
    stats=regstats(x7.HbO(:,i),mean(x7.HbO(:,:),2));
    x7_new.HbO(:,i)=stats.r;
    stats=regstats(x9.HbO(:,i),mean(x9.HbO(:,:),2));
    x9_new.HbO(:,i)=stats.r;
    stats=regstats(x10.HbO(:,i),mean(x10.HbO(:,:),2));
    x10_new.HbO(:,i)=stats.r;
    stats=regstats(x11.HbO(:,i),mean(x11.HbO(:,:),2));
    x11_new.HbO(:,i)=stats.r;
```

```
    stats=regstats(x12.HbO(:,i),mean(x12.HbO(:,:),2));
    x12_new.HbO(:,i)=stats.r;
    stats=regstats(x13.HbO(:,i),mean(x13.HbO(:,:),2));
    x13_new.HbO(:,i)=stats.r;
     stats=regstats(x14.HbO(:,i),mean(x14.HbO(:,:),2));
    x14_new.HbO(:,i)=stats.r;
     stats=regstats(x15.HbO(:,i),mean(x15.HbO(:,:),2));
    x15_new.HbO(:,i)=stats.r;
     stats=regstats(x16.HbO(:,i),mean(x16.HbO(:,:),2));
    x16_new.HbO(:,i)=stats.r;

 end
xhbo{1,1}=x1_new.HbO;
xhbo{1,2}=x2_new.HbO;
xhbo{1,3}=x3_new.HbO;
xhbo{1,4}=x4_new.HbO;
xhbo{1,5}=x5_new.HbO;
xhbo{1,6}=x6_new.HbO;
xhbo{1,7}=x7_new.HbO;
xhbo{1,8}=x8_new.HbO;
xhbo{1,9}=x9_new.HbO;
xhbo{1,10}=x10_new.HbO;
xhbo{1,11}=x11_new.HbO;
xhbo{1,12}=x12_new.HbO;
xhbo{1,13}=x13_new.HbO;
xhbo{1,14}=x14_new.HbO;
xhbo{1,15}=x15_new.HbO;
xhbo{1,16}=x16_new.HbO;

for i=1:133 %% global signal regression
    stats=regstats(y1.HbO(:,i),mean(y1.HbO(:,:),2));
    y1_new.HbO(:,i)=stats.r;
    stats=regstats(y8.HbO(:,i),mean(y8.HbO(:,:),2));
    y8_new.HbO(:,i)=stats.r;
    stats=regstats(y2.HbO(:,i),mean(y2.HbO(:,:),2));
    y2_new.HbO(:,i)=stats.r;
    stats=regstats(y3.HbO(:,i),mean(y3.HbO(:,:),2));
    y3_new.HbO(:,i)=stats.r;
    stats=regstats(y4.HbO(:,i),mean(y4.HbO(:,:),2));
    y4_new.HbO(:,i)=stats.r;
    stats=regstats(y5.HbO(:,i),mean(y5.HbO(:,:),2));
    y5_new.HbO(:,i)=stats.r;
    stats=regstats(y6.HbO(:,i),mean(y6.HbO(:,:),2));
    y6_new.HbO(:,i)=stats.r;
    stats=regstats(y7.HbO(:,i),mean(y7.HbO(:,:),2));
    y7_new.HbO(:,i)=stats.r;
```

```
    stats=regstats(y9.HbO(:,i),mean(y9.HbO(:,:),2));
    y9_new.HbO(:,i)=stats.r;
    stats=regstats(y10.HbO(:,i),mean(y10.HbO(:,:),2));
    y10_new.HbO(:,i)=stats.r;
    stats=regstats(y11.HbO(:,i),mean(y11.HbO(:,:),2));
    y11_new.HbO(:,i)=stats.r;
    stats=regstats(y12.HbO(:,i),mean(y12.HbO(:,:),2));
    y12_new.HbO(:,i)=stats.r;
    stats=regstats(y13.HbO(:,i),mean(y13.HbO(:,:),2));
    y13_new.HbO(:,i)=stats.r;
     stats=regstats(y14.HbO(:,i),mean(y14.HbO(:,:),2));
    y14_new.HbO(:,i)=stats.r;
     stats=regstats(y15.HbO(:,i),mean(y15.HbO(:,:),2));
    y15_new.HbO(:,i)=stats.r;
     stats=regstats(y16.HbO(:,i),mean(y16.HbO(:,:),2));
    y16_new.HbO(:,i)=stats.r;
end
yhbo{1,1}=y1_new.HbO;
yhbo{1,2}=y2_new.HbO;
yhbo{1,3}=y3_new.HbO;
yhbo{1,4}=y4_new.HbO;
yhbo{1,5}=y5_new.HbO;
yhbo{1,6}=y6_new.HbO;
yhbo{1,7}=y7_new.HbO;
yhbo{1,8}=y8_new.HbO;
yhbo{1,9}=y9_new.HbO;
yhbo{1,10}=y10_new.HbO;
yhbo{1,11}=y11_new.HbO;
yhbo{1,12}=y12_new.HbO;
yhbo{1,13}=y13_new.HbO;
yhbo{1,14}=y14_new.HbO;
yhbo{1,15}=y15_new.HbO;
yhbo{1,16}=y16_new.HbO;

 fs = 8.13;
stim=[60 84 113 139 168 192];
dura=[ 14 14 14 14 14 14];
mod=[1 1 1 1 1 1];
for i=1:16
    y=xhbo{1,i};
        [beta_pain_rightleg(i,:,:)] = glm(y, {stim}, {dura}, {mod}, 1, 0, fs);
    end
for i = 1:16
    y=yhbo{1,i};
        [beta_pain_leftleg(i,:,:)] = glm(y, {stim}, {dura}, {mod}, 1, 0, fs);
end
```

Appendix D

Matlab code for Back-Reconstruction of Individual Resting-state functional networks by correlation approach

```
load('D:\chronic pain subjects hb data\group_ica_combined40components');
l1=length(x1_new.HbO);
l2=length(x2_new.HbO);
l3=length(x3_new.HbO);
l4=length(x4_new.HbO);
l5=length(x5_new.HbO);
l6=length(x6_new.HbO);
l7=length(x7_new.HbO);
l8=length(x8_new.HbO);
l9=length(x9_new.HbO);
l10=length(x10_new.HbO);
l11=length(x11_new.HbO);
l12=length(x12_new.HbO);
l13=length(y1_new.HbO);
l14=length(y2_new.HbO);
l15=length(y3_new.HbO);
l16=length(y4_new.HbO);
l17=length(y5_new.HbO);
l18=length(y6_new.HbO);
l19=length(y7_new.HbO);
l20=length(y8_new.HbO);
l21=length(y9_new.HbO);
l22=length(y10_new.HbO);
l23=length(y11_new.HbO);
l24=length(y12_new.HbO);

s1=ICcombined_ica(:,1:l1);
s2=ICcombined_ica(:,l1+1:l1+l2);
s3=ICcombined_ica(:,l1+l2+1:l1+l2+l3);
s4=ICcombined_ica(:,l1+l2+l3+1:l1+l2+l3+l4);
s5=ICcombined_ica(:,l1+l2+l3+l4+1:l1+l2+l3+l4+l5);
s6=ICcombined_ica(:,l1+l2+l3+l4+l5+1:l1+l2+l3+l4+l5+l6);
s7=ICcombined_ica(:,l1+l2+l3+l4+l5+l6+1:l1+l2+l3+l4+l5+l6+l7);
s8=ICcombined_ica(:,l1+l2+l3+l4+l5+l6+l7+1:l1+l2+l3+l4+l5+l6+l7+l8);
s9=ICcombined_ica(:,l1+l2+l3+l4+l5+l6+l7+l8+1:l1+l2+l3+l4+l5+l6+l7+l8+l9);
s10=ICcombined_ica(:,l1+l2+l3+l4+l5+l6+l7+l8+l9+1:l1+l2+l3+l4+l5+l6+l7+l8+l9+l10);
s11=ICcombined_ica(:,l1+l2+l3+l4+l5+l6+l7+l8+l9+l10+1:l1+l2+l3+l4+l5+l6+l7+l8+l9+l10
+l11);
s12=ICcombined_ica(:,l1+l2+l3+l4+l5+l6+l7+l8+l9+l10+l11+1:l1+l2+l3+l4+l5+l6+l7+l8+l9
+l10+l11+l12);
s13=ICcombined_ica(:,l1+l2+l3+l4+l5+l6+l7+l8+l9+l10+l11+l12+1:l1+l2+l3+l4+l5+l6+l7+l
8+l9+l10+l11+l12+l13);
s14=ICcombined_ica(:,l1+l2+l3+l4+l5+l6+l7+l8+l9+l10+l11+l12+l13+1:l1+l2+l3+l4+l5+l6
+l7+l8+l9+l10+l11+l12+l13+l14);
s15=ICcombined_ica(:,l1+l2+l3+l4+l5+l6+l7+l8+l9+l10+l11+l12+l13+l14+1:l1+l2+l3+l4+l
5+l6+l7+l8+l9+l10+l11+l12+l13+l14+l15);
```

```
s16=ICcombined_ica(:,l1+l2+l3+l4+l5+l6+l7+l8+l9+l10+l11+l12+l13+l14+l15+1:l1+l2+l3+
l4+l5+l6+l7+l8+l9+l10+l11+l12+l13+l14+l15+l16);
s17=ICcombined_ica(:,l1+l2+l3+l4+l5+l6+l7+l8+l9+l10+l11+l12+l13+l14+l15+l16+1:l1+l2
+l3+l4+l5+l6+l7+l8+l9+l10+l11+l12+l13+l14+l15+l16+l17);
s18=ICcombined_ica(:,l1+l2+l3+l4+l5+l6+l7+l8+l9+l10+l11+l12+l13+l14+l15+l16+l17+1:l
1+l2+l3+l4+l5+l6+l7+l8+l9+l10+l11+l12+l13+l14+l15+l16+l17+l18);
s19=ICcombined_ica(:,l1+l2+l3+l4+l5+l6+l7+l8+l9+l10+l11+l12+l13+l14+l15+l16+l17+l1
8+1:l1+l2+l3+l4+l5+l6+l7+l8+l9+l10+l11+l12+l13+l14+l15+l16+l17+l18+l19);
s20=ICcombined_ica(:,l1+l2+l3+l4+l5+l6+l7+l8+l9+l10+l11+l12+l13+l14+l15+l16+l17+l1
8+l19+1:l1+l2+l3+l4+l5+l6+l7+l8+l9+l10+l11+l12+l13+l14+l15+l16+l17+l18+l19+l20);
s21=ICcombined_ica(:,l1+l2+l3+l4+l5+l6+l7+l8+l9+l10+l11+l12+l13+l14+l15+l16+l17+l1
8+l19+l20+1:l1+l2+l3+l4+l5+l6+l7+l8+l9+l10+l11+l12+l13+l14+l15+l16+l17+l18+l19+l20
+l21);
s22=ICcombined_ica(:,l1+l2+l3+l4+l5+l6+l7+l8+l9+l10+l11+l12+l13+l14+l15+l16+l17+l1
8+l19+l20+l21+1:l1+l2+l3+l4+l5+l6+l7+l8+l9+l10+l11+l12+l13+l14+l15+l16+l17+l18+l19
+l20+l21+l22);
s23=ICcombined_ica(:,l1+l2+l3+l4+l5+l6+l7+l8+l9+l10+l11+l12+l13+l14+l15+l16+l17+l1
8+l19+l20+l21+l22+1:l1+l2+l3+l4+l5+l6+l7+l8+l9+l10+l11+l12+l13+l14+l15+l16+l17+l18
+l19+l20+l21+l22+l23);
s24=ICcombined_ica(:,l1+l2+l3+l4+l5+l6+l7+l8+l9+l10+l11+l12+l13+l14+l15+l16+l17+l1
8+l19+l20+l21+l22+l23+1:l1+l2+l3+l4+l5+l6+l7+l8+l9+l10+l11+l12+l13+l14+l15+l16+l17
+l18+l19+l20+l21+l22+l23+l24);

for i=1:1:40
   for j=1:1:133
       temp=corrcoef(s1(i,:),x1_new.HbO(:,j)');
      corr_s_pain(i,j,1)=temp(1,2);
       temp=corrcoef(s2(i,:),x2_new.HbO(:,j)');
      corr_s_pain(i,j,2)=temp(1,2);
       temp=corrcoef(s3(i,:),x3_new.HbO(:,j)');
      corr_s_pain(i,j,3)=temp(1,2);
       temp=corrcoef(s4(i,:),x4_new.HbO(:,j)');
      corr_s_pain(i,j,4)=temp(1,2);
       temp=corrcoef(s5(i,:),x5_new.HbO(:,j)');
      corr_s_pain(i,j,5)=temp(1,2);
       temp=corrcoef(s6(i,:),x6_new.HbO(:,j)');
      corr_s_pain(i,j,6)=temp(1,2);
       temp=corrcoef(s7(i,:),x7_new.HbO(:,j)');
      corr_s_pain(i,j,7)=temp(1,2);
       temp=corrcoef(s8(i,:),x8_new.HbO(:,j)');
      corr_s_pain(i,j,8)=temp(1,2);
       temp=corrcoef(s9(i,:),x9_new.HbO(:,j)');
      corr_s_pain(i,j,9)=temp(1,2);
       temp=corrcoef(s10(i,:),x10_new.HbO(:,j)');
      corr_s_pain(i,j,10)=temp(1,2);
       temp=corrcoef(s11(i,:),x11_new.HbO(:,j)');
```

```
        corr_s_pain(i,j,11)=temp(1,2);
         temp=corrcoef(s12(i,:),x12_new.HbO(:,j)');
        corr_s_pain(i,j,12)=temp(1,2);

        temp=corrcoef(s13(i,:),y1_new.HbO(:,j)');
        corr_s_control(i,j,1)=temp(1,2);
         temp=corrcoef(s14(i,:),y2_new.HbO(:,j)');
        corr_s_control(i,j,2)=temp(1,2);
         temp=corrcoef(s15(i,:),y3_new.HbO(:,j)');
        corr_s_control(i,j,3)=temp(1,2);
         temp=corrcoef(s16(i,:),y4_new.HbO(:,j)');
        corr_s_control(i,j,4)=temp(1,2);
         temp=corrcoef(s17(i,:),y5_new.HbO(:,j)');
        corr_s_control(i,j,5)=temp(1,2);
         temp=corrcoef(s18(i,:),y6_new.HbO(:,j)');
        corr_s_control(i,j,6)=temp(1,2);
         temp=corrcoef(s19(i,:),y7_new.HbO(:,j)');
        corr_s_control(i,j,7)=temp(1,2);
         temp=corrcoef(s20(i,:),y8_new.HbO(:,j)');
        corr_s_control(i,j,8)=temp(1,2);
         temp=corrcoef(s21(i,:),y9_new.HbO(:,j)');
        corr_s_control(i,j,9)=temp(1,2);
         temp=corrcoef(s22(i,:),y10_new.HbO(:,j)');
        corr_s_control(i,j,10)=temp(1,2);
         temp=corrcoef(s23(i,:),y11_new.HbO(:,j)');
        corr_s_control(i,j,11)=temp(1,2);
         temp=corrcoef(s24(i,:),y12_new.HbO(:,j)');
        corr_s_control(i,j,12)=temp(1,2);

    end
end

corr_s_control_z=0.5*log((1+corr_s_control)./(1-corr_s_control));

mean_corr_s_control=mean(corr_s_control,3);
mean_corr_s_control_z=mean(corr_s_control_z,3);


for i=1:40
for j=1:133
    [h_z_control(i,j),p_z_control(i,j),ci,stats] = ttest(corr_s_control_z(i,j,:),0,0.01);
    t_z_control(i,j)=stats.tstat;
end
end

% for i=1:40
```

```
% value=mean_corr_s_control(i,:)';
% EasyTop_rot
%
% end

corr_s_pain_z=0.5*log((1+corr_s_pain)./(1-corr_s_pain));

mean_corr_s_pain=mean(corr_s_pain,3);
mean_corr_s_pain_z=mean(corr_s_pain_z,3);


for i=1:40
for j=1:133
    [h_z_pain(i,j),p_z_pain(i,j),ci,stats] = ttest(corr_s_pain_z(i,j,1:12),0,0.01);
    t_z_pain(i,j)=stats.tstat;
end
end


for i=1:40
for j=1:133
    [h_z_diff(i,j),p_z_diff(i,j),ci,stats] =
ttest2(corr_s_control_z(i,j,1:12),corr_s_pain_z(i,j,1:12),0.01);
    t_z_diff(i,j)=stats.tstat;
end
end
```

References

Adelson, P. D., Nemoto, E., Scheuer, M., Painter, M., Morgan, J., & Yonas, H. (1999). Noninvasive continuous monitoring of cerebral oxygenation periictally using near-infrared spectroscopy: a preliminary report. *Epilepsia, 40*(11), 1484-1489.

Apkarian, A. V., Bushnell, M. C., Treede, R. D., & Zubieta, J. K. (2005). Human brain mechanisms of pain perception and regulation in health and disease. *Eur J Pain, 9*(4), 463-484. doi:10.1016/j.ejpain.2004.11.001

Apkarian, A. V., Sosa, Y., Krauss, B. R., Thomas, P. S., Fredrickson, B. E., Levy, R. E., . . . Chialvo, D. R. (2004). Chronic pain patients are impaired on an emotional decision-making task. *Pain, 108*(1-2), 129-136. doi:10.1016/j.pain.2003.12.015

Apkarian, A. V., Sosa, Y., Sonty, S., Levy, R. M., Harden, R. N., Parrish, T. B., & Gitelman, D. R. (2004). Chronic back pain is associated with decreased prefrontal and thalamic gray matter density. *J Neurosci, 24*(46), 10410-10415. doi:10.1523/JNEUROSCI.2541-04.2004

Arbanas, G. (2010). Patients with combat-related and war-related posttraumatic stress disorder 10 years after diagnosis. *Croat Med J, 51*(3), 209-214.

Aupperle, R. L., Melrose, A. J., Stein, M. B., & Paulus, M. P. (2012). Executive function and PTSD: disengaging from trauma. *Neuropharmacology, 62*(2), 686-694. doi:10.1016/j.neuropharm.2011.02.008

Baliki, M. N., Chialvo, D. R., Geha, P. Y., Levy, R. M., Harden, R. N., Parrish, T. B., & Apkarian, A. V. (2006). Chronic pain and the emotional brain: specific brain activity associated with spontaneous fluctuations of intensity of chronic back pain. *J Neurosci, 26*(47), 12165-12173. doi:10.1523/JNEUROSCI.3576-06.2006

Baliki, M. N., Geha, P. Y., Apkarian, A. V., & Chialvo, D. R. (2008). Beyond feeling: chronic pain hurts the brain, disrupting the default-mode network dynamics. *J Neurosci, 28*(6), 1398-1403. doi:10.1523/JNEUROSCI.4123-07.2008

Baliki, M. N., Mansour, A. R., Baria, A. T., & Apkarian, A. V. (2014). Functional reorganization of the default mode network across chronic pain conditions. *PLoS One, 9*(9), e106133. doi:10.1371/journal.pone.0106133

Baliki, M. N., Schnitzer, T. J., Bauer, W. R., & Apkarian, A. V. (2011). Brain morphological signatures for chronic pain. *PLoS One, 6*(10), e26010. doi:10.1371/journal.pone.0026010

Banich, M. T., Milham, M. P., Atchley, R., Cohen, N. J., Webb, A., Wszalek, T., . . . Magin, R. (2000). fMri studies of Stroop tasks reveal unique roles of anterior and posterior brain systems in attentional selection. *J Cogn Neurosci, 12*(6), 988-1000.

Becerra, L., Breiter, H. C., Wise, R., Gonzalez, R. G., & Borsook, D. (2001). Reward circuitry activation by noxious thermal stimuli. *Neuron, 32*(5), 927-946.

Becerra, L., Harris, W., Grant, M., George, E., Boas, D., & Borsook, D. (2009). Diffuse optical tomography activation in the somatosensory cortex: specific activation by painful vs. non-painful thermal stimuli. *PLoS One, 4*(11), e8016. doi:10.1371/journal.pone.0008016

Becerra, L., Morris, S., Bazes, S., Gostic, R., Sherman, S., Gostic, J., . . . Borsook, D. (2006). Trigeminal neuropathic pain alters responses in CNS circuits to mechanical (brush) and thermal (cold and heat) stimuli. *J Neurosci, 26*(42), 10646-10657. doi:10.1523/JNEUROSCI.2305-06.2006

Beckmann, C. F., DeLuca, M., Devlin, J. T., & Smith, S. M. (2005). Investigations into resting-state connectivity using independent component analysis. *Philos Trans R Soc Lond B Biol Sci, 360*(1457), 1001-1013. doi:10.1098/rstb.2005.1634

Biswal, B., Yetkin, F. Z., Haughton, V. M., & Hyde, J. S. (1995). Functional connectivity in the motor cortex of resting human brain using echo-planar MRI. *Magn Reson Med, 34*(4), 537-541.

Boas, D. A., Dale, A. M., & Franceschini, M. A. (2004). Diffuse optical imaging of brain activation: approaches to optimizing image sensitivity, resolution, and accuracy. *Neuroimage, 23 Suppl 1*, S275-288. doi:10.1016/j.neuroimage.2004.07.011

Bouckoms, A. J. (1994). Limbic surgery for pain. *Textbook of pain*.

Brandes, D., Ben-Schachar, G., Gilboa, A., Bonne, O., Freedman, S., & Shalev, A. Y. (2002). PTSD symptoms and cognitive performance in recent trauma survivors. *Psychiatry Res, 110*(3), 231-238.

Breivik, H., Borchgrevink, P. C., Allen, S. M., Rosseland, L. A., Romundstad, L., Hals, E. K., . . . Stubhaug, A. (2008). Assessment of pain. *Br J Anaesth, 101*(1), 17-24. doi:10.1093/bja/aen103

Bremner, J. D., Scott, T. M., Delaney, R. C., Southwick, S. M., Mason, J. W., Johnson, D. R., . . . Charney, D. S. (1993). Deficits in short-term memory in posttraumatic stress disorder. *Am J Psychiatry, 150*(7), 1015-1019. doi:10.1176/ajp.150.7.1015

Brighina, F., Piazza, A., Vitello, G., Aloisio, A., Palermo, A., Daniele, O., & Fierro, B. (2004). rTMS of the prefrontal cortex in the treatment of chronic migraine: a pilot study. *J Neurol Sci, 227*(1), 67-71. doi:10.1016/j.jns.2004.08.008

Brown, J. E., Chatterjee, N., Younger, J., & Mackey, S. (2011). Towards a physiology-based measure of pain: patterns of human brain activity distinguish painful from non-painful thermal stimulation. *PLoS One, 6*(9), e24124. doi:10.1371/journal.pone.0024124

Bruehl, S., Burns, J. W., Chung, O. Y., & Chont, M. (2009). Pain-related effects of trait anger expression: neural substrates and the role of endogenous opioid mechanisms. *Neurosci Biobehav Rev, 33*(3), 475-491. doi:10.1016/j.neubiorev.2008.12.003

Buckalew, N., Haut, M. W., Morrow, L., & Weiner, D. (2008). Chronic pain is associated with brain volume loss in older adults: preliminary evidence. *Pain Med, 9*(2), 240-248. doi:10.1111/j.1526-4637.2008.00412.x

Buckner, R. L., Andrews-Hanna, J. R., & Schacter, D. L. (2008). The brain's default network: anatomy, function, and relevance to disease. *Ann N Y Acad Sci, 1124*, 1-38. doi:10.1196/annals.1440.011

Calhoun, V. D., Adali, T., Pearlson, G. D., & Pekar, J. J. (2001). A method for making group inferences from functional MRI data using independent component analysis. *Hum Brain Mapp, 14*(3), 140-151.

Calhoun, V. D., Liu, J., & Adali, T. (2009). A review of group ICA for fMRI data and ICA for joint inference of imaging, genetic, and ERP data. *Neuroimage, 45*(1 Suppl), S163-172. doi:10.1016/j.neuroimage.2008.10.057

Casey, K. L. (1999). Forebrain mechanisms of nociception and pain: analysis through imaging. *Proc Natl Acad Sci U S A, 96*(14), 7668-7674.

Cauda, F., Sacco, K., Duca, S., Cocito, D., D'Agata, F., Geminiani, G. C., & Canavero, S. (2009). Altered resting state in diabetic neuropathic pain. *PLoS One, 4*(2), e4542. doi:10.1371/journal.pone.0004542

Chance, B., Leigh, J. S., Miyake, H., Smith, D. S., Nioka, S., Greenfeld, R., . . . et al. (1988). Comparison of time-resolved and -unresolved measurements of deoxyhemoglobin in brain. *Proc Natl Acad Sci U S A, 85*(14), 4971-4975.

Chandrasekaran, H., & Kim, K. K. (1999). Sizing of the multilayer perceptron via modular networks. . *Neural Networks for signal processing*.

Cope, M., & Delpy, D. T. (1988). System for long-term measurement of cerebral blood and tissue oxygenation on newborn infants by near infra-red transillumination. *Med Biol Eng Comput, 26*(3), 289-294.

Cope, M., Delpy, D. T., Reynolds, E. O., Wray, S., Wyatt, J., & van der Zee, P. (1988). Methods of quantitating cerebral near infrared spectroscopy data. *Adv Exp Med Biol, 222*, 183-189.

Craggs, J. G., Price, D. D., Verne, G. N., Perlstein, W. M., & Robinson, M. M. (2007). Functional brain interactions that serve cognitive-affective processing during pain and placebo analgesia. *Neuroimage, 38*(4), 720-729. doi:10.1016/j.neuroimage.2007.07.057

Davis, K. D., Hutchison, W. D., Lozano, A. M., & Dostrovsky, J. O. (1994). Altered pain and temperature perception following cingulotomy and capsulotomy in a patient with schizoaffective disorder. *Pain, 59*(2), 189-199.

Delgado, M. R., Nearing, K. I., Ledoux, J. E., & Phelps, E. A. (2008). Neural circuitry underlying the regulation of conditioned fear and its relation to extinction. *Neuron, 59*(5), 829-838. doi:10.1016/j.neuron.2008.06.029

Delpy, D. T., Cope, M., van der Zee, P., Arridge, S., Wray, S., & Wyatt, J. (1988). Estimation of optical pathlength through tissue from direct time of flight measurement. *Phys Med Biol, 33*(12), 1433-1442.

Derbyshire, S. W., Jones, A. K., Creed, F., Starz, T., Meltzer, C. C., Townsend, D. W., . . . Firestone, L. (2002). Cerebral responses to noxious thermal stimulation in chronic low back pain patients and normal controls. *Neuroimage, 16*(1), 158-168. doi:10.1006/nimg.2002.1066

Derrfuss, J., Brass, M., Neumann, J., & von Cramon, D. Y. (2005). Involvement of the inferior frontal junction in cognitive control: meta-analyses of switching and Stroop studies. *Hum Brain Mapp, 25*(1), 22-34. doi:10.1002/hbm.20127

Diers, M., Koeppe, C., Diesch, E., Stolle, A. M., Holzl, R., Schiltenwolf, M., . . . Flor, H. (2007). Central processing of acute muscle pain in chronic low back pain patients: an EEG mapping study. *J Clin Neurophysiol, 24*(1), 76-83. doi:10.1097/01.wnp.0000241093.00844.0e

Dohrenwend, B. P., Turner, J. B., Turse, N. A., Adams, B. G., Koenen, K. C., & Marshall, R. (2006). The psychological risks of Vietnam for U.S. veterans: a revisit with new data and methods. *Science, 313*(5789), 979-982. doi:10.1126/science.1128944

Drangsholt, M., & LeResche, L. (1999). Temporomandibular Disorder Pain. In: Task Force on Epidemiology of the International Association for the Study of Pain (IASP) [Press release]

Duncan, A., Meek, J. H., Clemence, M., Elwell, C. E., Tyszczuk, L., Cope, M., & Delpy, D. T. (1995). Optical pathlength measurements on adult head, calf and forearm and the head of the newborn infant using phase resolved optical spectroscopy. *Phys Med Biol, 40*(2), 295-304.

Durduran, T., Choe, R., Baker, W. B., & Yodh, A. G. (2010). Diffuse Optics for Tissue Monitoring and Tomography. *Rep Prog Phys, 73*(7). doi:10.1088/0034-4885/73/7/076701

Ehlis, A. C., Herrmann, M. J., Wagener, A., & Fallgatter, A. J. (2005). Multi-channel near-infrared spectroscopy detects specific inferior-frontal activation during incongruent Stroop trials. *Biol Psychol, 69*(3), 315-331. doi:10.1016/j.biopsycho.2004.09.003

Erickson, D. J., Wolfe, J., King, D. W., King, L. A., & Sharkansky, E. J. (2001). Posttraumatic stress disorder and depression symptomatology in a sample of Gulf War veterans: a prospective analysis. *J Consult Clin Psychol, 69*(1), 41-49.

Erk, S., Mikschl, A., Stier, S., Ciaramidaro, A., Gapp, V., Weber, B., & Walter, H. (2010). Acute and sustained effects of cognitive emotion regulation in major depression. *J Neurosci, 30*(47), 15726-15734. doi:10.1523/JNEUROSCI.1856-10.2010

Eschweiler, G. W., Wegerer, C., Schlotter, W., Spandl, C., Stevens, A., Bartels, M., & Buchkremer, G. (2000). Left prefrontal activation predicts therapeutic effects of repetitive transcranial magnetic stimulation (rTMS) in major depression. *Psychiatry Res, 99*(3), 161-172.

Essenpreis, M., Elwell, C. E., Cope, M., van der Zee, P., Arridge, S. R., & Delpy, D. T. (1993). Spectral dependence of temporal point spread functions in human tissues. *Appl Opt, 32*(4), 418-425. doi:10.1364/AO.32.000418

Etkin, A., & Wager, T. D. (2007). Functional neuroimaging of anxiety: a meta-analysis of emotional processing in PTSD, social anxiety disorder, and specific phobia. *Am J Psychiatry, 164*(10), 1476-1488. doi:10.1176/appi.ajp.2007.07030504

Falconer, E., Bryant, R., Felmingham, K. L., Kemp, A. H., Gordon, E., Peduto, A., . . . Williams, L. M. (2008). The neural networks of inhibitory control in posttraumatic stress disorder. *J Psychiatry Neurosci, 33*(5), 413-422.

Fallgatter, A. J., Roesler, M., Sitzmann, L., Heidrich, A., Mueller, T. J., & Strik, W. K. (1997). Loss of functional hemispheric asymmetry in Alzheimer's dementia assessed with near-infrared spectroscopy. *Brain Res Cogn Brain Res, 6*(1), 67-72.

Fallgatter, A. J., & Strik, W. K. (2000). Reduced frontal functional asymmetry in schizophrenia during a cued continuous performance test assessed with near-infrared spectroscopy. *Schizophr Bull, 26*(4), 913-919.

Fierro, B., De Tommaso, M., Giglia, F., Giglia, G., Palermo, A., & Brighina, F. (2010). Repetitive transcranial magnetic stimulation (rTMS) of the dorsolateral prefrontal cortex (DLPFC) during capsaicin-induced pain: modulatory effects on motor cortex excitability. *Exp Brain Res, 203*(1), 31-38. doi:10.1007/s00221-010-2206-6

Flor, H., Knost, B., & Birbaumer, N. (1997). Processing of pain- and body-related verbal material in chronic pain patients: central and peripheral correlates. *Pain, 73*(3), 413-421.

Fox, M. D., Snyder, A. Z., Vincent, J. L., Corbetta, M., Van Essen, D. C., & Raichle, M. E. (2005). The human brain is intrinsically organized into dynamic, anticorrelated functional networks. *Proc Natl Acad Sci U S A, 102*(27), 9673-9678. doi:10.1073/pnas.0504136102

Francati, V., Vermetten, E., & Bremner, J. D. (2007). Functional neuroimaging studies in posttraumatic stress disorder: review of current methods and findings. *Depress Anxiety, 24*(3), 202-218. doi:10.1002/da.20208

Freund, W., Klug, R., Weber, F., Stuber, G., Schmitz, B., & Wunderlich, A. P. (2009). Perception and suppression of thermally induced pain: a fMRI study. *Somatosens Mot Res, 26*(1), 1-10. doi:10.1080/08990220902738243

Fukunaga, K. (1990). Introduction to statistical pattern recognition Computer science and scientific computing (pp. 1 online resource (xiii, 591 p.)). Retrieved from http://www.sciencedirect.com/science/book/9780080478654

Geha, P. Y., Baliki, M. N., Harden, R. N., Bauer, W. R., Parrish, T. B., & Apkarian, A. V. (2008). The brain in chronic CRPS pain: abnormal gray-white matter interactions in emotional and autonomic regions. *Neuron, 60*(4), 570-581. doi:10.1016/j.neuron.2008.08.022

Giesecke, T., Gracely, R. H., Clauw, D. J., Nachemson, A., Duck, M. H., Sabatowski, R., . . . Petzke, F. (2006). [Central pain processing in chronic low back pain. Evidence for reduced pain inhibition]. *Schmerz, 20*(5), 411-414, 416-417. doi:10.1007/s00482-006-0473-8

Giesecke, T., Gracely, R. H., Grant, M. A., Nachemson, A., Petzke, F., Williams, D. A., & Clauw, D. J. (2004). Evidence of augmented central pain processing in idiopathic chronic low back pain. *Arthritis Rheum, 50*(2), 613-623. doi:10.1002/art.20063

Glover, G. H. (1999). Deconvolution of impulse response in event-related BOLD fMRI. *Neuroimage, 9*(4), 416-429.

Greicius, M. D., Krasnow, B., Reiss, A. L., & Menon, V. (2003). Functional connectivity in the resting brain: a network analysis of the default mode hypothesis. *Proc Natl Acad Sci U S A, 100*(1), 253-258. doi:10.1073/pnas.0135058100

Guo, Y., & Pagnoni, G. (2008). A unified framework for group independent component analysis for multi-subject fMRI data. *Neuroimage, 42*(3), 1078-1093. doi:10.1016/j.neuroimage.2008.05.008

Gusnard, D. A., Akbudak, E., Shulman, G. L., & Raichle, M. E. (2001). Medial prefrontal cortex and self-referential mental activity: relation to a default mode of brain function. *Proc Natl Acad Sci U S A, 98*(7), 4259-4264. doi:10.1073/pnas.071043098

Hart, L. G., Deyo, R. A., & Cherkin, D. C. (1995). Physician office visits for low back pain. Frequency, clinical evaluation, and treatment patterns from a U.S. national survey. *Spine (Phila Pa 1976), 20*(1), 11-19.

Hart, R. P., Wade, J. B., & Martelli, M. F. (2003). Cognitive impairment in patients with chronic pain: the significance of stress. *Curr Pain Headache Rep, 7*(2), 116-126.

Hassanpour, M. S., White, B. R., Eggebrecht, A. T., Ferradal, S. L., Snyder, A. Z., & Culver, J. P. (2014). Statistical analysis of high density diffuse optical tomography. *Neuroimage, 85 Pt 1*, 104-116. doi:10.1016/j.neuroimage.2013.05.105

Hock, C., Villringer, K., Muller-Spahn, F., Hofmann, M., Schuh-Hofer, S., Heekeren, H., . . . Villringer, A. (1996). Near infrared spectroscopy in the diagnosis of Alzheimer's disease. *Ann N Y Acad Sci, 777*, 22-29.

Hoge, C. W., Castro, C. A., Messer, S. C., McGurk, D., Cotting, D. I., & Koffman, R. L. (2004). Combat duty in Iraq and Afghanistan, mental health problems, and barriers to care. *N Engl J Med, 351*(1), 13-22. doi:10.1056/NEJMoa040603

Holper, L., Gross, A., Scholkmann, F., Humphreys, B. K., Meier, M. L., Wolf, U., . . . Hotz-Boendermaker, S. (2014). Physiological effects of mechanical pain stimulation at the lower back measured by functional near-infrared spectroscopy and capnography. *J Integr Neurosci, 13*(1), 121-142. doi:10.1142/S0219635214500071

Huppert, T. J., Diamond, S. G., Franceschini, M. A., & Boas, D. A. (2009). HomER: a review of time-series analysis methods for near-infrared spectroscopy of the brain. *Appl Opt, 48*(10), D280-298.

Hyvarinen, A. (1999). Fast and robust fixed-point algorithms for independent component analysis. *IEEE Trans Neural Netw, 10*(3), 626-634. doi:10.1109/72.761722

Ivo, R., Nicklas, A., Dargel, J., Sobottke, R., Delank, K. S., Eysel, P., & Weber, B. (2013). Brain structural and psychometric alterations in chronic low back pain. *Eur Spine J, 22*(9), 1958-1964. doi:10.1007/s00586-013-2692-x

Jang, K. E., Tak, S., Jung, J., Jang, J., Jeong, Y., & Ye, J. C. (2009). Wavelet minimum description length detrending for near-infrared spectroscopy. *J Biomed Opt, 14*(3), 034004. doi:10.1117/1.3127204

Ji, G., Fu, Y., Ruppert, K. A., & Neugebauer, V. (2007). Pain-related anxiety-like behavior requires CRF1 receptors in the amygdala. *Mol Pain, 3*, 13. doi:10.1186/1744-8069-3-13

Kakigi, R., Koyama, S., Hoshiyama, M., Kitamura, Y., Shimojo, M., & Watanabe, S. (1995). Pain-related magnetic fields following painful CO2 laser stimulation in man. *Neurosci Lett, 192*(1), 45-48.

Kessler, R. C., Sonnega, A., Bromet, E., Hughes, M., & Nelson, C. B. (1995). Posttraumatic stress disorder in the National Comorbidity Survey. *Arch Gen Psychiatry, 52*(12), 1048-1060.

Kobayashi, Y., Kurata, J., Sekiguchi, M., Kokubun, M., Akaishizawa, T., Chiba, Y., . . . Kikuchi, S. (2009). Augmented cerebral activation by lumbar mechanical stimulus in chronic low back pain patients: an FMRI study. *Spine (Phila Pa 1976), 34*(22), 2431-2436. doi:10.1097/BRS.0b013e3181b1fb76

Koenen, K. C., Driver, K. L., Oscar-Berman, M., Wolfe, J., Folsom, S., Huang, M. T., & Schlesinger, L. (2001). Measures of prefrontal system dysfunction in posttraumatic stress disorder. *Brain Cogn, 45*(1), 64-78. doi:10.1006/brcg.2000.1256

Kohavi, R., & John, G. H. (1997). Wrappers for feature subset selection. . *Artificial intelligence*.

Kohl, M., Nolte, C., Heekeren, H. R., Horst, S., Scholz, U., Obrig, H., & Villringer, A. (1998). Determination of the wavelength dependence of the differential pathlength factor from near-infrared pulse signals. *Phys Med Biol, 43*(6), 1771-1782.

Kong, J., Loggia, M. L., Zyloney, C., Tu, P., Laviolette, P., & Gollub, R. L. (2010). Exploring the brain in pain: activations, deactivations and their relation. *Pain, 148*(2), 257-267. doi:10.1016/j.pain.2009.11.008

Kornelsen, J., Sboto-Frankenstein, U., McIver, T., Gervai, P., Wacnik, P., Berrington, N., & Tomanek, B. (2013). Default mode network functional connectivity altered in

failed back surgery syndrome. *J Pain, 14*(5), 483-491. doi:10.1016/j.jpain.2012.12.018

Kregel, J., Meeus, M., Malfliet, A., Dolphens, M., Danneels, L., Nijs, J., & Cagnie, B. (2015). Structural and functional brain abnormalities in chronic low back pain: A systematic review. *Semin Arthritis Rheum, 45*(2), 229-237. doi:10.1016/j.semarthrit.2015.05.002

Krummenacher, P., Candia, V., Folkers, G., Schedlowski, M., & Schonbachler, G. (2010). Prefrontal cortex modulates placebo analgesia. *Pain, 148*(3), 368-374. doi:10.1016/j.pain.2009.09.033

Kuchinad, A., Schweinhardt, P., Seminowicz, D. A., Wood, P. B., Chizh, B. A., & Bushnell, M. C. (2007). Accelerated brain gray matter loss in fibromyalgia patients: premature aging of the brain? *J Neurosci, 27*(15), 4004-4007. doi:10.1523/JNEUROSCI.0098-07.2007

Kulkarni, B., Bentley, D. E., Elliott, R., Julyan, P. J., Boger, E., Watson, A., . . . Jones, A. K. (2007). Arthritic pain is processed in brain areas concerned with emotions and fear. *Arthritis Rheum, 56*(4), 1345-1354. doi:10.1002/art.22460

Laird, A. R., McMillan, K. M., Lancaster, J. L., Kochunov, P., Turkeltaub, P. E., Pardo, J. V., & Fox, P. T. (2005). A comparison of label-based review and ALE meta-analysis in the Stroop task. *Hum Brain Mapp, 25*(1), 6-21. doi:10.1002/hbm.20129

Latremoliere, A., & Woolf, C. J. (2009). Central sensitization: a generator of pain hypersensitivity by central neural plasticity. *J Pain, 10*(9), 895-926. doi:10.1016/j.jpain.2009.06.012

Lebel, A., Becerra, L., Wallin, D., Moulton, E. A., Morris, S., Pendse, G., . . . Borsook, D. (2008). fMRI reveals distinct CNS processing during symptomatic and recovered complex regional pain syndrome in children. *Brain, 131*(Pt 7), 1854-1879. doi:10.1093/brain/awn123

Li, J., Manry, M. T., Narasimha, P. L., & Yu, C. (2006). Feature selection using a piecewise linear network. *IEEE Trans Neural Netw, 17*(5), 1101-1115. doi:10.1109/TNN.2006.877531

Liberzon, I., & Sripada, C. S. (2008). The functional neuroanatomy of PTSD: a critical review. *Prog Brain Res, 167*, 151-169. doi:10.1016/S0079-6123(07)67011-3

Lieberman, M. D., Eisenberger, N. I., Crockett, M. J., Tom, S. M., Pfeifer, J. H., & Way, B. M. (2007). Putting feelings into words: affect labeling disrupts amygdala activity in response to affective stimuli. *Psychol Sci, 18*(5), 421-428. doi:10.1111/j.1467-9280.2007.01916.x

Lloyd, D., Findlay, G., Roberts, N., & Nurmikko, T. (2008). Differences in low back pain behavior are reflected in the cerebral response to tactile stimulation of the lower back. *Spine (Phila Pa 1976), 33*(12), 1372-1377. doi:10.1097/BRS.0b013e3181734a8a

Loggia, M. L., Kim, J., Gollub, R. L., Vangel, M. G., Kirsch, I., Kong, J., . . . Napadow, V. (2013). Default mode network connectivity encodes clinical pain: an arterial spin labeling study. *Pain, 154*(1), 24-33. doi:10.1016/j.pain.2012.07.029

Lorenz, I. H., Egger, K., Schubert, H., Schnurer, C., Tiefenthaler, W., Hohlrieder, M., . . . Kolbitsch, C. (2008). Lornoxicam characteristically modulates cerebral pain-

processing in human volunteers: a functional magnetic resonance imaging study. *Br J Anaesth, 100*(6), 827-833. doi:10.1093/bja/aen082

Lorenz, J., Minoshima, S., & Casey, K. L. (2003). Keeping pain out of mind: the role of the dorsolateral prefrontal cortex in pain modulation. *Brain, 126*(Pt 5), 1079-1091.

Luchtmann, M., Steinecke, Y., Baecke, S., Lutzkendorf, R., Bernarding, J., Kohl, J., . . . Firsching, R. (2014). Structural brain alterations in patients with lumbar disc herniation: a preliminary study. *PLoS One, 9*(3), e90816. doi:10.1371/journal.pone.0090816

Mackey, S. C., & Maeda, F. (2004). Functional imaging and the neural systems of chronic pain. *Neurosurg Clin N Am, 15*(3), 269-288. doi:10.1016/j.nec.2004.03.001

MacLeod, C. M. (1991). Half a century of research on the Stroop effect: an integrative review. *Psychol Bull, 109*(2), 163-203.

Maihofner, C., Herzner, B., & Otto Handwerker, H. (2006). Secondary somatosensory cortex is important for the sensory-discriminative dimension of pain: a functional MRI study. *Eur J Neurosci, 23*(5), 1377-1383. doi:10.1111/j.1460-9568.2006.04632.x

Markham, J., White, B. R., Zeff, B. W., & Culver, J. P. (2009). Blind identification of evoked human brain activity with independent component analysis of optical data. *Hum Brain Mapp, 30*(8), 2382-2392. doi:10.1002/hbm.20678

Martucci, T., Ng , P., & Mackey, S. (2014). Neuroimaging Chronic Pain: What Have We Learned and Where Are We Going? *Future Neurology, 9*(6), 615-626.

Matsuda, G., & Hiraki, K. (2006). Sustained decrease in oxygenated hemoglobin during video games in the dorsal prefrontal cortex: a NIRS study of children. *Neuroimage, 29*(3), 706-711. doi:10.1016/j.neuroimage.2005.08.019

Matsuo, K., Kato, T., Fukuda, M., & Kato, N. (2000). Alteration of hemoglobin oxygenation in the frontal region in elderly depressed patients as measured by near-infrared spectroscopy. *J Neuropsychiatry Clin Neurosci, 12*(4), 465-471. doi:10.1176/jnp.12.4.465

Matsuo, K., Taneichi, K., Matsumoto, A., Ohtani, T., Yamasue, H., Sakano, Y., . . . Kato, T. (2003). Hypoactivation of the prefrontal cortex during verbal fluency test in PTSD: a near-infrared spectroscopy study. *Psychiatry Res, 124*(1), 1-10.

Mazoyer, P., Wicker, B., & Fonlupt, P. (2002). A neural network elicited by parametric manipulation of the attention load. *Neuroreport, 13*(17), 2331-2334. doi:10.1097/01.wnr.0000044988.13025.30

Medvedev, A. V., Kainerstorfer, J., Borisov, S. V., Barbour, R. L., & VanMeter, J. (2008). Event-related fast optical signal in a rapid object recognition task: improving detection by the independent component analysis. *Brain Res, 1236*, 145-158. doi:10.1016/j.brainres.2008.07.122

Mesquita, R. C., Franceschini, M. A., & Boas, D. A. (2010). Resting state functional connectivity of the whole head with near-infrared spectroscopy. *Biomed Opt Express, 1*(1), 324-336. doi:10.1364/BOE.1.000324

Morren, G., Wolf, U., Lemmerling, P., Wolf, M., Choi, J. H., Gratton, E., . . . Van Huffel, S. (2004). Detection of fast neuronal signals in the motor cortex from functional near

infrared spectroscopy measurements using independent component analysis. *Med Biol Eng Comput, 42*(1), 92-99.

Murphy, K., Birn, R. M., Handwerker, D. A., Jones, T. B., & Bandettini, P. A. (2009). The impact of global signal regression on resting state correlations: are anti-correlated networks introduced? *Neuroimage, 44*(3), 893-905. doi:10.1016/j.neuroimage.2008.09.036

Napadow, V., LaCount, L., Park, K., As-Sanie, S., Clauw, D. J., & Harris, R. E. (2010). Intrinsic brain connectivity in fibromyalgia is associated with chronic pain intensity. *Arthritis Rheum, 62*(8), 2545-2555. doi:10.1002/art.27497

Neugebauer, V., Galhardo, V., Maione, S., & Mackey, S. C. (2009). Forebrain pain mechanisms. *Brain Res Rev, 60*(1), 226-242. doi:10.1016/j.brainresrev.2008.12.014

Neugebauer, V., Li, W., Bird, G. C., & Han, J. S. (2004). The amygdala and persistent pain. *Neuroscientist, 10*(3), 221-234. doi:10.1177/1073858403261077

Obrig, H., & Villringer, A. (2003). Beyond the visible--imaging the human brain with light. *J Cereb Blood Flow Metab, 23*(1), 1-18.

Ochsner, K. N., Bunge, S. A., Gross, J. J., & Gabrieli, J. D. (2002). Rethinking feelings: an FMRI study of the cognitive regulation of emotion. *J Cogn Neurosci, 14*(8), 1215-1229. doi:10.1162/089892902760807212

Ochsner, K. N., Ludlow, D. H., Knierim, K., Hanelin, J., Ramachandran, T., Glover, G. C., & Mackey, S. C. (2006). Neural correlates of individual differences in pain-related fear and anxiety. *Pain, 120*(1-2), 69-77. doi:10.1016/j.pain.2005.10.014

Ohara, P. T., Vit, J. P., & Jasmin, L. (2005). Cortical modulation of pain. *Cell Mol Life Sci, 62*(1), 44-52. doi:10.1007/s00018-004-4283-9

Okada, F., Tokumitsu, Y., Hoshi, Y., & Tamura, M. (1994). Impaired interhemispheric integration in brain oxygenation and hemodynamics in schizophrenia. *Eur Arch Psychiatry Clin Neurosci, 244*(1), 17-25.

Okamoto, M., Dan, H., Sakamoto, K., Takeo, K., Shimizu, K., Kohno, S., . . . Dan, I. (2004). Three-dimensional probabilistic anatomical cranio-cerebral correlation via the international 10-20 system oriented for transcranial functional brain mapping. *Neuroimage, 21*(1), 99-111.

Pariente, J., White, P., Frackowiak, R. S., & Lewith, G. (2005). Expectancy and belief modulate the neuronal substrates of pain treated by acupuncture. *Neuroimage, 25*(4), 1161-1167. doi:10.1016/j.neuroimage.2005.01.016

Park, A. (2011). Healing the hurt. Finding new ways to treat pain. *Time, 177*(9), 64-68, 71.

Patterson, M. S., Chance, B., & Wilson, B. C. (1989). Time resolved reflectance and transmittance for the non-invasive measurement of tissue optical properties. *Appl Opt, 28*(12), 2331-2336. doi:10.1364/AO.28.002331

Peyron, R., Laurent, B., & Garcia-Larrea, L. (2000). Functional imaging of brain responses to pain. A review and meta-analysis (2000). *Neurophysiol Clin, 30*(5), 263-288.

Plichta, M. M., Herrmann, M. J., Baehne, C. G., Ehlis, A. C., Richter, M. M., Pauli, P., & Fallgatter, A. J. (2006). Event-related functional near-infrared spectroscopy

(fNIRS): are the measurements reliable? *Neuroimage, 31*(1), 116-124. doi:10.1016/j.neuroimage.2005.12.008

Power, J. D., Cohen, A. L., Nelson, S. M., Wig, G. S., Barnes, K. A., Church, J. A., . . . Petersen, S. E. (2011). Functional network organization of the human brain. *Neuron, 72*(4), 665-678. doi:10.1016/j.neuron.2011.09.006

Price, D. D. (2000). Psychological and neural mechanisms of the affective dimension of pain. *Science, 288*(5472), 1769-1772.

Price, D. D., Hu, J. W., Dubner, R., & Gracely, R. H. (1977). Peripheral suppression of first pain and central summation of second pain evoked by noxious heat pulses. *Pain, 3*(1), 57-68.

Pudil, P., Novovicová, J., & Kittler, J. (1994). Floating search methods in feature selection. *Pattern recognition letters, 2*, 279-283.

Raichle, M. E., MacLeod, A. M., Snyder, A. Z., Powers, W. J., Gusnard, D. A., & Shulman, G. L. (2001). A default mode of brain function. *Proc Natl Acad Sci U S A, 98*(2), 676-682. doi:10.1073/pnas.98.2.676

Reynolds, E. O., Wyatt, J. S., Azzopardi, D., Delpy, D. T., Cady, E. B., Cope, M., & Wray, S. (1988). New non-invasive methods for assessing brain oxygenation and haemodynamics. *Br Med Bull, 44*(4), 1052-1075.

Roca, V., Hart, J., Kimbrell, T., & Freeman, T. (2006). Cognitive function and dissociative disorder status among veteran subjects with chronic posttraumatic stress disorder: a preliminary study. *J Neuropsychiatry Clin Neurosci, 18*(2), 226-230. doi:10.1176/jnp.2006.18.2.226

Ruck, D. W., Rogers, S. K., Kabrisky, M., Oxley, M. E., & Suter, B. W. (1990). The multilayer perceptron as an approximation to a Bayes optimal discriminant function. *IEEE Trans Neural Netw, 1*(4), 296-298. doi:10.1109/72.80266

Schmidt-Wilcke, T., Leinisch, E., Ganssbauer, S., Draganski, B., Bogdahn, U., Altmeppen, J., & May, A. (2006). Affective components and intensity of pain correlate with structural differences in gray matter in chronic back pain patients. *Pain, 125*(1-2), 89-97. doi:10.1016/j.pain.2006.05.004

Schmithorst, V. J., & Holland, S. K. (2004). Comparison of three methods for generating group statistical inferences from independent component analysis of functional magnetic resonance imaging data. *J Magn Reson Imaging, 19*(3), 365-368. doi:10.1002/jmri.20009

Schroeter, M. L., Zysset, S., Kruggel, F., & von Cramon, D. Y. (2003). Age dependency of the hemodynamic response as measured by functional near-infrared spectroscopy. *Neuroimage, 19*(3), 555-564.

Schroeter, M. L., Zysset, S., Kupka, T., Kruggel, F., & Yves von Cramon, D. (2002). Near-infrared spectroscopy can detect brain activity during a color-word matching Stroop task in an event-related design. *Hum Brain Mapp, 17*(1), 61-71. doi:10.1002/hbm.10052

Schroeter, M. L., Zysset, S., & von Cramon, D. Y. (2004). Shortening intertrial intervals in event-related cognitive studies with near-infrared spectroscopy. *Neuroimage, 22*(1), 341-346. doi:10.1016/j.neuroimage.2003.12.041

Seminowicz, D. A., Mikulis, D. J., & Davis, K. D. (2004). Cognitive modulation of pain-related brain responses depends on behavioral strategy. *Pain, 112*(1-2), 48-58. doi:10.1016/j.pain.2004.07.027

Seminowicz, D. A., Shpaner, M., Keaser, M. L., Krauthamer, G. M., Mantegna, J., Dumas, J. A., . . . Naylor, M. R. (2013). Cognitive-behavioral therapy increases prefrontal cortex gray matter in patients with chronic pain. *J Pain, 14*(12), 1573-1584. doi:10.1016/j.jpain.2013.07.020

Seminowicz, D. A., Wideman, T. H., Naso, L., Hatami-Khoroushahi, Z., Fallatah, S., Ware, M. A., . . . Stone, L. S. (2011). Effective treatment of chronic low back pain in humans reverses abnormal brain anatomy and function. *J Neurosci, 31*(20), 7540-7550. doi:10.1523/JNEUROSCI.5280-10.2011

Shin, L. M., & Liberzon, I. (2010). The neurocircuitry of fear, stress, and anxiety disorders. *Neuropsychopharmacology, 35*(1), 169-191. doi:10.1038/npp.2009.83

Shulman, G. L., Fiez, J. A., Corbetta, M., Buckner, R. L., Miezin, F. M., Raichle, M. E., & Petersen, S. E. (1997). Common Blood Flow Changes across Visual Tasks: II. Decreases in Cerebral Cortex. *J Cogn Neurosci, 9*(5), 648-663. doi:10.1162/jocn.1997.9.5.648

Silverthorn, D. U., Hill, D., & Silverthorn, D. U. (2010). *Human physiology : an integrated approach : student workbook* (5th ed.). San Francisco, Calif.London: Benjamin Cummings ;Pearson Education distributor.

Singh, A. K., Okamoto, M., Dan, H., Jurcak, V., & Dan, I. (2005). Spatial registration of multichannel multi-subject fNIRS data to MNI space without MRI. *Neuroimage, 27*(4), 842-851. doi:10.1016/j.neuroimage.2005.05.019

Smith, S. M., Fox, P. T., Miller, K. L., Glahn, D. C., Fox, P. M., Mackay, C. E., . . . Beckmann, C. F. (2009). Correspondence of the brain's functional architecture during activation and rest. *Proc Natl Acad Sci U S A, 106*(31), 13040-13045. doi:10.1073/pnas.0905267106

Sokol, D. K., Markand, O. N., Daly, E. C., Luerssen, T. G., & Malkoff, M. D. (2000). Near infrared spectroscopy (NIRS) distinguishes seizure types. *Seizure, 9*(5), 323-327. doi:10.1053/seiz.2000.0406

Stroop, J. R. (1935). *Studies of interference in serial verbal reactions.* (Ph D), George Peabody College for Teachers, George Peabody College for Teachers, Nashville, Tenn.

Tagliazucchi, E., Balenzuela, P., Fraiman, D., & Chialvo, D. R. (2010). Brain resting state is disrupted in chronic back pain patients. *Neurosci Lett, 485*(1), 26-31. doi:10.1016/j.neulet.2010.08.053

Talbot, J. D., Villemure, J. G., Bushnell, M. C., & Duncan, G. H. (1995). Evaluation of pain perception after anterior capsulotomy: a case report. *Somatosens Mot Res, 12*(2), 115-126.

Tian, F., Kozel, F. A., Yennu, A., Croarkin, P. E., McClintock, S. M., Mapes, K. S., . . . Liu, H. (2012). Test-retest assessment of cortical activation induced by repetitive transcranial magnetic stimulation with brain atlas-guided optical topography. *J Biomed Opt, 17*(11), 116020. doi:10.1117/1.JBO.17.11.116020

Tian, F., & Liu, H. (2014). Depth-compensated diffuse optical tomography enhanced by general linear model analysis and an anatomical atlas of human head. *Neuroimage, 85 Pt 1*, 166-180. doi:10.1016/j.neuroimage.2013.07.016

Tian, F., Niu, H., Khan, B., Alexandrakis, G., Behbehani, K., & Liu, H. (2011). Enhanced functional brain imaging by using adaptive filtering and a depth compensation algorithm in diffuse optical tomography. *IEEE Trans Med Imaging, 30*(6), 1239-1251. doi:10.1109/TMI.2011.2111459

Tian, F., Yennu, A., Smith-Osborne, A., Gonzalez-Lima, F., North, C. S., & Liu, H. (2014). Prefrontal responses to digit span memory phases in patients with post-traumatic stress disorder (PTSD): a functional near infrared spectroscopy study. *Neuroimage Clin, 4*, 808-819. doi:10.1016/j.nicl.2014.05.005

Tracey, I., & Mantyh, P. W. (2007). The cerebral signature for pain perception and its modulation. *Neuron, 55*(3), 377-391. doi:10.1016/j.neuron.2007.07.012

Turk, D. C., & Dworkin, R. H. (2004). What should be the core outcomes in chronic pain clinical trials? *Arthritis Res Ther, 6*(4), 151-154. doi:10.1186/ar1196

van Dieen, J. H., Kuijer, P. P., Burdorf, A., Marras, W. S., & Adams, M. A. (2012). Non-specific low back pain. *Lancet, 379*(9829), 1874; author reply1874-1875. doi:10.1016/S0140-6736(12)60803-4

Vasterling, J. J., Brailey, K., Constans, J. I., & Sutker, P. B. (1998). Attention and memory dysfunction in posttraumatic stress disorder. *Neuropsychology, 12*(1), 125-133.

Vasterling, J. J., Duke, L. M., Brailey, K., Constans, J. I., Allain, A. N., Jr., & Sutker, P. B. (2002). Attention, learning, and memory performances and intellectual resources in Vietnam veterans: PTSD and no disorder comparisons. *Neuropsychology, 16*(1), 5-14.

Vincent, J. L., Kahn, I., Snyder, A. Z., Raichle, M. E., & Buckner, R. L. (2008). Evidence for a frontoparietal control system revealed by intrinsic functional connectivity. *J Neurophysiol, 100*(6), 3328-3342. doi:10.1152/jn.90355.2008

Wager, T. D., Davidson, M. L., Hughes, B. L., Lindquist, M. A., & Ochsner, K. N. (2008). Prefrontal-subcortical pathways mediating successful emotion regulation. *Neuron, 59*(6), 1037-1050. doi:10.1016/j.neuron.2008.09.006

Wager, T. D., Rilling, J. K., Smith, E. E., Sokolik, A., Casey, K. L., Davidson, R. J., . . . Cohen, J. D. (2004). Placebo-induced changes in FMRI in the anticipation and experience of pain. *Science, 303*(5661), 1162-1167. doi:10.1126/science.1093065

Wan, E. A. (1990). Neural network classification: a Bayesian interpretation. *IEEE Trans Neural Netw, 1*(4), 303-305. doi:10.1109/72.80269

Wand, B. M., Parkitny, L., O'Connell, N. E., Luomajoki, H., McAuley, J. H., Thacker, M., & Moseley, G. L. (2011). Cortical changes in chronic low back pain: current state of the art and implications for clinical practice. *Man Ther, 16*(1), 15-20. doi:10.1016/j.math.2010.06.008

Watanabe, E., Maki, A., Kawaguchi, F., Yamashita, Y., Koizumi, H., & Mayanagi, Y. (2000). Noninvasive cerebral blood volume measurement during seizures using multichannel near infrared spectroscopic topography. *J Biomed Opt, 5*(3), 287-290. doi:10.1117/1.429998

Wiech, K., Kalisch, R., Weiskopf, N., Pleger, B., Stephan, K. E., & Dolan, R. J. (2006). Anterolateral prefrontal cortex mediates the analgesic effect of expected and perceived control over pain. *J Neurosci, 26*(44), 11501-11509. doi:10.1523/JNEUROSCI.2568-06.2006

Wilcox, C. E., Mayer, A. R., Teshiba, T. M., Ling, J., Smith, B. W., Wilcox, G. L., & Mullins, P. G. (2015). The Subjective Experience of Pain: An FMRI Study of Percept-Related Models and Functional Connectivity. *Pain Med, 16*(11), 2121-2133. doi:10.1111/pme.12785

Willis, W. D., & Westlund, K. N. (1997). Neuroanatomy of the pain system and of the pathways that modulate pain. *J Clin Neurophysiol, 14*(1), 2-31.

Woolf, C. J. (2011). Central sensitization: implications for the diagnosis and treatment of pain. *Pain, 152*(3 Suppl), S2-15. doi:10.1016/j.pain.2010.09.030

Yanagisawa, H., Dan, I., Tsuzuki, D., Kato, M., Okamoto, M., Kyutoku, Y., & Soya, H. (2010). Acute moderate exercise elicits increased dorsolateral prefrontal activation and improves cognitive performance with Stroop test. *Neuroimage, 50*(4), 1702-1710. doi:10.1016/j.neuroimage.2009.12.023

Ye, J. C., Tak, S., Jang, K. E., Jung, J., & Jang, J. (2009). NIRS-SPM: statistical parametric mapping for near-infrared spectroscopy. *Neuroimage, 44*(2), 428-447. doi:10.1016/j.neuroimage.2008.08.036

Yennu, A., Tian, F., Rawat, R., Manry, M. T., Gatchel, R. J., & Liu, H. (2013). A Preliminary Investigation of Human Frontal Cortex Under Noxious Thermal Stimulation Over the Temporomandibular Joint Using Functional Near Infrared Spectroscopy. *Journal of Applied Biobehavioral Research, 18*(3), 134–155.

Yennu, A., Tian, F., Smith-Osborne, A., R, J. G., Woon, F. L., & Liu, H. (2016). Prefrontal responses to Stroop tasks in subjects with post-traumatic stress disorder assessed by functional near infrared spectroscopy. *Sci Rep, 6*, 30157. doi:10.1038/srep30157

Yeo, B. T., Krienen, F. M., Sepulcre, J., Sabuncu, M. R., Lashkari, D., Hollinshead, M., . . . Buckner, R. L. (2011). The organization of the human cerebral cortex estimated by intrinsic functional connectivity. *J Neurophysiol, 106*(3), 1125-1165. doi:10.1152/jn.00338.2011

Yu, C., Manry, M. T., Li, J., & Lakshmi Narasimha, P. (2006). An efficient hidden layer training method for the multilayer perceptron. . *Neurocomputing, 70*, 525-535.

Yuc, C., & Manry, M. T. (2007). Convergent design of piecewise linear neural networks. . *Neurocomputing, 70*, 1022-1039.

Yucel, M. A., Aasted, C. M., Petkov, M. P., Borsook, D., Boas, D. A., & Becerra, L. (2015). Specificity of hemodynamic brain responses to painful stimuli: a functional near-infrared spectroscopy study. *Sci Rep, 5*, 9469. doi:10.1038/srep09469

Zeff, B. W., White, B. R., Dehghani, H., Schlaggar, B. L., & Culver, J. P. (2007). Retinotopic mapping of adult human visual cortex with high-density diffuse optical tomography. *Proc Natl Acad Sci U S A, 104*(29), 12169-12174. doi:10.1073/pnas.0611266104

Zhang, H., Duan, L., Zhang, Y. J., Lu, C. M., Liu, H., & Zhu, C. Z. (2011). Test-retest assessment of independent component analysis-derived resting-state functional connectivity based on functional near-infrared spectroscopy. *Neuroimage, 55*(2), 607-615. doi:10.1016/j.neuroimage.2010.12.007

Zhang, H., Zhang, Y. J., Duan, L., Ma, S. Y., Lu, C. M., & Zhu, C. Z. (2011). Is resting-state functional connectivity revealed by functional near-infrared spectroscopy test-retest reliable? *J Biomed Opt, 16*(6), 067008. doi:10.1117/1.3591020

Zhang, H., Zhang, Y. J., Lu, C. M., Ma, S. Y., Zang, Y. F., & Zhu, C. Z. (2010). Functional connectivity as revealed by independent component analysis of resting-state fNIRS measurements. *Neuroimage, 51*(3), 1150-1161. doi:10.1016/j.neuroimage.2010.02.080

Zhuo, M. (2008). Cortical excitation and chronic pain. *Trends Neurosci, 31*(4), 199-207. doi:10.1016/j.tins.2008.01.003

Biographical Information

Amarnath Shivkumar Yennu, born in Hyderabad on September 11th 1986, received his Bachelor of Engineering degree in Biomedical Engineering from Jawahar Lal Nehru Technological University, India in May 2008. Amarnath received his Master of Science degree in Biomedical Engineering at the Joint Program of University of Texas at Arlington and University of Texas Southwestern Medical Center at Dallas, Texas in December 2010. In August 2011, he started his Ph.D. in Biomedical Engineering at the Joint Program of University of Texas at Arlington and University of Texas Southwestern Medical Center at Dallas, Texas, completing it by August 2016. His research expertise is in functional near infrared spectroscopy, medical image processing and signal processing, for applications in medical diagnostics and therapy. His interests include developing novel methods in medical image processing and providing engineering solutions to medical problems. In future, he hopes to contribute in improvement of global healthcare through his work in clinical research industry.